EXPERIMENTAL AND NUMERICAL STUDY OF OIL LUBRICATION ON A THRUST COLLAR FOR USE IN AN INTEGRALLY GEARED COMPRESSOR

A Dissertation

by

THOMAS CHANDLER KERR

Submitted to the Office of Graduate and Professional Studies of
Texas A&M University
in partial fulfillment of the requirements for the degree of

DOCTOR OF PHILOSOPHY

Chair of Committee,	Adolfo Delgado
Committee Members,	Luis San Andrés
	Stefan Hurlebaus
	Waruna Kulatilaka
Head of Department,	Andreas A. Polycarpou

August 2020

Major Subject: Mechanical Engineering

ABSTRACT

Thrust collars (TCs) are bearing elements used in geared machinery that transmit axial loads from one shaft to another. TCs are primarily used in integrally geared compressors (IGCs), but have applications in gearboxes, and marine propulsion. Accurate modeling requires knowledge of the film characteristics such as lubricant cavitation, flow turbulence, and air ingestion, all of which could potentially reduce load capacity. Current models in the literature do not properly account for lubricant cavitation or flow turbulence within the TC. The following dissertation introduces a new experimental set-up that optically characterizes the oil film in a thrust collar, along with two predictive models.

The test rig geometries, speeds, and loads match those seen in a typical industrial IGC. The test rig utilizes a transparent acrylic window in conjunction with a high speed camera to capture images of the oil film. Images are filtered and averaged to obtain areas of interest in the oil film. Lubricant cavitation and flow turbulence areas are measured for pinion speeds of 2.5, 5, and 7.5 krpm, and axial loads of 0.5, 1, and 1.5 kN. Cavitation occurs in the diverging (upper) region of the TC and appears at pinion speeds over 5,000 rpm, but does not change in shape after that speed. Turbulence at the inlet region (bottom) occurs at all speeds, but increases to almost 35% of the total area at the highest speed. The turbulence area decreases as the axial load increases.

The dissertation advances a finite element (FE) model that accounts for elastic deformation of the disks and uses a mass conserving function to model lubricant cavitation. Elastic deformation only becomes important to predicting load capacity at high loads (above 2 kN for a TC made of

acrylic). At higher loads (>2kN, 23.2 bar specific load), the predicted load capacity can be significantly lower when considering elastic deformation, even for a TC made of steel.

The dissertation also includes the first computation fluid dynamics (CFD) model predictions on a TC. The CFD model predicts a larger cavitation area than the FE model, or the experimental results (35-43% for CFD and 26% - 33% for FE). The CFD model predicts flow turbulence in the lower region that increases for increasing spin speed, which matches the experimental results, but tends to overpredict the total area.

Experiments include testing at various oil inlet velocities. As the oil inlet velocity approaches the surface speed of the TC, the turbulence area increases, until the oil velocity matches or exceeds the surface speed, at which point the flow turbulence drops off. CFD modeling matches this trend, but also tends to overpredict the total turbulence area. As IGCs move into new application areas to satisfy new needs, the increase in efficiency and capacity comes at a cost of more load and higher speed requirements on the TCs. This work will help original equipment manufacturers model TCs more accurately to ensure safe and efficient operating conditions.

ACKNOWLEDGEMENTS

I acknowledge and thank my committee, Dr. San Andrés, Dr. Kulatilaka, Dr. Hurlebaus, and especially Dr. Delgado.

I have many people to thank for helping with this dissertation, too many to remember, but I will try. Starting chronologically, I would like to thank God, for everything is His. My family has always supported me, especially my wife. When I first arrived at the turbomachinery lab, Dr. Childs and Andrew Crandall provided immense help, both from their expertise and their time. I owe an especial debt to Andrew Crandall for his help in starting the TC project, and pioneering the test rig. Several undergraduate students have helped me along the way, especially with testing: Johnny, Bryant, and Abe. Even more, graduate students have helped, Marie, Sean, Burak, Josh, and especially Travis Cable and Clay Norrbin.

CONTRIBUTORS AND FUNDING SOURCES

Contributors

This project has been managed by the following dissertation committee: Professor Adolfo Delgado, Professor Luis San Andrés, and Professor Waruna Kulatilaka of the Department of Mechanical Engineering and Professor Stefan Hurlebaus of the Department of Civil Engineering.

Most of this work was completed by the student, Thomas Kerr, all of it under the direction of Dr. Adolfo Delgado, and the rest of the committee. The TC modeling is based off of work completed by Dr. San Andres, and Travis Cable.

Funding Sources

Thanks are due to Professor Delgado for funding this project. Samsung Techwin also provided the funding necessary for building the original test rig.

NOMENCLATURE

Acronyms

BG	Bull Gear
BW	Bull Wheel
CFD	Computation Fluid Dynamics
EHD	Elastohydrodynamic
FE	Finite Element
FEA	Finite Element Analysis
fps	Frames per Second
FR	Frame Rate
IGC	Integrally Geared Compressor
HSC	High Speed Camera
HSS	High Speed Shaft
JFO	Jakobsson Floberg Olsson
LA	Lubricated Area
NSE	Navier-Stokes Equation
TC	Thrust Collar
TPTB	Tilting Pad Thrust Bearing
UCA	Universal Cavitation Algorithm
VFD	Variable Frequency Drive

Variables

2D	Two Dimensional

$3D$	Three Dimensional
A	Area
c	Height of LA
d	Distance Between Shafts
F_{TC}	Axial Force
g	Cavitation Switch Function
h	Film thickness
I	Greyscale Intensity Value
N	Number (count)
P	Film Pressure
$\dot{Q}$	Flow Rate
R_1	BG Radius
R_2	TC Radius
V	Velocity
α	Density Ratio
γ	Gamma Filter Value
Φ	Taper angle
ρ	Fluid Density
ω	Spin Speed

TABLE OF CONTENTS Page

LIST OF TABLES

Page

LIST OF FIGURES

Page

1. INTRODUCTION

Thrust Collars in Industry: Applications, Advantages, and Disadvantages

Integrally geared compressors (IGCs) are a widely growing option for industrial gas compression [1]. IGCs offer many advantages to traditional centrifugal compressors: a reduced footprint, easier maintenance, and increased efficiency [1]. Figure 1 displays a cut view of a typical IGC. An IGC uses a bull gear (BG) to spin anywhere from one to eight pinion shafts. Each pinion shaft has one or two compressor stages on its end. The process fluid is often cooled in between each compressor stage, resulting in increased efficiency. Typically, the pinion shafts are driven by the BG shaft through helical gearing. The pinion shaft spins at the gear ratio times the speed of the BG.

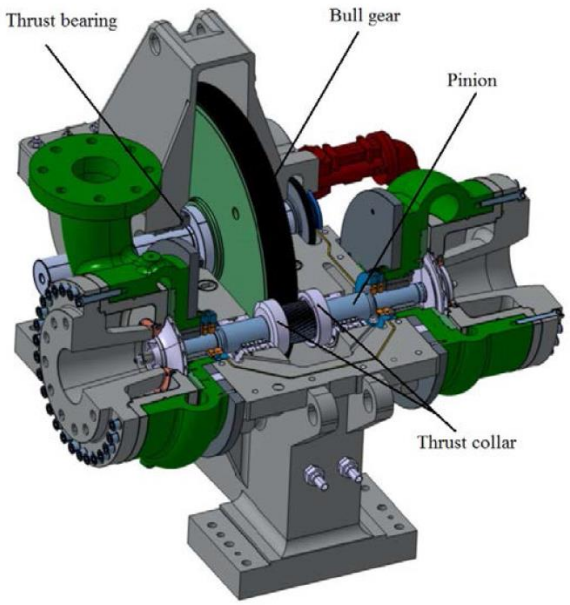

Figure 1. Cut view of a typical industrial IGC showing important components adapted from [1].

Beaty et al. [2] describes the advantages and disadvantages of using an IGC compared to a typical beam-type compressor. The authors compare the two types of compressors against capital and installed cost, operating cost, durability, downtime, and maintenance cost. Beam-type compressors typically have a higher durability, but a larger downtime. The authors also provide five hypothetical cases, and identify the advantages of using an IGC or beam type compressor. They conclude that IGCs typically offer higher efficiency, and generaly have lower installation costs.

The pressure rise across the compressor stage in IGCs, along with the forces from the helical gearing, create an axial force on the pinion shafts that must be balanced. Traditional tilting pad thrust bearings (TPTB) represent one alternative to balance the load on each pinion shaft. Another method to balance the load is to utilize a tapered thrust collar (TC). Figure 2 shows the working principle of a typical flat-faced TC. Both the BG and the TC will have a face with a taper angle on it (Φ), typically one to three degrees. The figure provides an exaggerated view with a larger taper angle. The minimum clearance between the two disks is at the centerline of the overlapping area. This creates a converging-diverging wedge with an increasing pressure field that can react the axial load created by the compressor stages and the helical gearing.

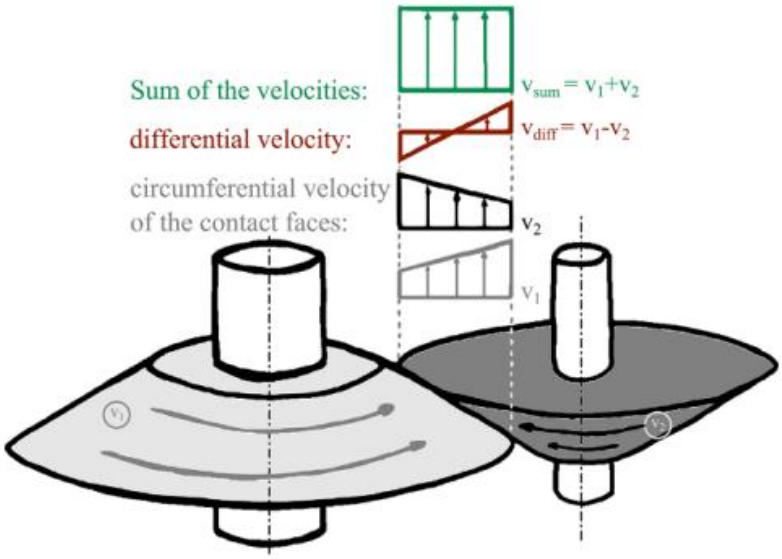

Figure 2. Expanded view of TC working principles, adapted from [3].

Because both faces are spinning in the same direction, the relative velocity between the two faces is smaller than that of a typical tilting pad thrust bearing. The lubricated area is also smaller than that of a TPTB. Both of these features lead to TCs having a smaller power loss as compared to a TPTB [3]. TCs are also cheaper to machine and install. However, the increase in efficiency comes at a cost of larger axial clearances of the pinion shafts, as well as a dynamic coupling between the BG and pinion shafts [1].

Motivation

Figure 3 shows the typical range of IGC industrial uses. IGCs currently occupy a large range of compression needs in terms of volume and discharge pressure, but IGC manufacturers are seeking to expand the range of IGCs to compete in a larger range of flows and compression ratios [1]. Increasing the compressor speed leads to higher efficiencies and more compact designs with

less compressor stages. This will allow IGCs to move into new application areas and satisfy new needs. The increase in efficiency and capacity comes at a cost of more load and higher speed requirements on the TCs.

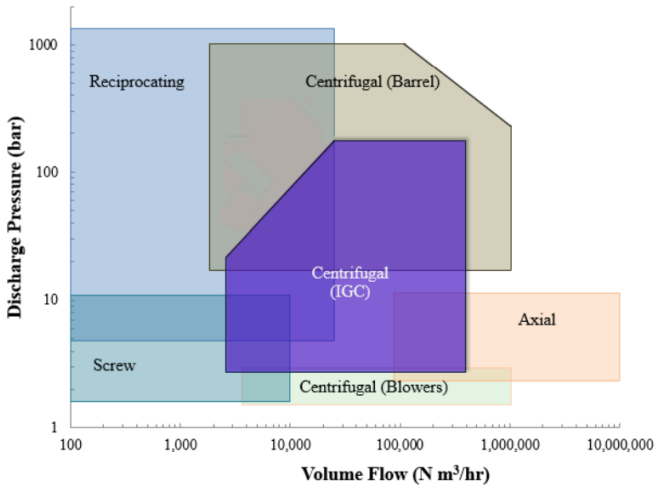

Figure 3. Operating range of IGCs with volume flow and discharge pressure, adapted from [1].

Hess and Lohrengel1 [3] suggest an expansion of thrust collars from IGCs to geared transmissions. The primary advantage of using TCs instead of tapered roller bearings is an increase in efficiency. They identify the decreased relative velocity between the two faces as compared to a rigid thrust bearing as the reason for the reduction in friction losses. The authors created two small scale test rigs, one with a thrust collar and the other with tapered roller bearings, and compared their efficiencies. The thrust collar rig proved to be more efficient. TCs in geared transmissions have higher load requirements, and more studies are necessary to ensure their safe usage.

Elastohydrodynamic (EHD) studies on the TC are well documented in the literature, as it will be explained further. Many studies have focused on predicting and improving the load capacity of the TC through mechanical and material advancements, but there has been little published research on the lubrication of the TC. One area lacking in literature is the low pressure diverging section of the TC. The diverging section of the TC leads to a lubricant cavitation area which limits the load capacity of the TC. Lubricant cavitation in TCs has received little to no attention in the literature thus far. Similarly, there are no studies available in the literate focusing on the oil delivery and inlet area. The oil inlet conditions have a large effect on the static performance of a TC, but have been largely ignored in the literature.

A thorough understanding of the lubricated area within the TCs will aide turbomachinery manufacturers in achieving higher speeds, loads, and more effective lubrication methods.

Literature Review

The chronological literature review covers four section: previous work done on thrust collars (TCs), optical test rigs, liquid cavitation modeling in bearings, and inlet condition studies of machinery lubricated with nozzles.

Experimental and Analytical Studies Performed on Thrust Collars

Jakob Niederhauser received the first approved patent in the United States for a TC in 1925 [4]. In 1968, Sadykov and Shneerson [5] presented the first experiments on a TC aimed to determine the ideal circumstances for maximum load capacity. The test parameters include the taper angle, the TC connection type, and the radius of the BG and TC. The authors determined that the taper angle of both the BG and pinion shaft should be within 0.5 to 2 degrees, that a taper angle of at least 0.5 degrees is necessary to develop the hydrodynamic wedge, and when the angle is above 2 degrees, the load capacity drops dramatically. They also suggest using the same taper

angle on both the TC and BG, otherwise scoring could occur. They also include results showing the best method to secure the TC to the shaft, to prevent the TC from slipping.

Langer [6] presented the first elastohydrodynamic (EHD) finite element analysis (FEA) on the lubricated area of a TC in 1982. Langer starts with the classical Reynolds equation of lubrication to solve for load capacity and power loss in the TC. Langer's analysis shows there is an ideal geometry yielding a maximum load capacity. He also includes results for a viscosity that is dependent on pressure.

Figure 4 shows plots for minimum film thickness as a function of axial load for three test cases: (a) rigid surfaces (b) rigid surfaces with pressure dependent viscosity, and (c) compliant disks with changing viscosity. In 1984, Simon [7] extended Langer's analysis to include thermal effects by using the energy equation. Simon concludes that higher viscosity oil increases the load capacity of the TC.

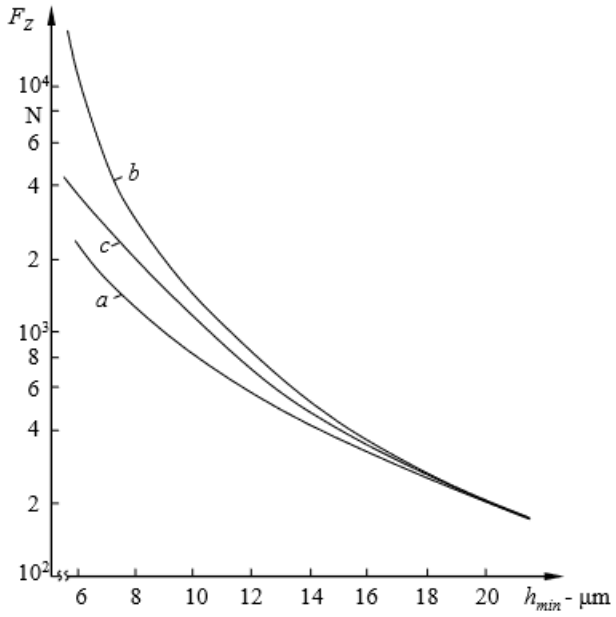

Figure 4. Predicted minimum film thickness as a function of load capacity for three test cases, adapted from [6].

In 1995, Barragan de Ling et al. [8] created a code to predict minimum film thickness. The primary purpose of the paper was to evaluate the effect of adding a crown on the outside edge of both the TC and the BG to help ensure full lubrication. The authors introduced a full EHD lubrication analysis predicting that as spin speed increases, the average and minimum film thickness will also increase. The application is for marine gearboxes, and does not directly apply to TCs for IGCs. There is no mention of lubricant cavitation or flow turbulence in the models from Barragan de Ling et al. [8] or Langer [6].

In 1996, Parkins and Rudd [9] developed a test rig capable of measuring the minimum and average film thickness of a TC lubricated area. They used a glass TC and tested at high loads (10 kN-no unit load or overlap area is given) and low speeds, matching TCs in marine gearbox applications. They shone a light through the glass TC and used light interferometry techniques to

determine the film thickness. They showed that film thickness increases versus mean speed of the TC.

Figure 5 shows the test rig designed by Parkins and Rudd, as well as their interferometry results. There is a limited description of the measured results, and there is no explanation for the various colored area. Furthermore, the authors show a film thickness based on the interferometry results but make no note of observing any lubricant cavitation.

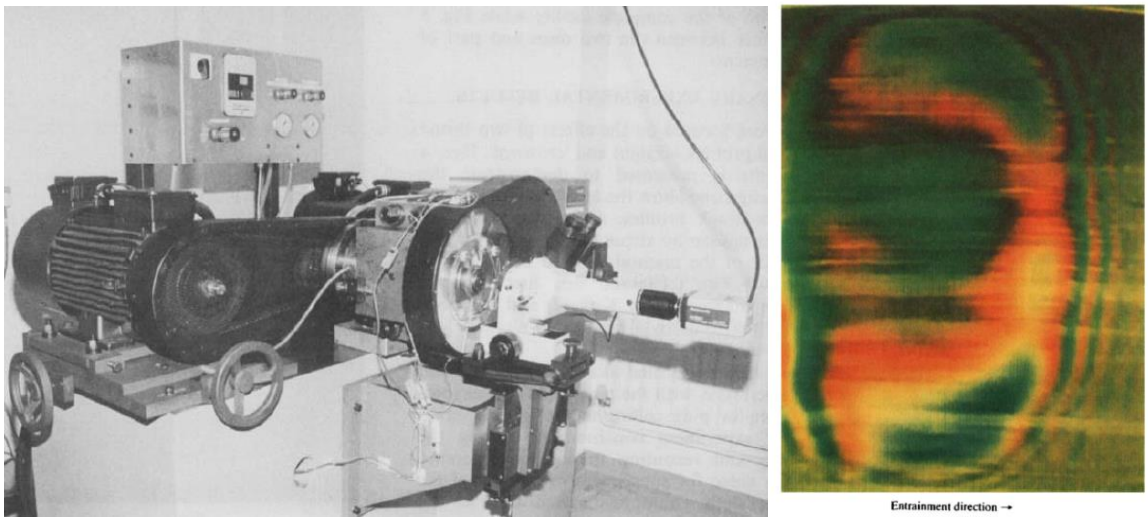

Figure 5. Test rig (left) and experimental results (right) from Parkins and Rudd test facility, adapted from [9].

Hess et al. [7] conducted experiments in 2013 on a TC test rig designed to measure inception of full hydrodynamic lubrication. They coated one face of the TC in an electrical insulating material, and measured the electrical resistance of the TC to determine when the two faces are no longer in contact. They determined the load capacity of the TC increases with increasing TC velocity and compared their results to a predictive code by Thoden [10]. Thoden's model included a shear stress equation to the EHD analysis to predict power loss.

Figure 6 shows the test rig created by Hess, as well as his measured results compared to the predictions by Thoden [10]. The test rig used two separate motors to spin each shaft. The diameter of the thrust collar and the bull gear were similar. They tested with an axial force up to 30 kN, but did not include specific load or power loss measurements.

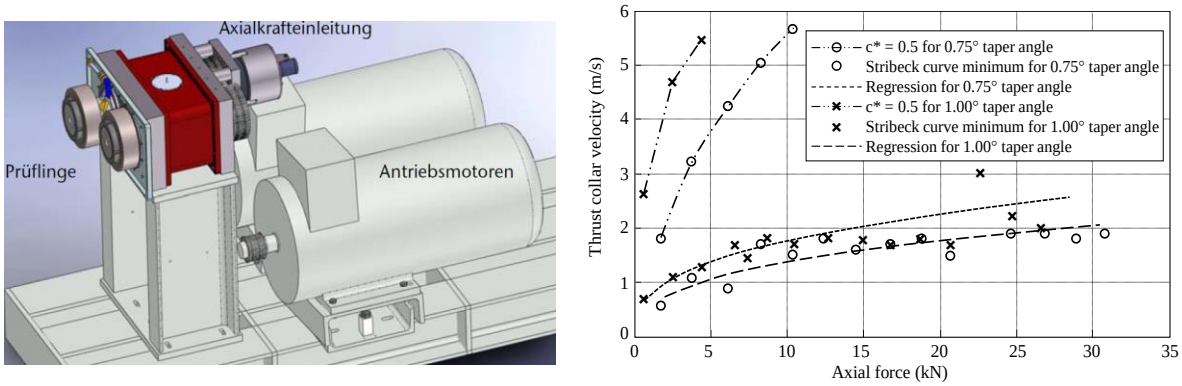

Figure 6. Test facility (left) and experimental and predicted results (right), adapted from Hess [3].

In 2015, San Andres et al. [11] introduced a dynamic model of a TC based on the classic Reynolds equation of lubrication. Their code, capable of modeling any geometry of the TC and BW, predicted both static and dynamic performance characteristics for the TC, including: load capacity, required lubricant flowrate, pressure field, film thickness, and stiffness and damping of the TC.

Cable et al. [12] extended the model from Ref. [11] to include thermal effects and misalignment of the BW and TC. The model does not include elastic deformation of the faces of the TC and BW. They used the Reynolds condition to model lubricant cavitation in the low pressure area, which does not conserve mass thorough the flow domain. The model predictions for stiffness correlated

well with the experimental stiffness coefficients identified by Kerr at al. [13]. The static results have not been benchmarked thus far.

Optical Test Rigs for Characterization of Fluid Films

Optical visualization of the lubricant film helps to characterize parameters in turbomachinery components. In 1971, Wedeven et al. [14] introduced a test rig that uses optical interferometry to identify areas of lubrication starvation. They also presented a numerical anaylysis on the lubrication starvation, based on the Reynolds' equation. The vertical test rig used a motor to spin a three ball thrust bearing. The camera and interferometer were placed over a glass race. The interferometer identifies the film thickness while the camera captures images that show areas of starvation and lubricant cavitation.

Figure 7 shows the results of two test cases. Case A is with a high film thickness and displays cavitation "fingers". Case B, with low thickness, shows cavitation bubbles forming outside the wake of the test ball. Tests were conducted at minimized lubricant flow rates to create starvation. The paper compares the film thickness and area of starvation to the predictions from the analysis, and the trends and magnitudes of both agree. The authors concluded that the onset of starvation occurs at a specific ratio of inlet geometry to film thickness.

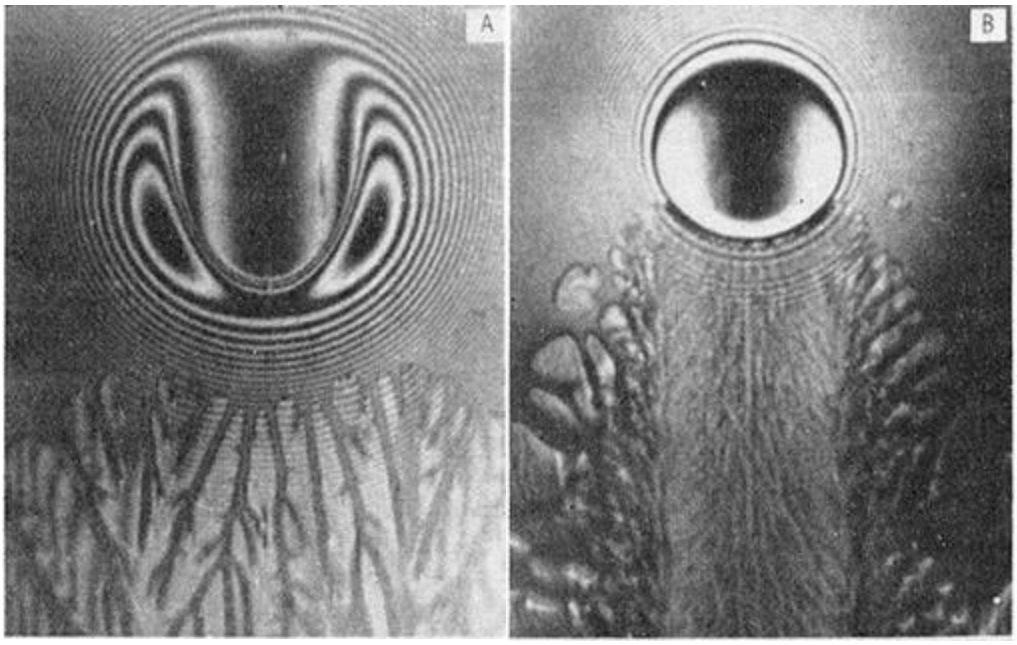

Figure 7. Experimental results adapted from Wedeven et al. [14] showing cavitation "fingers" on left and cavitation bubbles on right.

Cross et al. [15] introduced in 2012 a test rig designed to analyze oil flow in a pocketed thrust washer. A steel disk, featuring 15 holes cut circumferentially, is glued to a clear glass window. The holes act as the pockets, with the back of the hole being the window. They tested with six different runners. The shaft is mounted vertically, and a mirror allowed for a DSLR camera to capture the images. Figure 8 shows the lubricant cavitation that forms in a single pocket. A caviation bubble forms on the leading edge of the pocket, and the size of the bubble grows for increased speeds and viscocities.

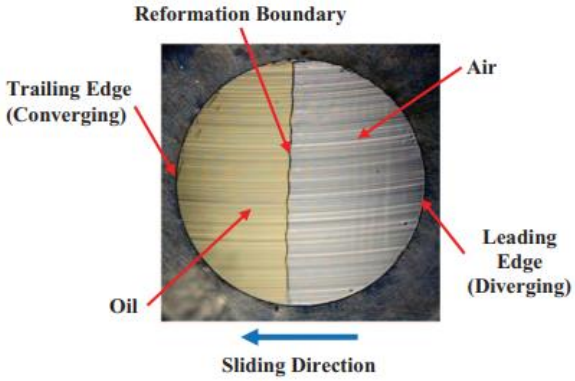

Figure 8. Cavitation area in pocketed thrust washer for high speed test case, adapted from [15].

The authors presented graphs for "cavitated ratio" versus speed and load for six different thrust disk geometries as well as different viscocity oils. The cavitated ratio is defined as the percent of the total area that is cavitated. The coefficient of friction, measured through a torquemeter, increases for increasing spin speeds. Similar trends existed for coefficient of friction and cavitation ratio. Finally, an ANSYS Fluent model showed the pressure contour on the disk for one pocket. Figure 9 shows the predicted and measured lubricant cavitation area for the low load test. Tests were limited to a maximum speed of 500 rpm and 0.148 MPa load.

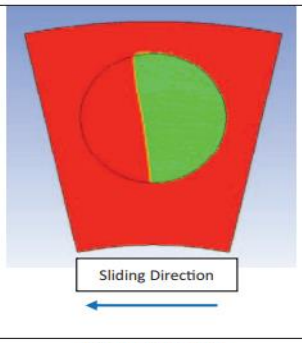

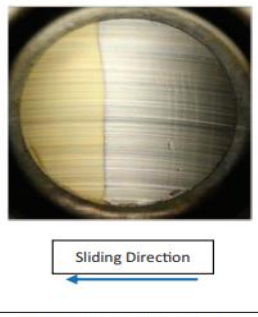

Fluent Model	Experimental Results
Cavitation Area 57.1%	Cavitation Area 61.6%
Load 527.64N	Load 551.38N
NBP 0.1422MPa	NBP 0.1486MPa
Film Thickness 19.3μm	—

Figure 9. Predicted results from ANSYS compared to experimental cavitation area, adapted from Cross [15].

San Andres and Diaz [16] performed optical tests on a squeeze film damper in 2001. The tests were focused on correlating air ingestion on an open ended squeeze film damper and dynamic squeeze film pressure. The test rig utilized an acrylic housing with a high speed camera to visualize the film at different squeeze locations, and at different oil-air volume fractions. Figure 10 displays their results. The images show the development of large striated air pockets. The pockets are largest for the maximum film thickness, and the highest air volume ratio.

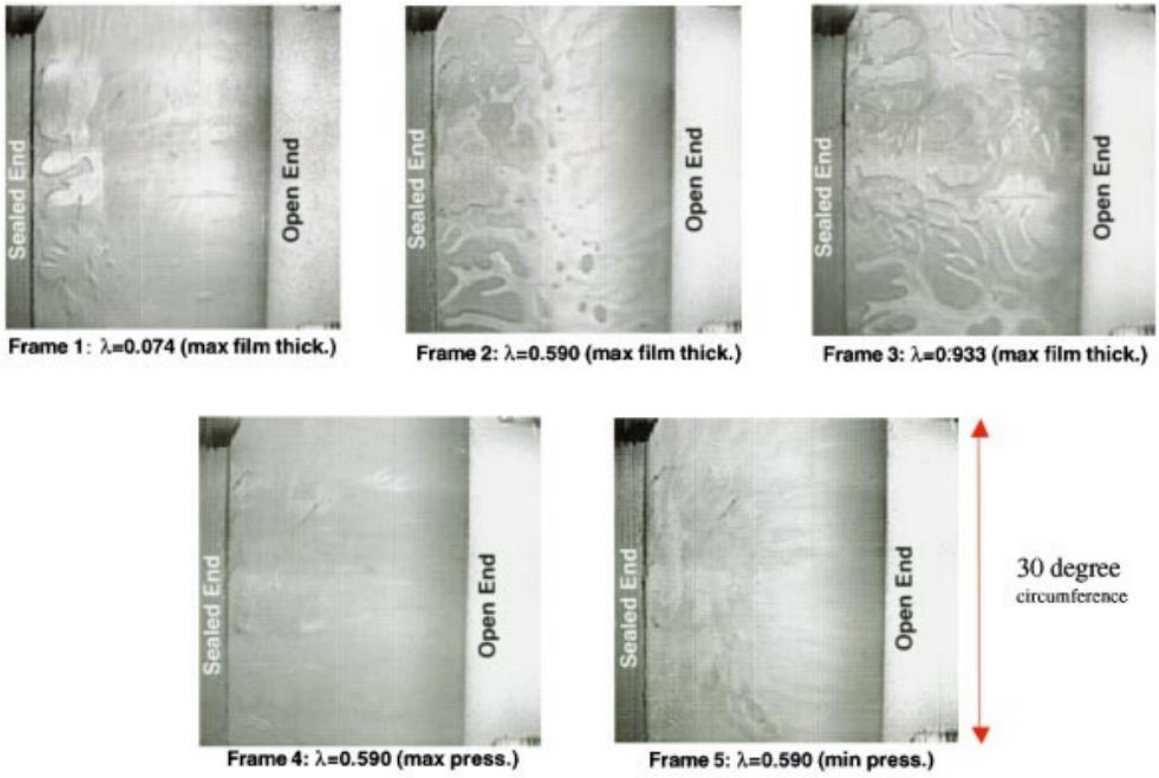

Figure 10. Flow field of squeeze film damper for different film locations and air volume fractions, adapted from [16].

Song et al. [17] described an experimental and numerical study on the effects of lubricant cavitation on a tapered land thrust bearing. Figure 11 shows the test rig, which uses an organic glass thrust bearing that is held stationary, with a spinning metal thrust runner. A hydraulic press applies a constant axial load of 450 N. Tests were conducted at speeds of 2, 4, 5, and 6.7 krpm. The authors used a techniscope to observe the lubricated area between the tapered land bearing and the runner. A flush-mount pressure sensor measures the pressure along the radial direction of the runner.

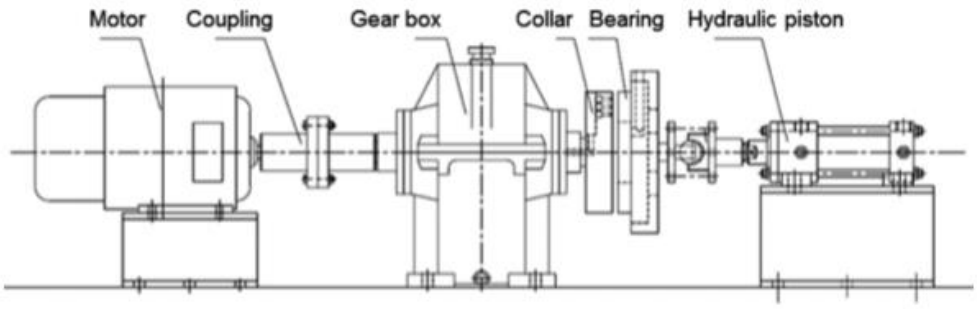

Fig. 1 Diagrammatic view of the test rig

Figure 11. Side view of test rig, adapted from Song et al [17].

Figure 12 shows their results for four spin speeds. They observed a cavitation area at speeds above 2krpm. They also observed air bubbles in the oil mixture. The cavitation area seems to grow for larger speeds. The authors did not show any tests with varying loads.

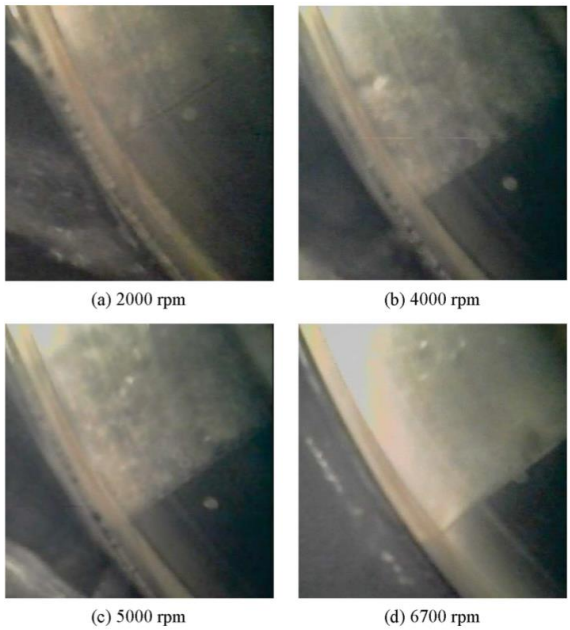

Figure 12. Experimental results from Song et al. [17] showing lubricant cavitation boundary for four spin speeds.

Song et al. [17] also performed a 3D Navier-Stokes solution with combined boundary conditions to predict the pressure profile and gas volume fraction in the thin film lubrication area. Figure 13 shows the pressure profile as well as the cavitation area. They compared their results with a Reynolds equation solution as well as an Elrod's method solution. The predictions from the NSE matched the results from the pressure sensor, especially at low speeds. The gas volume fraction also helped identify where the areas of lubricant cavitation are. The paper listed cavitation as a contributing factor to reduction in load capacity, especially at higher speeds.

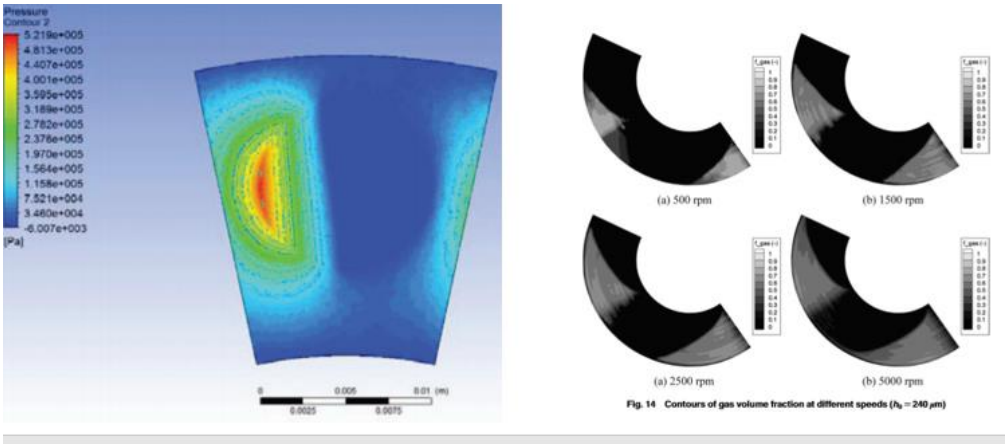

Figure 13. Predicted low pressure areas from ANSYS, adapted from [17].

Modeling of Liquid Cavitation for Turbomachinery Applications

Because of the diverging section of a bearing, the fluid is subjected to a negative pressure, or tensile force. Since fluids do not readily react tensile forces, they instead cavitate, as the pressure drops below the vapor pressure of the bearing. In 2010 Braun and Hannon [18] published a review for cavitation formation and modelling for fluid film bearings. They started with a brief

introduction to fluid film modelling starting with Reynolds and Sommerfeld equations. Braun and Hannon described the four types of cavitation as first published by Swales [19] as: travelling, fixed, vortex, and vibratory. And with the exception of vortex cavitation, the cavitation is typically short-lived and very transient in nature.

At some point in the pressure field, the fluid moves from being a liquid to a vapor, this is known as the film rupture. The film reformation boundary is the location where the gas returns to liquid form. There are several different models describing the film rupture-reformation. Figure 14, taken from Ref. [18] shows four different film rupture boundary models. The plots display the pressure in the bearing versus the circumferential location along the bearing. The first model is the Gumbel model [20], proposed in 1914. In this model, the pressure is simply chopped once it goes below the cavitation pressure. The second model is the Swift-Steiber model, which allows for the slope of the pressure profile to be zero at the rupture. Neither of these models conserve mass through the cavitated zone.

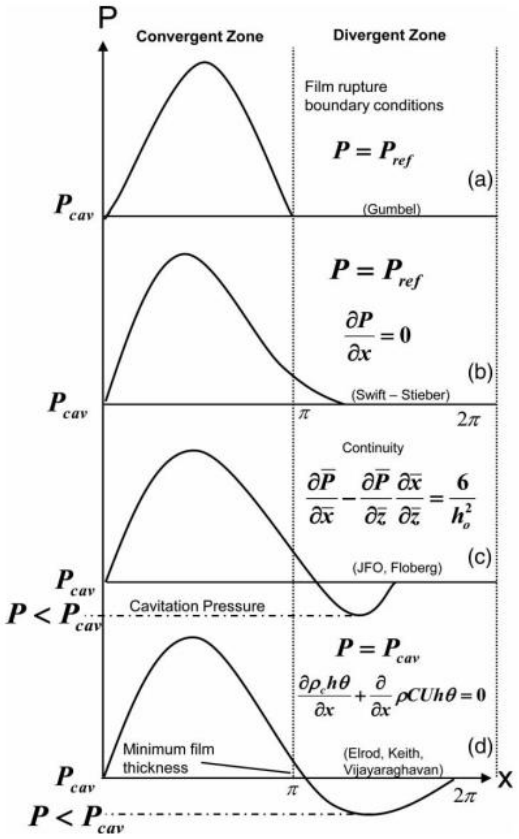

Figure 14. Circumferential pressure development based on film rupture theories: (a) Gumbel, (b) Swift-Stieber, (c) JFO and Floberg, (d) Elrod, adapted from [18]

Jakobson and Floberg [21] presented a mass flowrate expression into the continuity equation on the bubble boundary. They combined the new mass conservation condition with the Reynolds equation to determine a solution that conserves mass throughout the boundary. Elrod [22] introduced a dimensionless density variable, which relates the pressure to the cavity pressure and the new dimensionless density variable. Elrod's method will be described in more detail in chapter 4.

Brewe [25] developed a numerical scheme based on the Elrod algorithm to predict the onset of cavitation for a journal bearing submerged in an oil bath. The results were then compared to

experimental results from Jakobsson and Floberg [23]. The housing was made of a plastic (PMMA) for viewing purposes. The analytical results slightly underpredicted the extent of lubricant cavitation, but the predictions correlate well to the experimental results. Several adaptations to Elrod's method have allowed for complicated geometries [23] transient solutions [24], and oscillatory movement of the rotor [25].

Since Braunn and Hannon published their review in 2010, several new papers have been published on cavitation modeling. Li et al. [26] showed a gaseous cavitation model based on air solubility in the lubricant. Their model is compatible with Elrod's method, and predicts whether vaporous or gaseous cavitation is occuring. Song et al [27] confirmed the work done by Li et al. [26] by comparing the model to previously published results. The model accurately predicts the onset location and total cavitation area. The results are nearly identical to predictions using the JFO condition. Woloszynki [28] presented a more efficient solution to the cavitation problem using a reformulated discretized cavitating flow with complimentary constraints. Brunetiere [29] provided a general model for gas and liquid lubrication for a homogenous mixture using rheological parameters. Bayada and Chupin [30] solved for the pressure across the film assuming both the vapor and liquid are compressible, treating the film as continous.

Studies on the Inlet Region and Boundary Conditions of Machinery Lubricated from Oil Nozzles

Dai et al. [31] showed the importance of lubrication nozzle location, flowrate, and inlet velocity, for proper gear meshing. The authors completed CFD simulations using a turbulence and muli-phase model of a small scale industrial gear train. Their CFD model captured both gears, and a large control volume (simulating the casing). The model predicted different results for different nozzle inlcination angles and offset distances. The percent volume and oil pressure at the gear

mesh interface location were different for each jet arrangement. The authors also built a test rig and measured the temperature of the gear mesh with an infared temperature gun. The nozzle arrangements that had the highest predicted oil volume fraction had the lowest temperature in the tests. The authors showed the importance of proper jet lubrication performance for machine reliability and fatigue life.

Zeng et al. [32] modeled the air oil mixture at the inlet of a high speed ball bearing. The paper uses the volume of fluid (VOF) method developed in the 80s by Hirt and Nichols [33]. The authors determined the oil-to-air volume fraction inside the casing of a ball bearing. They also built a test rig to verify temperature predictions. The ball bearing had four nozzles providing lubrication oil to the system. The sides were open to atmosphere. Figure 15 displays the oil vollume fraction results for a bearing that has only one inlet nozzle. Oil makes 20% of the volume near the nozzle outlet, but quickly dissipates to the atmosphere. The authors suggested using at least four nozzles in the bearing to maintain a high oil volume fraction throughout the bearing.

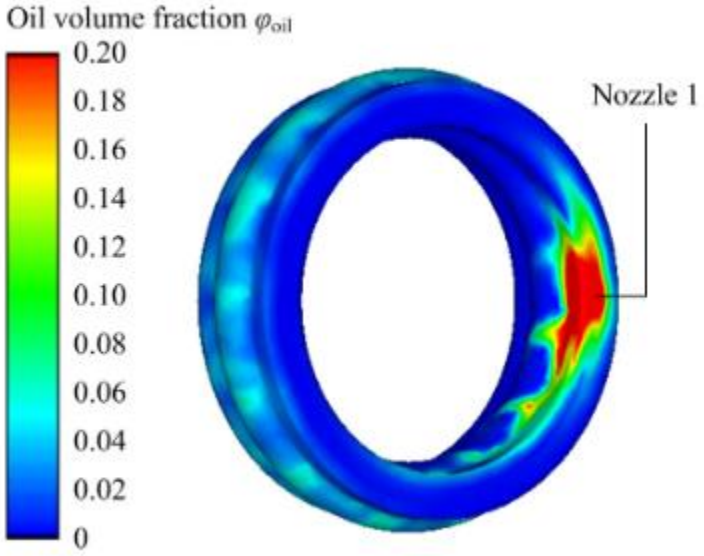

Figure 15. Oil volume fraction inside ball bearing with one nozzle, adopted from [32].

Yazdani and Soteriou [34] presented a novel approach to modeling the oil lubricating a geared system. Their model uses a coupled two phase VOF with the energy equation to predict the temperature rise in the oil. Figure 16 shows a non-dimensional temperature term in the oil for two separate spin directions. The nozzle that supplies oil in the spin direction has a smaller temperature rise than the spray that flows against the spin direction. The authors also showed the effect of oil jet velocity on maximum temperature rise within the gearbox. The results showed that an increased inlet jet velocity yields a smaller temperature rise in the gears.

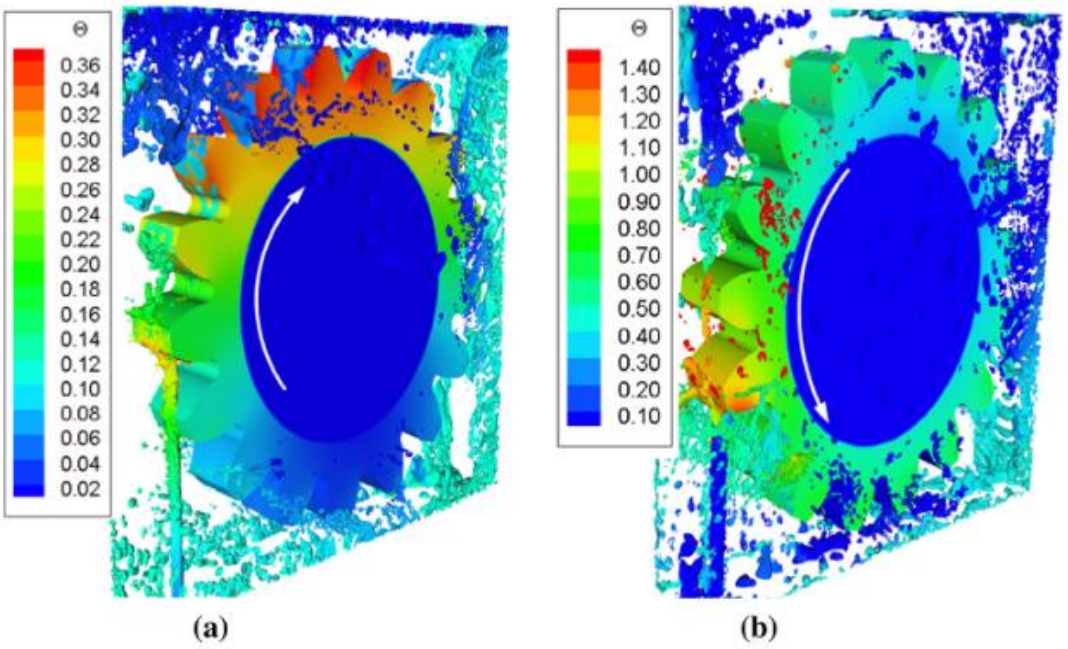

Figure 16. Temperature response of lubricating oil for two spin directions: with inlet velocity (a) and against (b) , adapted from [34].

Manshoor et al. [35] conducted a three dimensional computational fluid dynamics (CFD) study on a standard journal bearing, analyzing three different flow turbulence models. The authors

concluded that the type of model has little effect on the pressure field inside the bearing. They did not compare their results to any experimental work. Zhu et al. [36] showed a CFD model of an aerostatic journal bearing with vortex shedding. They modeled the inlet with a set pressure and a turbulence intensity of 1, 5, and 10%, and atmospheric pressure is set at the outlet. They concluded that vortex shedding leads to pressure fluctuations that can affect bearing vibrations. They built a small test rig and obtained good correlation between experimental data and their predictions. Several papers exist on CFD studies of turbulence in seals. Xu et al. [37] showed how turbulence effects in a spiral groove dry gas seal, and Ji et al. [38] conducted similar work on a hole pattern seal.

Lubricant cavitation, flow turbulence, and inlet conditions in bearings has been studied in depth for decades. Analysis on TCs has also been ongoing for decades, yet there remains a deficiency in the literature for a thorough lubrication analysis on TCs, investigating lubricant cavitation, flow turbulence, and inlet flow conditions.

The current work aims at improving the modeling and design of TCs through an experimental and numerical study of the inlet and boundary lubrication conditions. The experiments consist of a visual characterization of the oil film within the TC at specific operating conditions and oil supply velocities using multiple nozzles orifice sizes. A detailed image post-processing provides quantifiable characteristics of the lubricant cavitation and flow turbulence regions[1] within the TC lubricated area (LA). Numerical predictions using Reynolds equation model and CFD complement the experimental results.

[1] The original aim of this work was to evaluate the cavitation region within the TC lubrication area. However, the experimental results revealed there is also a flow region at the entrance of the TC characterized by a local recirculation area and the formation of eddies. This area is referred to

2. TEST FACILITY DESIGN

Facility Overview

Figure 17 shows a rendered view of the thrust collar (TC) test facility at the turbomachinery lab. The test rig design aims at replicating a TC used in a typical industrial integrally geared compressor (IGC). The rig was designed by Andrew Crandall and Dr. Dara Childs, built by Andrew Crandall, and is described fully by Kerr [13]. The primary difference between the rig and a production IGC is the absence of a geared connection between the pinion shaft and the bull gear shaft. Instead, two separate motors spin the shafts to a predetermined speed, according to an "assumed" gear ratio. Variable frequency drives (VFDs) allow the user to control the speed of both shafts, so the test rig is capable of achieving any gear ratio. For the current tests, the pinion shaft spin speed ω_H spins 11.67 times faster than the bull wheel shaft speed, ω_L, which is a number equivalent to what would be seen in a production IGC.

as a "turbulence" region. The size and turbulence intensity of this region is mainly a function of the supply oil flow velocity.

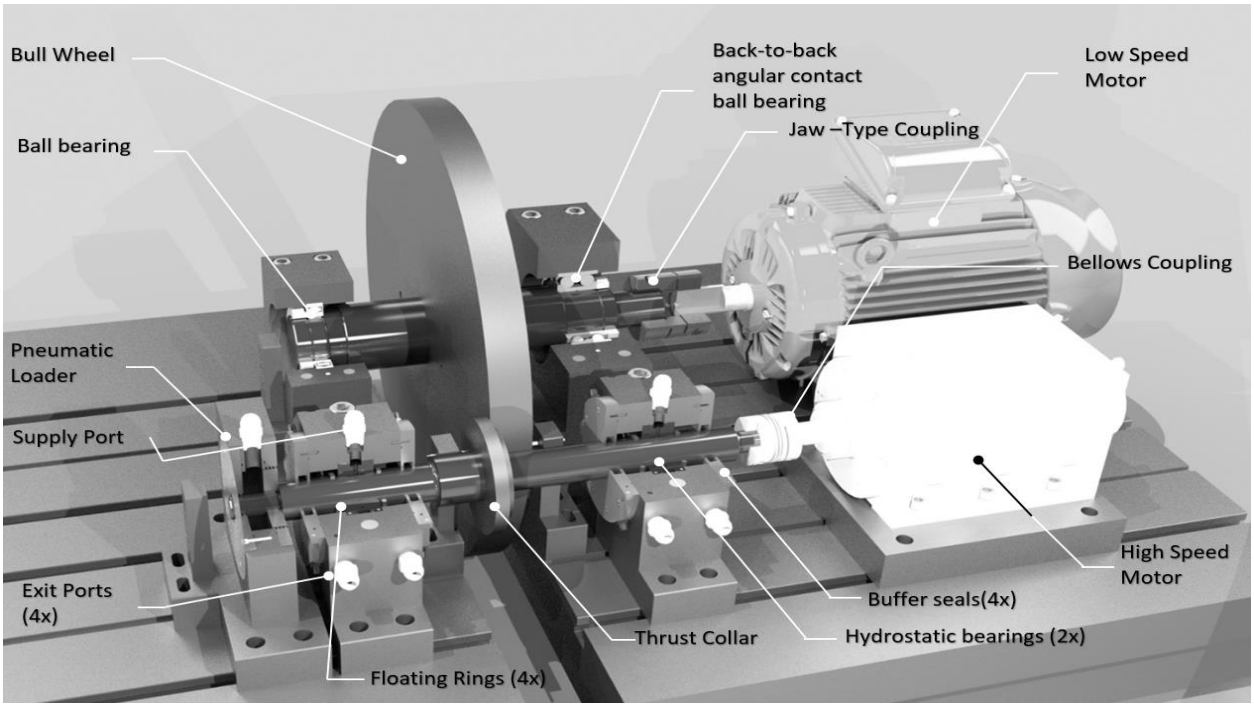

Figure 17. Rendered view of TC test facility at Turbomachinery Laboratory.

Two high pressure hydrostatic bearings provide lateral support for the high speed shaft (HSS), while also allowing axial movement. A pneumatic loader applies an axial force (F_{TC}) on the pinion, which is transferred to the bull gear shaft through the TC and is reacted through two back-to-back ball bearings. The bearing and TC lubricant is supplied through an accumulator, so that in the event of a shut-down the system can coast down safely.

Table 1 displays the TC facility geometries, and maximum capabilities with respect to speed and load. The geometry of the TC overlap area can be completely defined by the radius of the TC (R_1) and the BW (R_2), the taper angle on the face of the TC (Φ_{TC}) and BW (Φ_{BW}), and the distance between the two shafts (d).

Table 1. TC geometry and maximum capabilities.

Description	Value
F_{TC}	2.67 kN
ω_L	3.6 krpm
ω_H	20 krpm
R_2	342 mm
R_1	60 mm
$\Phi_{TC} = \Phi_B$	2°
d	380 mm

Figure 18 shows the overlap between the TC and the BW, where the dashed black lines represent the lubricated area (LA). The figure is not drawn to scale but shows the TC and bull wheel (BW) radius and spin direction. The oil nozzle supplies oil to the underside of the TC overlap area. The upper side of the TC has a diverging film thickness which creates a low pressure area often leading to lubricant cavitation. This section of the TC is shown by the dashed red lines.

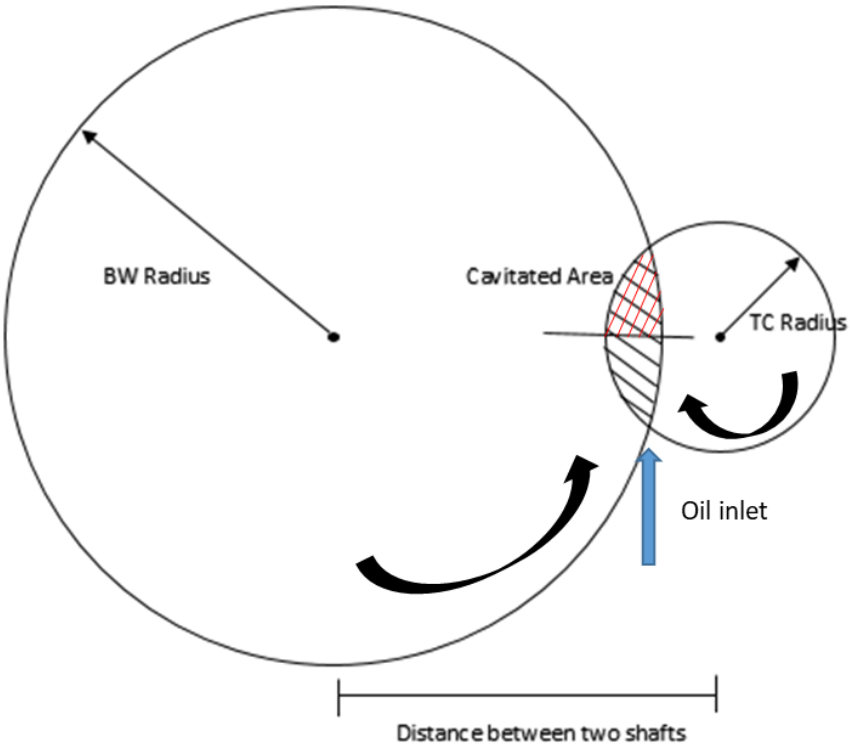

Figure 18. Overlap area between TC and BW showing location of diverging section and oil entrance section.

The area of the overlap is determined from

$$A_{TC}=\frac{1}{d}\sqrt{4d^2R_{TC}-\left(d^2-R_2^2+R_1^2\right)^2} \quad (1)$$

where the specific load is

$$F_o=F_{TC}/A_{TC} \quad (2)$$

The three static, axial forces tested are F_{TC} = 500, 1,000, and 1,500 N which correspond to unit-loads of F_o = 7.8, 11.6, and 15.5 bar.

Transparent TC Design

Figure 19 shows the TC machined to accommodate a high strength acrylic window. The picture on the left is the solid model, and the picture on the right shows the entire pinion shaft. Making

the entire TC out of acrylic instead of just one window ensures that there are no steps on the face of the TC. The taper angle on the TC is 2 degrees with a tolerance of ±0.1 degrees. Each window in the steel backing has a width of 24 mm, and spans 110°, ensuring at least one full observation of the lubricated area, when positioned correctly.

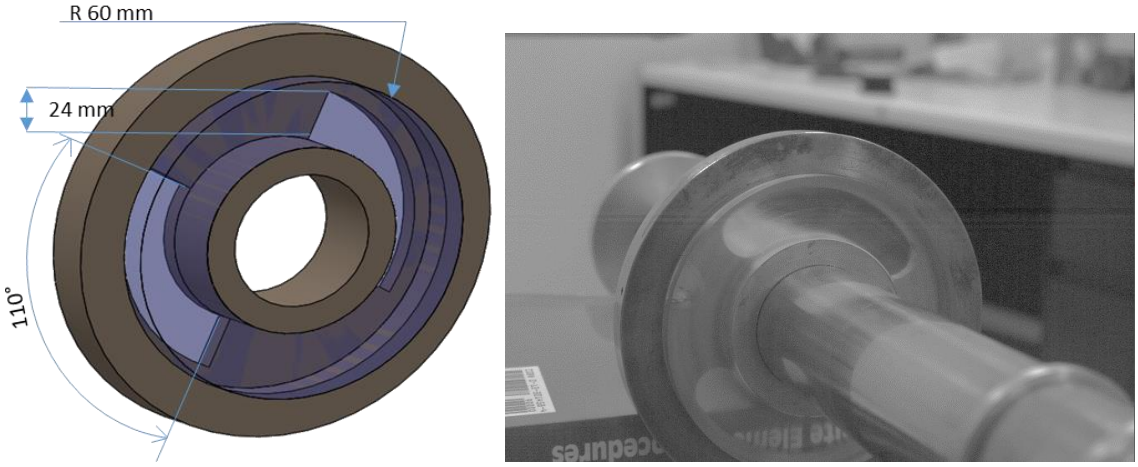

Figure 19. Model of TC with acrylic window (left) shown next to a picture of the actual TC (right).

Figure 20 shows the pinion shaft installed in the test rig. As the pinion shaft spins the lubricated area will be fully visible twice every rotation. The window size is slightly larger than the lubricated area, so that the entire field can be visualized. The steel backing, which can obscure the view, is necessary to minimize the deflection of the acrylic window.

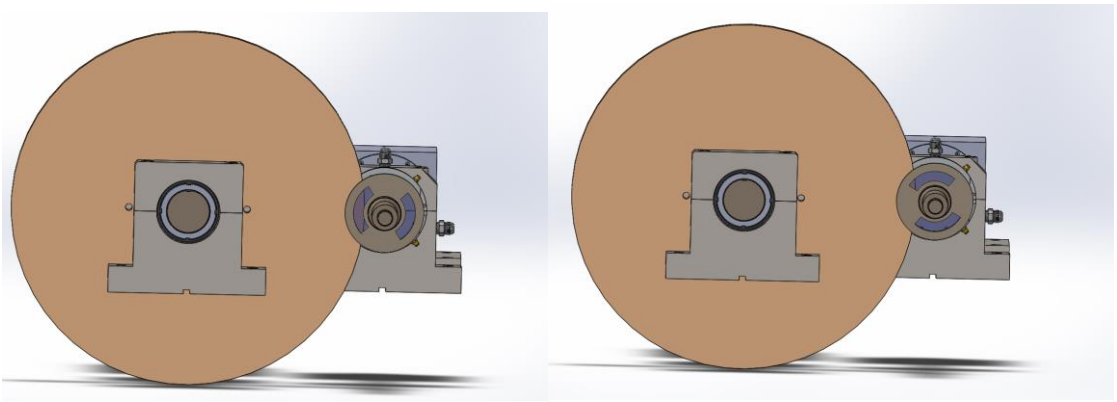

Figure 20. Model of the TC test facility showing viewing area when window is aligned with lubricated area (left) and out of line (right).

Figure 21 shows a stress and deflection of the TC from a finite element (FE) analysis. The picture on the left is a TC that is completely made of 2120 steel, and the picture on the right shows the new TC with the acrylic window. The applied force is 7.5 kN (80 bar), which is the highest load the pneumatic loader can supply. The red dots show the general location of the pressure field, and the arrows show where the TC is rigidly fixed. The deflection of the TC with the acrylic window is twice as high as the steel, but is still relatively small, 0.15 mm (6 mils). The steel backing behind the window helps to minimize deflection. The deflection results in a local increase of the taper angle of 0.089° (which is less than the machining tolerances of ±0.1°)

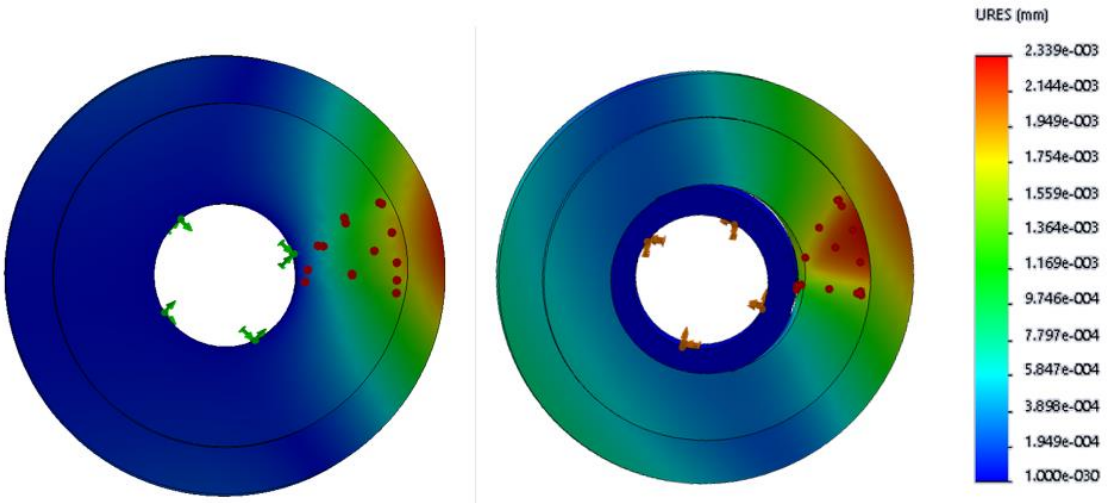

Figure 21. Numerical FEA results showing the deflection of the TC made entirely of steel (left) and with acrylic window (right).

The contact face of the TC is machined to have a similar surface finish to the face of the BW. The surface finish of the BW and TC at the lubrication area is machined to 16 microinches, well below the minimum film thickness. The different surface materials should not affect the TC hydrodynamics. Jacobson and Hamrock [39] conduct cavitation experiments on a journal bearing with an aluminum shaft and a shaft made from PTFE. Their results show that the size and form of cavitation does not change between shafts with different surface roguhness profiles. While their results show that the surface material can effect the fine inner structure of the cavitation, this only occurs at the highest eccentricity ranges when the film thickness is equal to the surface roughness of the materials.

High Speed Monitoring Equipment and Setup

The non-drive end (NDE) hydrostatic bearing does not allow to locate the HSC in line with the TC window. Furthermore, there is only an 8 centimeter gap between the back of the TC and the front of the bearing pedestal. Due to the given space constrains, the camera was placed vertically.

Figure 22 displays the high speed camera (HSC) arrangement including a mirror placed at a 45 degree angle to capture the LA. A magnetic stand supports the mirror in place and allows for small angular adjustments.

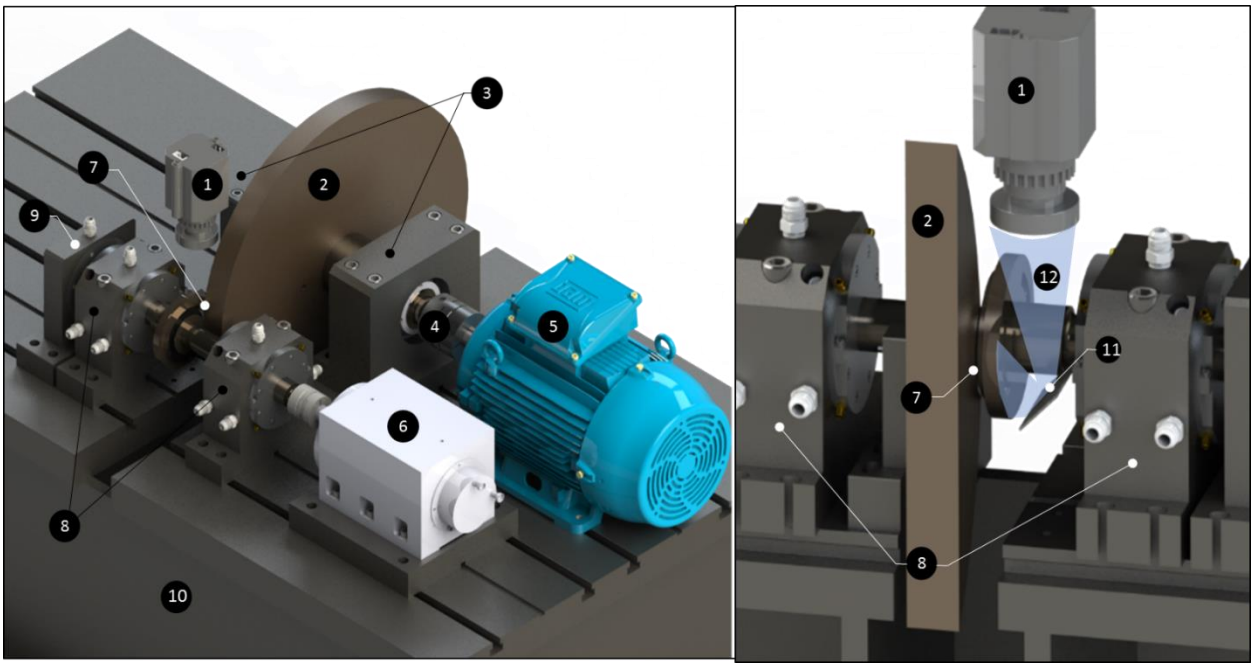

Figure 22. Solid model TC test facility showing main components and cut-view depicting high-speed optical set-up. (1) High speed camera, (2) Bull wheel, (3) BW shaft ball bearings, (4) jaw-type coupling, (5) Low speed motor, (6) High speed motor, (7) Transparent TC, (8) Hydrostatic bearings, (9) Pneumatic loader, (10) Bedplate, (11) Mirror, (12) Visualization path.

Figure 23 shows a picture of the HSC on an adjustable camera stand, as well as the mirror. The camera is a V711 phantom camera, able to capture images at over 100,000 frames per second (fps); the camera captures images in black and white (mono). The camera uses a canon EF 100 mm lens to capture only the area immediately surrounding and including the mirror. There are three settings from the camera control software that determine the quality of the captured images: aperture,

frame-rate, and exposure time. The aperature of the lens controls the focal depth of the camera. The higher the aperature, the larger the depth the camera can focus on, but the less light the lens will let in. Once the aperture is set, the phantom camera control (PCC) software sets the focus of the camera. The focal distance is the summation of the height of the lens above the mirror and the distance between the mirror and the oil film, close to 0.58 m (number twelve in Fig. 22).

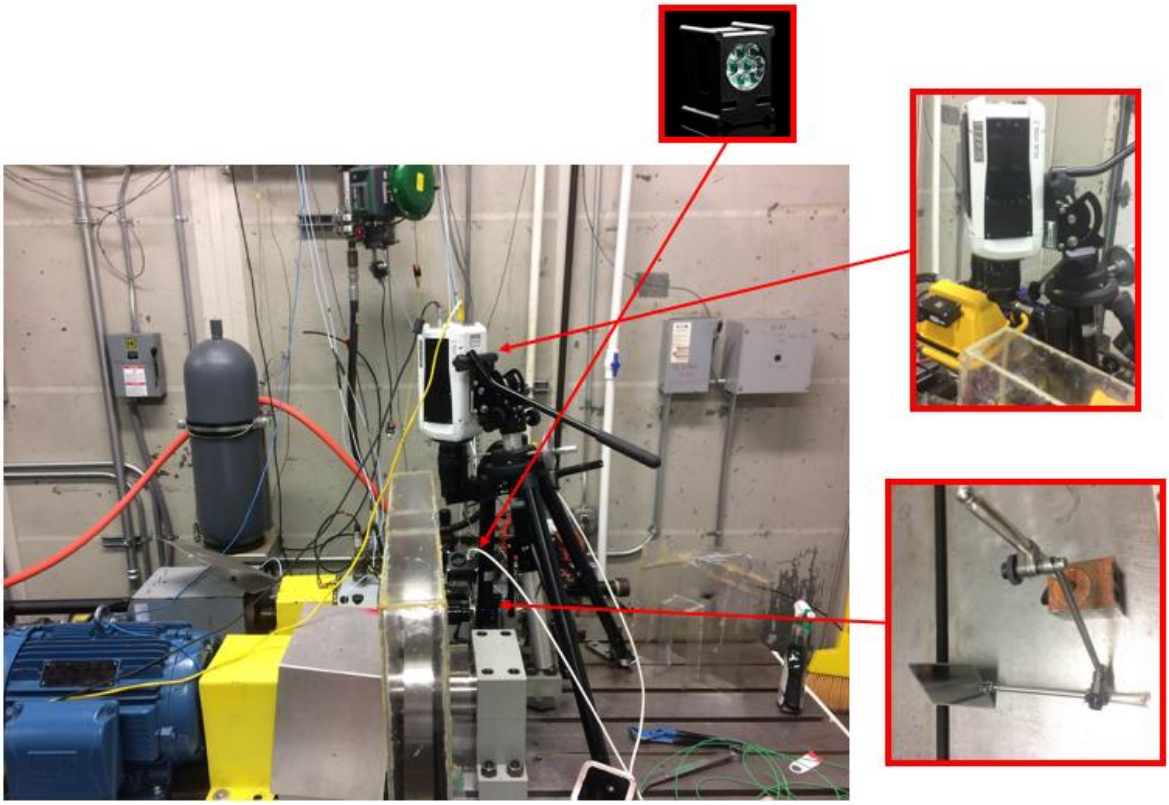

Figure 23. Test set up highlighting HSC on adjustable camera stand and adjustable mirror.

To capture each window as it passes by the camera, the framerate only needs to be twice the speed of the shaft. But to capture any transient data of the fluid within the window, the framerate (FR) needs to be

$$FR = \frac{\omega_{TC} * r_l * N_{shots}}{c} \quad (3)$$

where c is the height of the LA, and N_{shots} is the number of necessary images to describe the fluid flow, typically at least 5.

Exposure is the amount of light per unit area that reaches the camera lens. The chosen framerate directly controls the maximum exposure time allowed by the camera. When the framerate and aperture is high, there may not be enough light entering the lens for the camera to read the data. Figure 24 shows one of two high power LED lamps used to luminate the TC LA. The lights provide 7,000 lumens each. These provide directed, continous, white light, and are oil-resistant.

Figure 24. High power LED lamps used to illuminate the LA.

Oil Delivery System

Figure 25 shows the spray bar mounted directly under the overlap area. A VFD controls the two-horsepower pump, which enables the user to prescribe a flowrate up to 30 liters per minute. Covers and compressed air help contain and return the oil back to the internals of the bedplate, which acts as a reservoir. Testing involved modifying the spray applications for a test matrix

comprising five flow conditions. Figure 25 shows one nozzle test case (4.5 mm opening). The flow floods the underside of the TC with ISO VG 32 oil from a 12.7 mm diameter open tube or nozzle (4.5 mm, 2.2 mm opening).

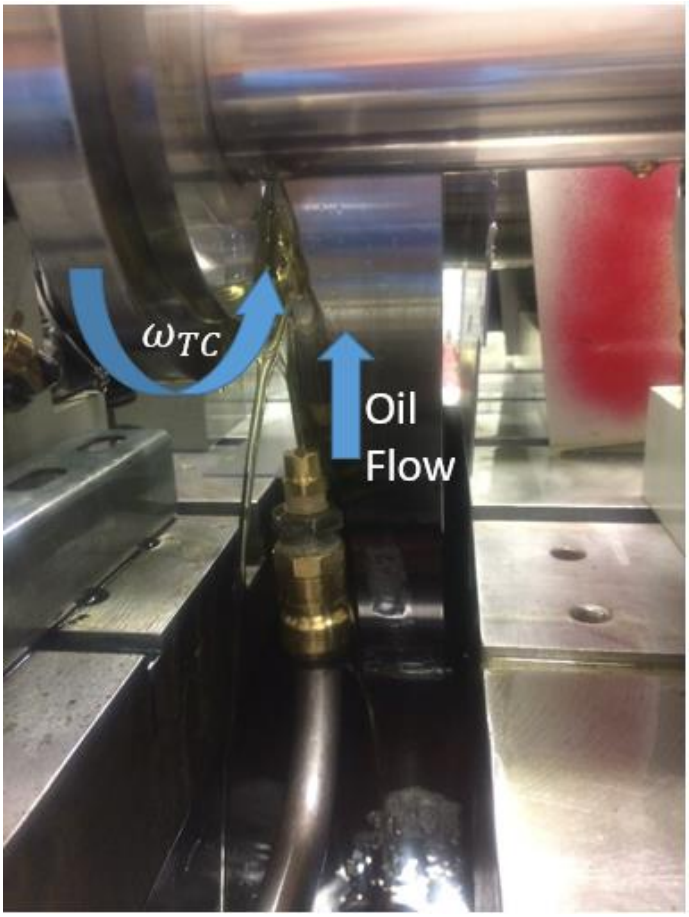

Figure 25. Under mounted spray bar with 4.5 mm nozzle in aligned position, showing oil flow and disk spin direction.

The open tube or nozzle is positioned directly below the TC LA so that the velocity of the oil does not decrease, and so the oil stream remains uniform. Figure 26 shows the oil entering the LA while neither shaft is spinning. The oil flowrate is set to 15 liters per minute. Without any rotation

of the shafts, there is no shear force helping the oil to flow through the LA, so the oil only reaches three fifths of the way up the LA. As the clearance begins diverging, there is not enough oil supply to continue flowing up, so there is air in this section. Visually checking for oil in the LA ensures that the nozzle is properly aligned with the TC opening. This image also shows that starvation is not occurring for the given flowrates, since the LA has enough oil.

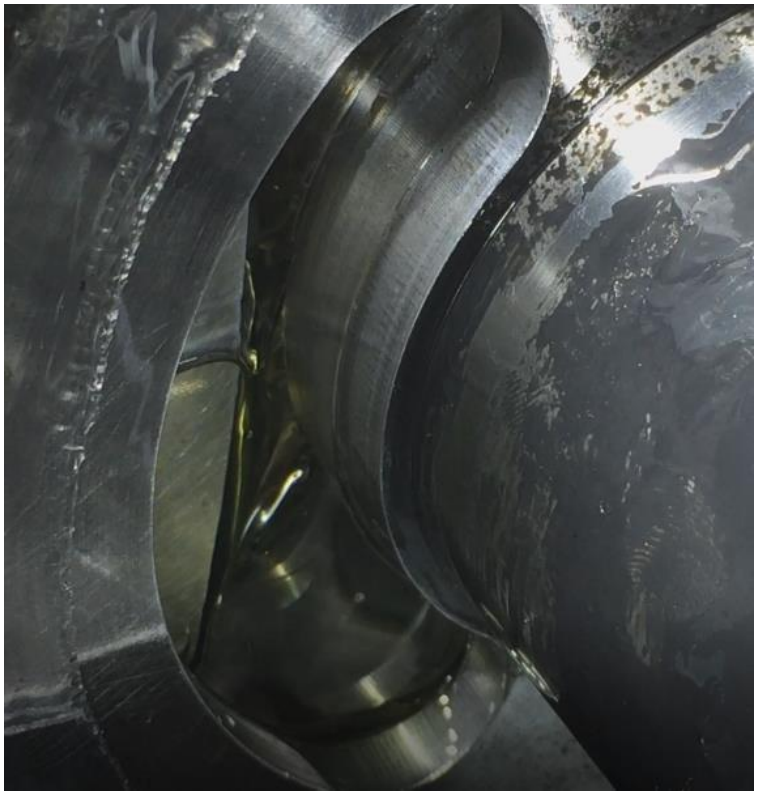

Figure 26. Oil from flat nozzle entering LA with no load and no spin speed demonstrating aligned nozzle.

The velocity of the oil entering the TC is determined from the flow rate and nozzle/tube flow area. The flowrate is measured by a positive displacement flowmeter with an accuracy of 0.5% and a range of 1.9 to 37.8 Liters per second. Table 2 shows oil velocity at the exit of the nozzle for

each test condition. The open tubing condition is only tested at the highest available flowrate (22.5 l/min). The smallest diameter nozzle could only be tested at a flowrate of 7.5 l/min due to pump flowrate / pressure restrictions.

Table 2. Outlet oil velocity for each of the three nozzles tested at each flowrate.

Nozzle \ Flowrate	7.5 l/min	15 l/min	22.5 l/min
Open Pipe (12.7 mm)			3 m/s
4.5 mm	7.6 m/s	15 m/s	23 m/s
2.2 mm	30.4 m/s		

3. EXPERIMENTAL PROCEDURE

This section describes the experimental procedure and methodology of turning raw video footage into quantifiable cavitation and turbulence areas. The experiments consist of recording images of the lubrication area (LA) at relevant operating conditions listed in Table 3.

Table 3. Operating conditions for experimental testing.

Test parameters	Values
Axial load (unit load)	500, 1000, 1500 N (7.7, 11.6. 15.5 bar)
Pinion speed (speed ratio)	2.5, 5, 7.5 krpm (11.67)
Oil supply nozzle	12.7 (open tube), 4.5, 2.2 mm
Flow rates*	7.5 Lpm, 15 l/min, 22.5 l/min
Bull wheel speed	214, 428, 642 rpm

*: Not all flow rate/nozzle combinations were possible. Please refer to Table 2.

The high speed camera (HSC) captures three videos for each test point. The video is broken into images that are filtered, cropped, digitized and turned into a cavitation and turbulence areas. The results are also qualitatively described, analyzing film boundary formation, their precise shape, and changes for varying test points. A detailed description of this process follows.

High Speed Camera Data Capturing

The HSC captures images in monochrome (greyscale). Color imaging requires additional light, since a color camera uses three color filters, where each filter absorbs some of the light. All of the images captured by the HSC have a resolution of 1280 x 800. Each pixel has an intensity value, or grey level, between 0 and 255, because the camera has an 8-bit depth.

Figure 27 shows a single image captured with the HSC. The upper-right side of the picture shows the high speed shaft, while the lower-right side shows the non-drive end (NDE) bearing of the high speed shaft (HSS). The dashed red lines show the mirror (positioned parallel to the thrust collar (TC) and at a 45 degree angle from the horizontal). The dashed blue lines show the LA. The oil is nearly transparent, so the metal seen in the LA is the inside of the bull wheel (BW). The mirror flips the image so that the top of the LA is shown at the bottom of the mirror. The mirror is positioned so that nearly all of the LA can be visualized at once. An interferometer could measure the entire film thickness, locating the minimum film thickness and detect any changes in film thickness with different test parameters. A quote for the required interferometer proved cost prohibitive for this test campaign.

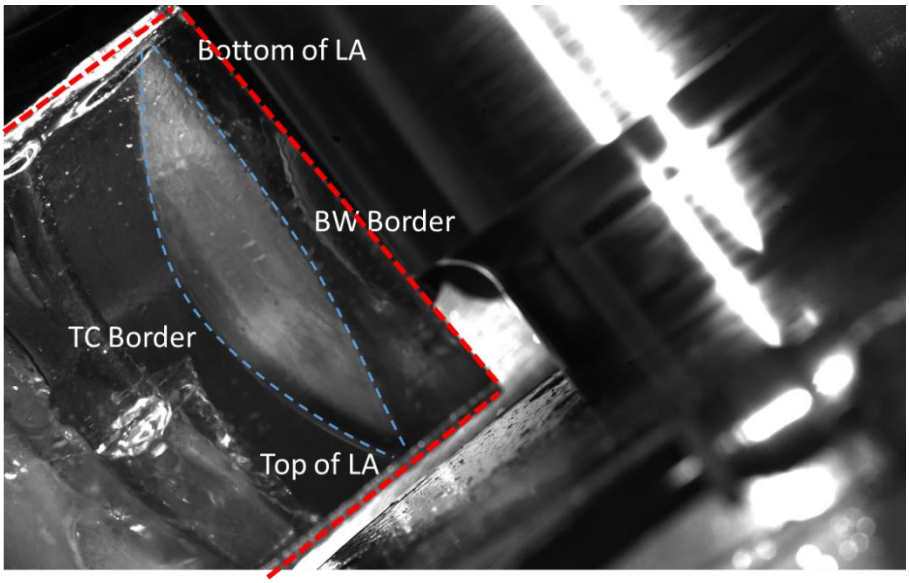

Figure 27. Single unedited image captured from HSC showing location of mirror, edge of TC and BW, and overlap region.

Figure 28 displays a histogram showing the number of pixels at each grey level for Figure 27. Greyscale histogram plots provide insight for choosing a filter to enhance image quality. Most of

the pixels in this plot have a small grey level value, corresponding to a darker image. The image histogram suggests spreading the data and shifting it to a higher grey level for maximum clarity.

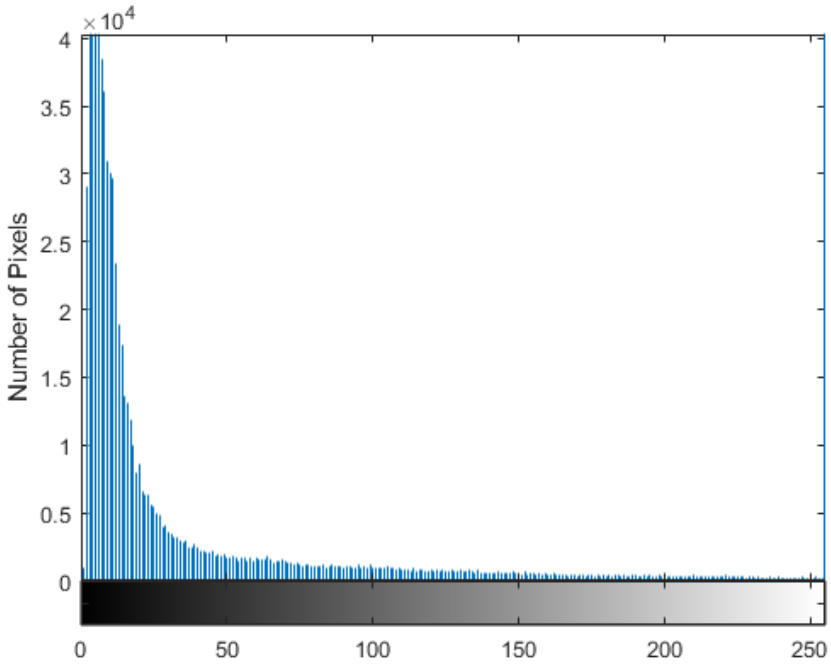

Figure 28**. Histogram showing number of pixels at each grey level for a single image, highlighting the importance of filtering to better spread out data.**

Image Processing

Filtering is applied to an image that has grey-value areas that are too high or too low. Filtering is done once the image is oriented properly, but has not been averaged. Gamma correction is a common filtering technique utilizing a nonlinear adjustment [40] according to a power law equation

$$I_{out}=A*I_{in}^{\gamma} \quad (4)$$

where I is the greyscale intensity, A is a constant (gain) and γ is the gamma value. When images are too dark, a gamma value less than one can brighten them according to the power equation. Table 4 shows the filtering parameters used in this section.

Table 4. Filtering parameters and values.

Filtering Parameter	Value
Gamma (γ)	0.396
Gain (A)	1.574
Brightness (%)	30

Figure 29 shows a single cropped image at $\omega_{TC} = 7.5$ krpm and $F_{TC} = 1$ kN. Figure 29 (a) shows the un-filtered, or raw, image and Figure 29 (b) shows the image with a gamma adjustment. The images have also been rotated vertically and flipped over the horizontal axis to account for the mirror. Gamma adjustments highlight two areas of interest in the TC LA. The first area of interest is the bright area at the inlet region of the TC. A turbulent mixture of oil and possibly some air entrapment characterizes this area. The second area is the bright area in the diverging section of the TC LA. This bright area is an oil vapor-cavitation area in the form of streamers. Characterization of these two areas will be discussed further in the following sections.

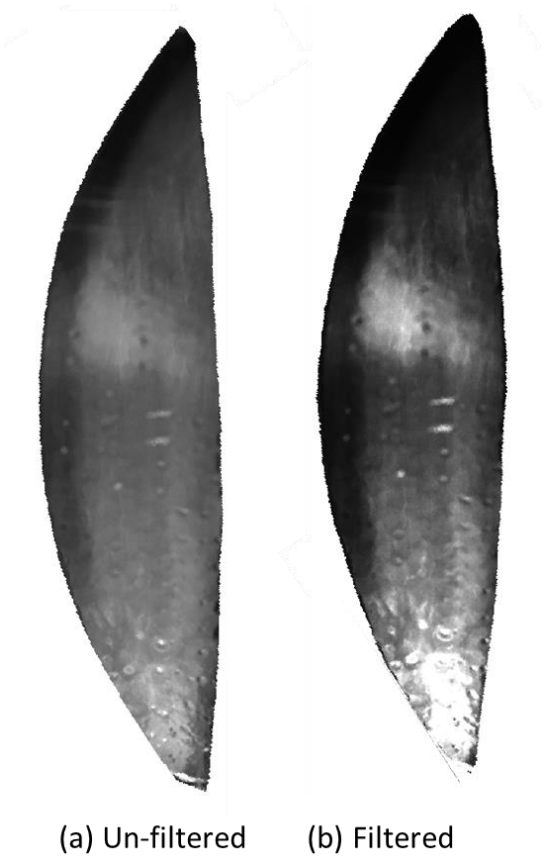

Figure 29. One single frame captured at $\omega_{TC} = 7.5$ krpm, ω_{BW} = 624 rpm, F_{TC} = 1 kN showing unfiltered (a) and gamma filtered (b) showing two locations of flow disturbances.

The HSC captures one second of data. Thus, with a framerate (FR) of 5,000 fps, the video contains 5,000 separate images. At a ω_{TC} of 7.5 krpm, the TC will have rotated 125 times in this one second interval. Figure 30 shows the steps for processing the raw images. This data is at $\omega_{TC} =$ 7.5 krpm and $F_{TC} = 1$ kN. First, 20 separate images are captured (10 from each window) from a single video. The images are then cropped and averaged to obtain a single cropped, averaged picture of the TC LA for each test point. The images still need to be flipped vertically (because of the mirror) and rotated in to a vertical position for comparison to numerical predictions.

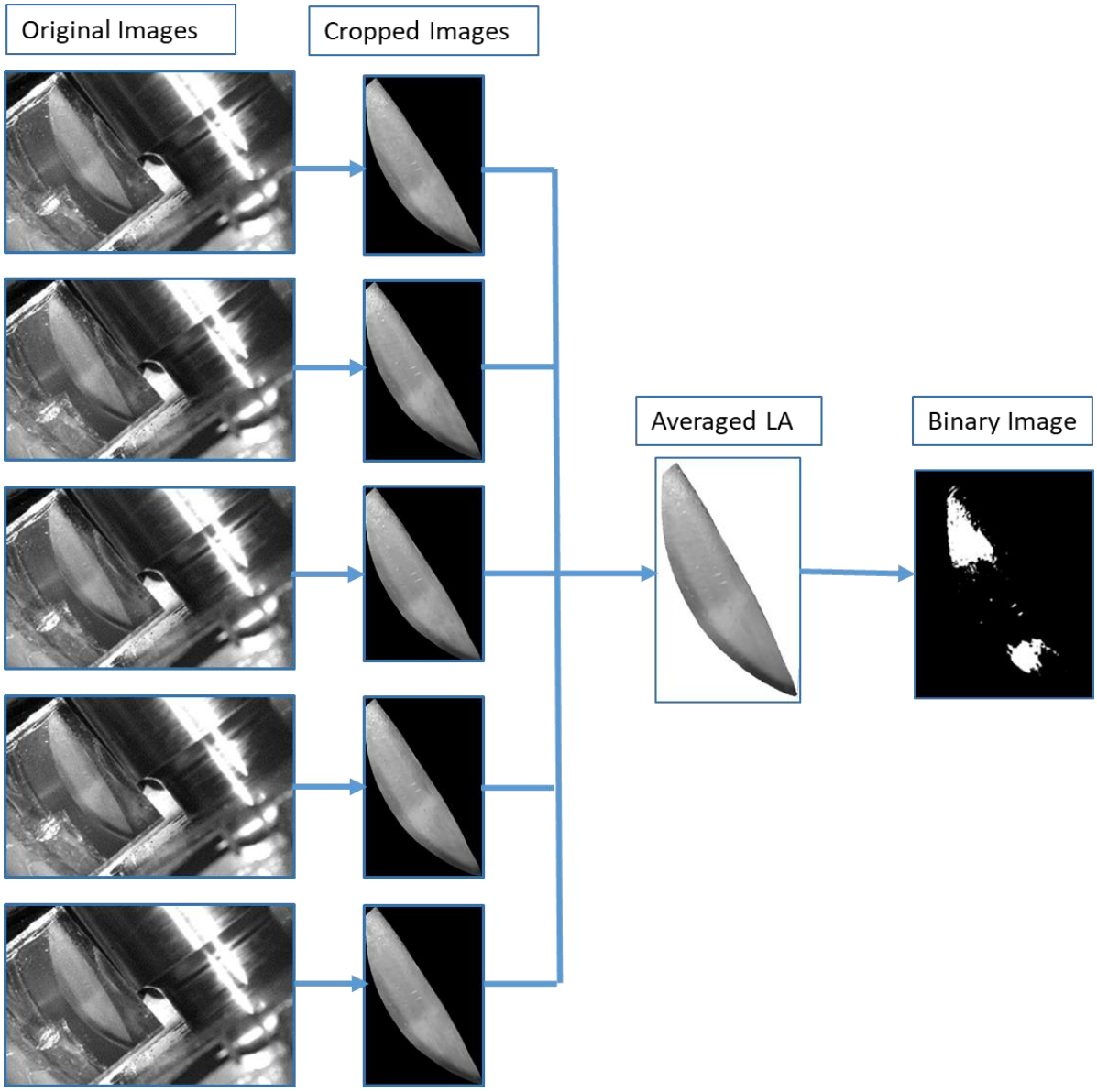

Figure 30. Data analysis procedure, showing averaging, cropping and binary imaging.

Once the images have been cropped and averaged, a binary imaging technique turns the image into black and white values, based on pixel intensity. Otsu [41] describes a technique to determine the threshold intensity based on the cumulative moments of the gray level histogram. Otsu [41]

provides an algorithm that searches every pixel, and determines the threshold value that minimizes the intra-class variance (σ_W), which is determined by

$$\sigma_B^2 = \sigma^2 - \sigma_W^2 \tag{5}$$

where σ_B is the variance in the background and σ is the total variance in the image. Once the image is split into binary form, the averaged flow turbulent or cavitated area is divided by the total area to determine a percent cavitation or turbulence area.

4. COMPUTATIONAL MODELING

This section describes two different approaches to modeling the thrust collar (TC) oil film. The first is a finite element model based on the Reynolds equation, and the second is a computational fluid dynamic (CFD) model using ANSYS FLUENT. Each model offers unique advantages to aid in modeling the TC, and OEMS could utilize either depending on their needs.

The finite element (FE) Reynolds model has previously been used to analyze TCs [12], but this model uses the Reynolds assumption to model lubricant cavitation and does not include deformation of the disks. The current model incorporates deflection and cavitation and is used for evaluating their effect on load capacity. The FE model also allows for quick changes in geometry and spin speeds and is computationally less expensive than a CFD model.

The CFD model is quicker to set up, and solves the flow in the lubricated area in 3 dimensions. The CFD model was utilized to capture complex flow patterns that occur in a three dimensional flow field. Experiments showed a turbulent region occurring in the inlet of the LA that could not be modeled by a two-dimensional approach.

Finite Element Modeling

This section describes a procedure for modeling the TC oil film based on the Reynolds equation using a finite elements approach.

Figure 31, adopted from [12], depicts the TC lubricated area. The following 2D analysis is described in cylindrical coordinates, r and θ, with an origin at the center of the TC, denoted P. R_1 and R_2 denote the radius of the TC and bull wheel (BW), respectively. The lubricated area is shaded in yellow. The distance between the two shafts is d. The height and width of the lubricated area (c and l), and the distance from the center of the BW to an arbitrary point in the lubricated area b can be calculated using the other geometries, where

$$b_{r,\theta} = \sqrt{(d^2 + r^2 - 2rdcos(\theta))} \tag{6}$$

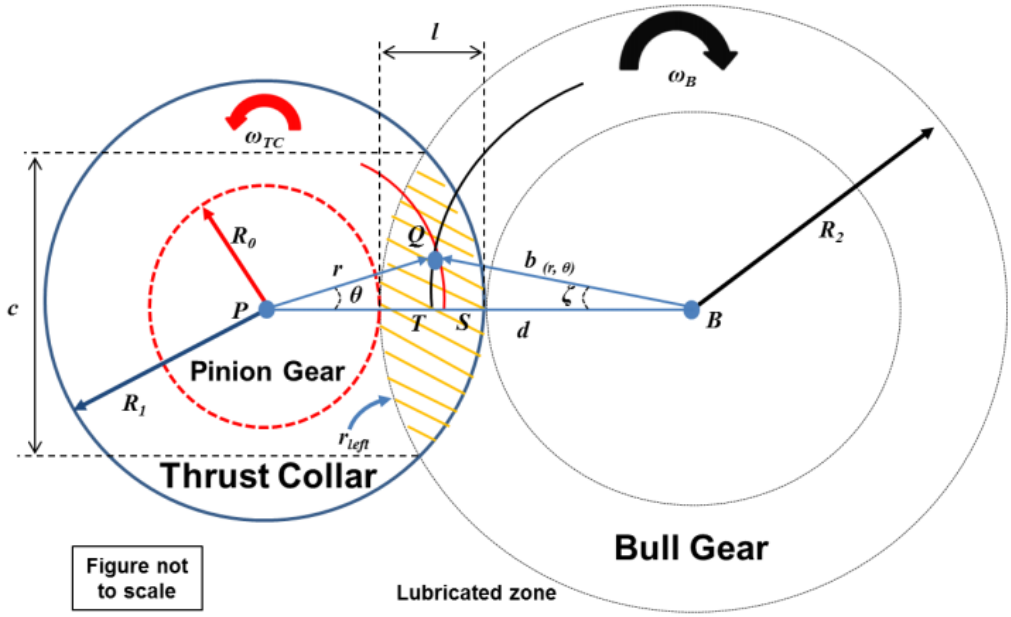

Figure 31. Diagram of TC lubricated zone shown in cylindrical coordinates, adapted from [12].

Cable et al. [12] describe the Reynolds equation for a TC as

$$\frac{1}{r}\frac{\partial p}{\partial r}\left(r\frac{h^3}{12\mu}\frac{\partial p}{\partial r}\right)+\frac{1}{r}\frac{\partial p}{\partial \theta}\left(\frac{h^3}{12\mu\, r\partial\theta}\frac{\partial p}{\partial \theta}\right)=\frac{\partial h}{\partial t}+\frac{1}{r}\frac{\partial}{\partial r}\left\{r[b\omega_B \sin(\epsilon)]\left(\frac{h}{2}\right)\right\}+\frac{1}{r}\frac{\partial}{\partial \theta}\left\{[b\omega_B \cos(\epsilon)+r(\right. \tag{7}$$

where $h(r,\theta)$ is the film thickness

$$h_{r,\theta}=h_0+\left[\left(R_1\text{-}d+b_{r,\theta}\right)\tan\left(\phi_B\right)\right]\text{-}\left[\left(R_1\text{-}r\right)\tan\left(\phi_{TC}\right)\right]$$

Elrod's Method for Cavitation

The model in Ref. [12] uses the Reynolds condition to solve for the boundary of the cavitation zone, where

$$\left(\frac{\partial \mathrm{P}}{\partial \theta}\right)_{\theta=\theta_1} = \left(\frac{\partial \mathrm{P}}{\partial \mathrm{z}}\right)_{\theta=\theta_1} = 0 \tag{8}$$

θ_1 signifies the start of the cavitation boundary. The Reynolds condition ensures that the pressure profile is continuous. Experiments show that the Reynolds boundary condition does not always accurately predict the cavitation boundary. Furthermore, the Reynolds condition does not conserve mass throughout the lubricated area.

Elrod [22] advances a mass continuity equation to solve for the boundary location of the cavitation area called the universal cavitation algorithm (UCA). His approach is based on the Jakobsson, Floberg, and Olsson (JFO) model [21]. In the model

$$\partial P = \frac{\kappa}{\rho}\partial\rho = \mathrm{g}\frac{\kappa}{\alpha}\partial\alpha \tag{9}$$

where k is the liquid bulk-modulus, α is the density ratio, and g is a switch function,

$$g = \begin{Bmatrix} 1 & \text{full film zone} \\ 0 & \text{in cavitation} \end{Bmatrix} \tag{10}$$

The boundary condition on the film rupture and reformation is

$$g = \begin{Bmatrix} \alpha = 1, p > 0 & \text{full film zone} \\ 0 < \alpha < 1, p = 0 & i\text{n cavitation} \end{Bmatrix}$$

Substituting (9) into (7) leads to a new global mass conservation equation

$$\frac{1}{r}\frac{\partial}{\partial r}\left(r\frac{\rho_c h^3}{12\mu}\text{gк}\ \frac{\partial \alpha}{\partial r}\right)+\frac{1}{r}\frac{\partial}{\partial \theta}\left(\frac{\rho_c h^3}{12\mu}\text{gк}\ \frac{\partial \alpha}{\partial r}\right) \tag{11}$$

$$=\rho_c\frac{\partial(\alpha h)}{\partial t}+\frac{1}{r}\frac{\partial}{\partial r}\left\{r\alpha\rho_c b\omega_B\sin(\epsilon)\left(\frac{h}{2}\right)\right\}$$

$$+\frac{1}{r}\frac{\partial}{\partial \theta}\left\{\alpha\rho_c(b\omega_B\cos(\epsilon)+r\omega_{TC})\left(\frac{h}{2}\right)\right\}$$

Olsson [42] solved the continuity equation for a simple journal bearing using a finite difference (FD) approach. Ten years later, in 1999, Kumar and Booker [43] introduce the first prediction using a finite element (FE) approach. Hajjam and Bonneau [44] extend the FE cavitation algorithm to allow for elastic deformation of a lip seal. In their model, the fluidity matrix is solved iteratively for new vectors of g. Meng et al. [45] introduce a new model that does not require recalculation of the fluidity matrix, only an iterative solver for finding the boundary area.

After cancelling out the density and time derivative terms, the Reynolds equation, from (9), becomes

$$\frac{1}{r}\frac{\partial p}{\partial r}\left(r\frac{h^3}{12\mu}\frac{\partial p}{\partial r}\right)+\frac{1}{r}\frac{\partial p}{\partial \theta}\left(\frac{h^3}{12\mu}\frac{\partial p}{r\partial \theta}\right)=\frac{U_r}{2}\frac{1}{r}\frac{\partial}{\partial r}\{\alpha h\}+\frac{U_\theta}{2}\frac{1}{r}\frac{\partial}{\partial \theta}\{\alpha h\} \tag{12}$$

where U_r and U_θ are the velocity terms equal to

$$\begin{aligned} U_r &= b\omega_B sin(\epsilon) \\ U_\theta &= b\omega_B\cos(\epsilon)+r\omega_{TC} \end{aligned} \tag{13}$$

The Galerkin formulation allows for expressing the partial differential equation into a set of linear equations. Expressing Eq. 12 in its weak variational form [46] with *w* representing a bilinear weight function yields

$$\int_\Omega\left[\frac{h^3}{12\mu}\left(\frac{\partial w}{\partial r}\frac{\partial p}{\partial r}+\frac{\partial w}{r\partial \theta}\frac{\partial p}{r\partial \theta}\right)\right]d\Omega-\int_\Omega\left[\frac{1}{2}\left(U_r\frac{\partial(\alpha h)}{\partial r}+U_\theta\frac{\partial(\alpha h)}{r\partial \theta}\right)\right]d\Omega=0 \tag{14}$$

where $d\Omega = \mathrm{rdrd}\theta$. Reddy [46] describes a method for integrating Eq (14) through Gauss-Legendre-Quadratures so that the global set of equations becomes

$$k^G * p = k^T * \alpha \tag{15}$$

where the coefficients of the two matrices are

$$k^G = \int_{\Omega} \left[\frac{h^3}{12\mu} \left(\frac{\partial w}{\partial r} \frac{\partial p}{\partial r} + \frac{\partial w}{r\partial \theta} \frac{\partial p}{r\partial \theta} \right) \right] d\Omega \tag{16}$$

and

$$k^T = \int_{\Omega} \left[\frac{1}{2} \left(U_r \frac{\partial(\theta h)}{\partial r} + U_\theta \frac{\partial(\theta h)}{r\partial \theta} \right) \right] d\Omega \tag{17}$$

Introducing a new complimentary term, first shown by Meng et al. [45],

$$\Phi = g * p + (1 - g)\alpha \tag{18}$$

So that Φ is equal to p in the full film zone and α in the cavitated area. Combining Eq. (15) and Eq. (18) lead to

$$[k^G * g - k^T(1 - g)]\Phi = k^T g \tag{19}$$

The model first builds the fluidity matrices. The area is assumed to be in full film so that g is one everywhere, then Φ is calculated. If Φ is less than the liquid cavitation pressure, g at that node is switched to zero. Φ is solved for iteratively, until the switch function g is no longer changing. The typical solution takes two to four iterations, but because the fluidity matrix does not need to be recalculated, there is minimal additional computational costs.

Figure 32 shows the FE mesh, there are 35 horizontal nodes, and 55 vertical nodes with 1,836 total elements. A higher fidelity mesh with 3,750 nodes produces similar results (within 1%), but comes as an exponentially higher computational cost. The boundary condition states that the pressure is at ambient at each boundary element.

$$P_{boundary} = P_a$$

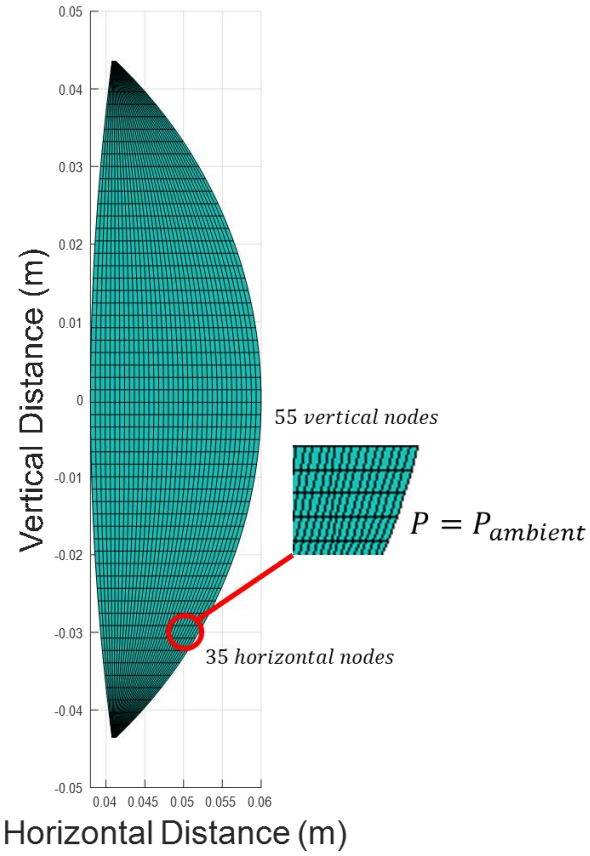

Figure 32. FE mesh, showing horizontal and vertical nodes.

Szeri [47] describes a critical Reynolds number (Re_c) of 2,000 defined for parallel flow by

$$Re_c = \frac{\rho \omega \mathrm{rh}}{\mu} \tag{20}$$

substituting the equivalent surface speed for the TC and BW yields

$$Re = \frac{\rho h}{\mu}(r_{TC} * \omega_{TC} - r_{BW} * \omega_{BW}) \tag{21}$$

where h, r_{TC}, ω_{TC}, r_{BW}, and ω_{BW} are all local parameters. The highest local Reynolds number for $\omega_{TC} = 7.5$ krpm and $F_{TC} = 1{,}500$ n occurs at the top and bottom of the LA, where the film

thickness is the largest. The highest Reynolds number seen in the LA is 930, well below Re_c cited by Szeri [47]. For this reason, the FE model assumes the entire flow domain is laminar.

Elastohydrodynamic Model Including Disk Flexibility

At high loads, local pressures can cause a deformation in the surface of the disks. When the surfaces elastically deform, an elastohydrodynamic (EHL) model is required to capture the film thickness changes described as

$$h_{r,\theta} = h_{R_1} + \left[\left(R_1 - d + b_{r,\theta}\right)\tan(\phi_B)\right] - \left[(R_1 - r)\tan(\phi_{TC})\right] + \delta(r,\theta) \tag{22}$$

where δ is equal to the total deformation of the two surfaces. The deformation is calculated by assuming the convex lubricated surfaces to be two semi-infinite bodies subject to the same pressure distribution [8]. The deflection can be calculated from the pressure field according to the equation [48]

$$\delta(x_1, y_1) = \frac{2}{\pi E'}\iint_{\Omega}\frac{p(x,y)dxdy}{\sqrt{(x-x_1)^2 + (y-y_1)^2}} \tag{23}$$

where Ω is the total fluid domain. E' is the effective elastic modulus determined from the material of the two disks

$$E' = 2\left[\frac{1-v_1^2}{E_1} + \frac{1-v_2}{E_2}\right]^{-1} \tag{24}$$

Table 5 shows the elastic modulus for the acrylic TC and the steel BW (made from 4140 steel). The effective modulus is 7 GPa. In a traditional IGC, both the TC and the BW would be made from steel, so the effective modulus would be much higher (approximately 200 GPa).

Table 5. Effective modulus from acrylic TC and steel BW.

Material / Parameter	4140 Steel	Acrylic
Elastic Modulus	200 GPa	3.1 GPa
Poisson Ratio	0.3	0.36
E'	7 GPa	

The model does not include variation on viscosity due to pressure and the transient nature of the inertia of the disks. Including inertia would likely reduce the deflection amplitude. So these static prediction represents a conservative estimate of surface deflection.

Computational Fluid Dynamic Modeling Using ANSYS FLUENT

This section presents a procedure for modeling the thrust collar (TC) lubricated area (LA) using ANSYS FLUENT. Figure 33 shows the TC LA mesh used in the computational fluid dynamics (CFD) analysis. The boundaries are set by the radius of each disk. The left side of the figure shows the curvature caused by the radius of the TC, and the right, the BW. The LA is the overlap between the two disks. The mesh is broken into 100 elements from top to bottom and eight elements across the film thickness.

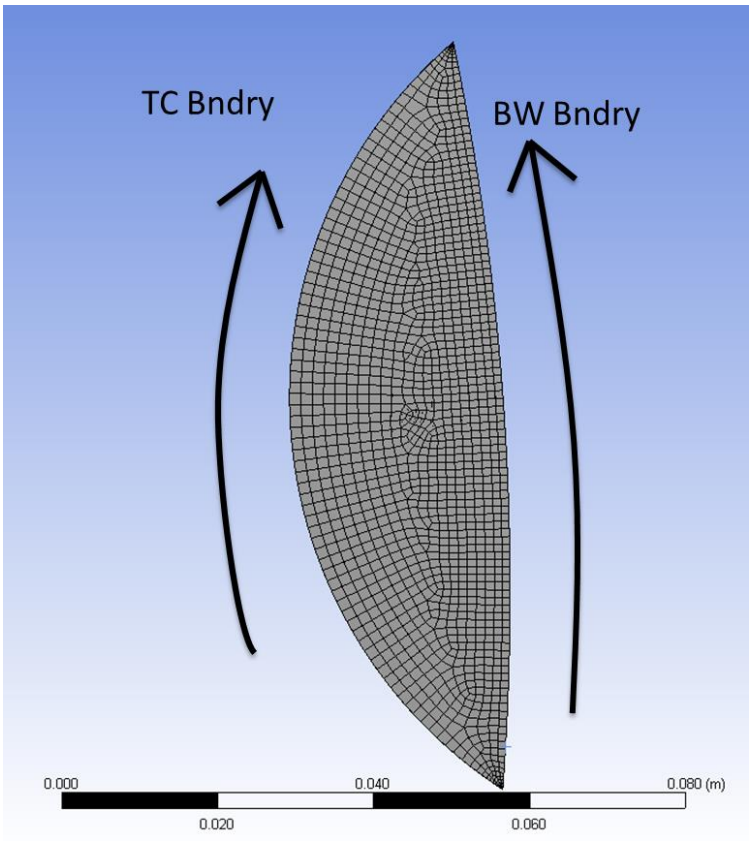

Figure 33. TC LA mesh for CFD from front showing disk boundaries.

Figure 34 displays a side view of the LA mesh. From this angle it is easy to see the converging-diverging wedge that creates the pressure field. The flow direction is from right to left, and is due to the drag force from the surface of the BW and TC. There are 8 elements across the flow thickness. The figure also shows a close up view of the mesh highlighting the eight elements across the film thickness. The elements in this direction allow for a 3-dimensional analysis. A mesh independence study (tested at ½, 2, and 4 times the mesh density with results that matched withing five percent), along with good convergence proves the quality of the mesh.

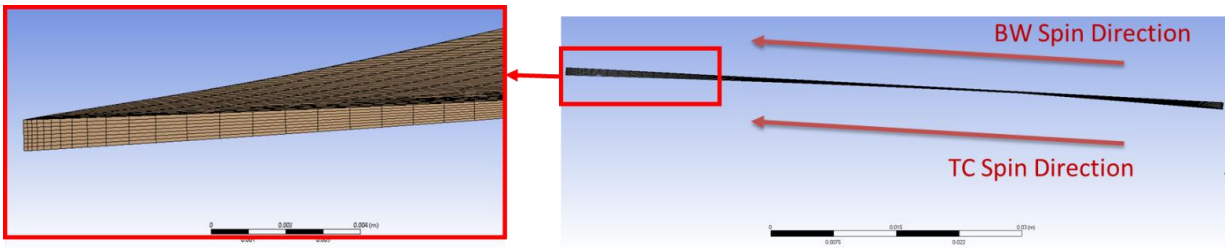

Figure 34. Side view of the LA mesh including elements through film.

Figure 35 displays the velocity of the fluid in the first element near the surface of the TC (left) and the BW (right). For this test case, $\omega_{TC} = 7{,}500$ rpm and $\omega_{BW} = 642.6$ rpm. There is a no slip condition, so the fluid velocity at the surface is the same speed as the surface of each disk. For an IGC, the geared connection ensures that the surface speed of both the TC shaft and BW shaft at the gear location is equal. The smallest velocity of the TC surface (25.5 m/s) is larger than the highest surface speed on the BW (23.0 m/s). And the max TC surface speed is substantially higher (50 m/s). Two things cause the surface speed on the BW and TC surface to be different. The first is the gear ratio where ω_{TC} is larger than ω_{BW} (11.67 times greater). The speed of the TC surface varies by 4 m/s (from the edge of the TC to the more central location in the LA), where the variance on the BW surface is small. The second is that the gear location is at the edge of the BW and on the TC shaft, where the TC extends laterally past the gear location.

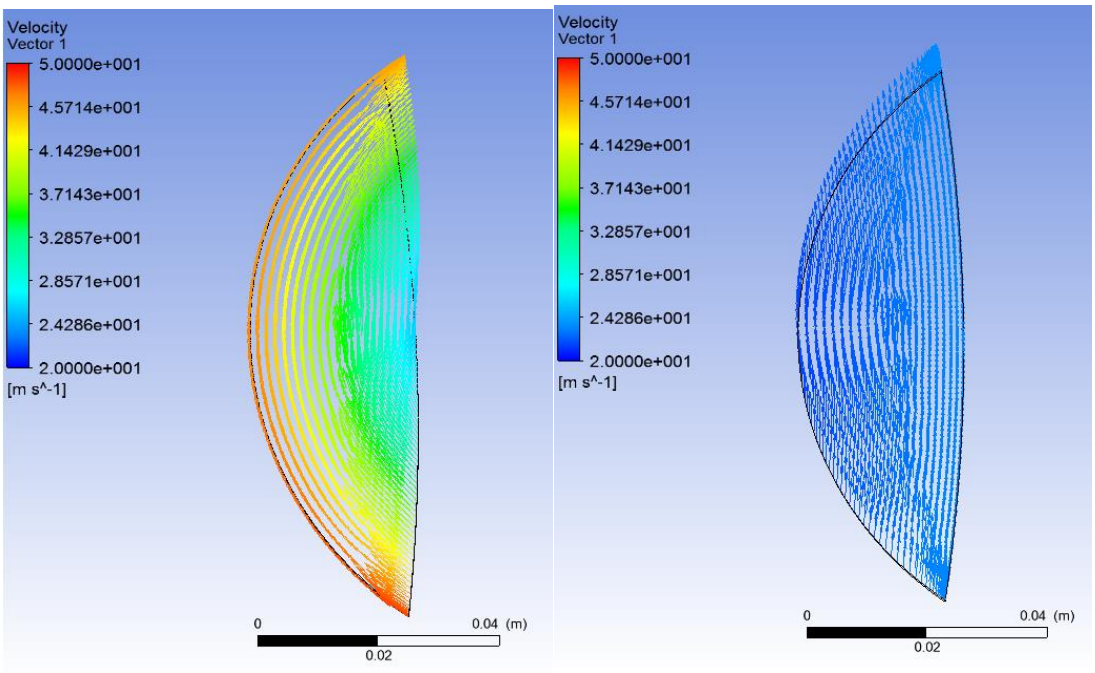

Figure 35. Velocity fields near the surface of the LA from the TC (left) and BW (right).

Figure 36 shows a magnified view of the velocity vector on the faces of the TC and BW at the top of the LA. The curvature from the TC radius is larger than the curvature from the BW side. At the top of the LA, the velocity direction on the TC face is almost completely horizontal, where the velocity direction from the BW surface is nearly vertical. The difference in velocity directions is highest at the bottom and top of the LA. This difference in direction promotes the formation of turbulence at the entrance region.

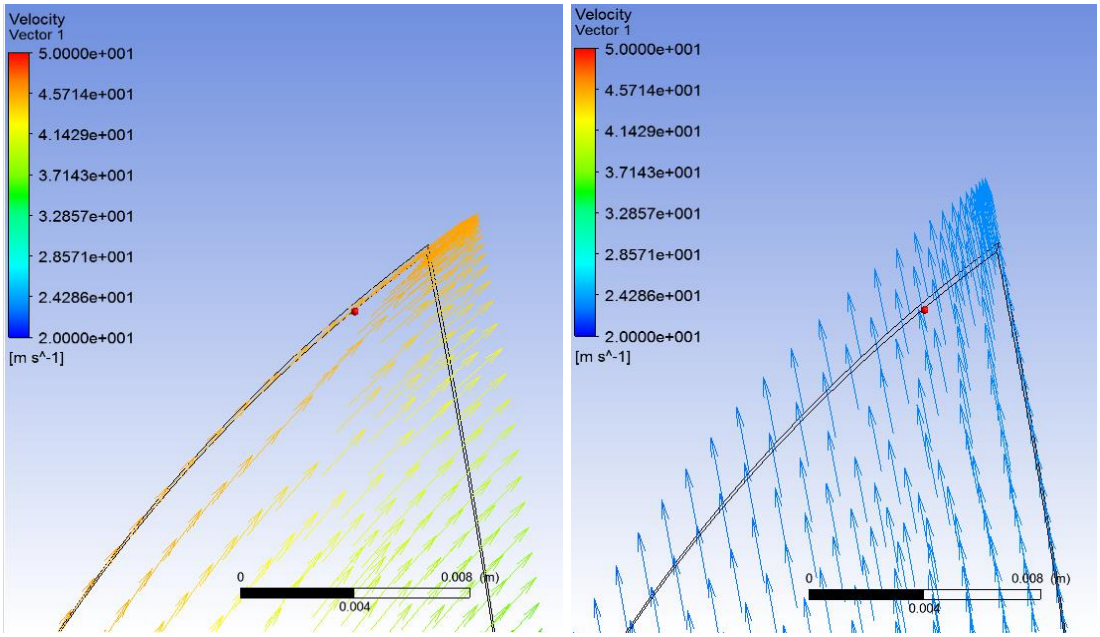

Figure 36. View of upper region of TC showing velocity profiles: TC (left) and BW (right).

Figure 37 shows the magnitude of the velocity of the oil in the vertical direction in the interior nodes of the LA (left) and on the face of the TC (right) for the $\omega_{TC} = 7{,}500$ rpm test case. The vertical or *x*-axis is in the direction from the inlet (bottom) to the outlet (top) of the LA. While the surfaces of the TC have a high velocity at the entrance in the vertical direction, the mid-plane of the LA cross-section area has a relatively low velocity. Figure 37 shows a flow reversal at the entrance region, so the oil is actually moving from the minimum film thickness that has a high pressure back down towards the inlet region that has a higher film thickness and lower pressure. The large difference in velocity across the film (from the surface of each disk to the velocity of the fluid in the middle of the LA) leads to a region of strong recirculation and flow turbulence, also shown in the figure. The recirculation region can only be properly captured through a three-dimensional analysis.

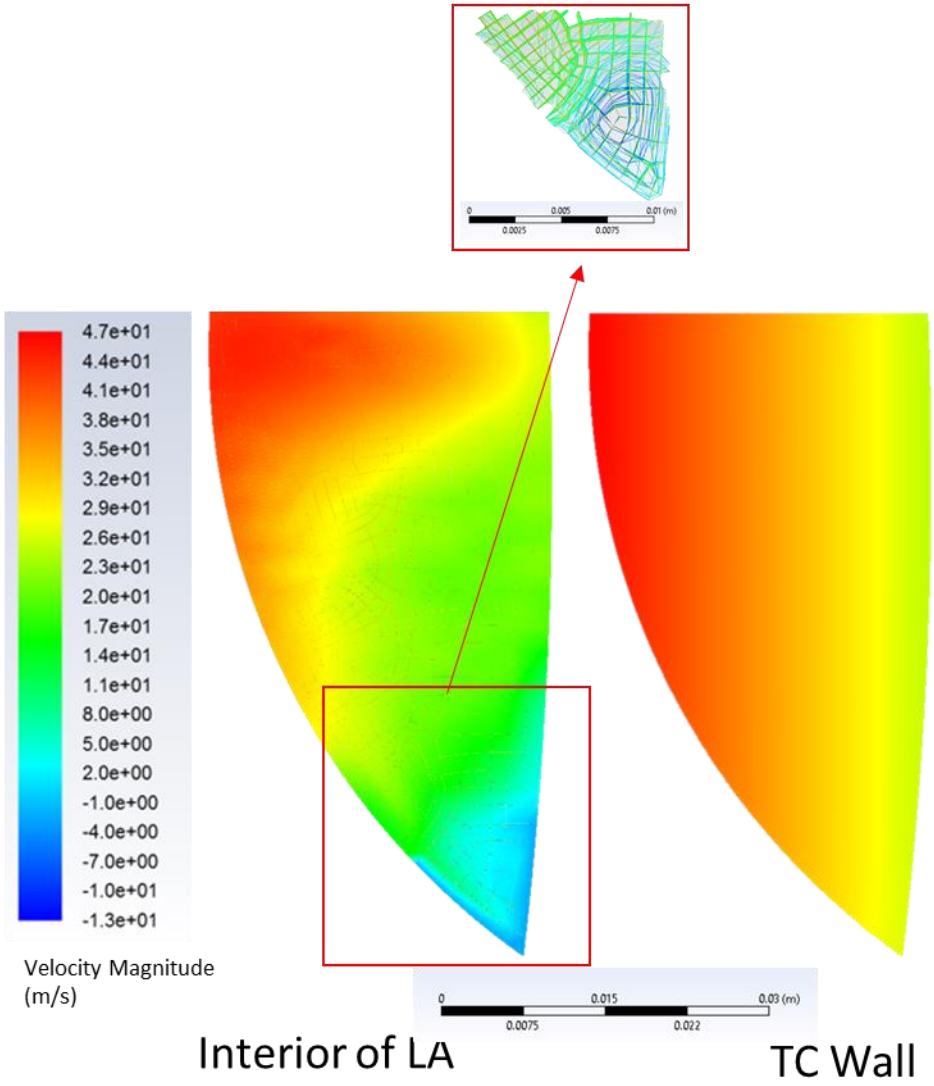

Figure 37. Contour plot showing the vertical velocity of the oil on the interior of the LA in m/s.

The model predicts a pressure field on both the TC and BW faces. The load is balanced by the pressure that arises because of the converging-diverging section of the LA. As the film thickness decreases the pressure profile increases, and vice-versa. The applied load is solved iteratively by setting the film thickness and calculating the pressure field. The boundary conditions are described

later in this section. The oil is two phase with cavitation as the interaction, so that bubbles form below the cavitation pressure (P_{cav}) and collapse above it.

FLUENT first uses the Rayleigh-Plesset equations to determine the lubricant cavitation area, and describes the bubble growth as

$$\frac{3}{2}\left(\frac{\mathrm{DR_b}}{\mathrm{Dt}}\right)^2=\left(\frac{\mathrm{P_B\text{-}P}}{\rho_l}\right) \tag{25}$$

where R_b is the radius of the bubble (5 micrometers), P_B is the bubble surface pressure, P is the field pressure, and ρ_l is the density of the liquid.

Once the bubble growth is described, a model must determine the mass transfer between the vapor bubbles and the surrounding fluid. ANSYS FLUENT supports three cavitation models: Singhal et al. model, Zwart-Gerber-Belamri model, and the Schnerr and Sauer model [49]. The Schnerr and Saur model is compatible with turbulent analysis, and describes the mass transfer term, R, as

$$\mathrm{R}=\frac{\rho_v\rho_l}{\rho}\alpha(1\text{-}\alpha)\frac{3}{\mathrm{R_b}}\sqrt{\frac{2}{3}\frac{(\mathrm{P_B\text{-}P})}{\rho_l}} \tag{26}$$

where α is the vapor volume fraction, and ρ_v is the vapor density.

Flow turbulence occurs in fluids when inertial forces become large compared to the viscous forces; it is characterized by a randomly fluctuating velocity field. FLUENT contains several turbulence models, this analysis uses the standard $k-\epsilon$ model [50], because it allows for multi-phase analysis and allows for modeling thin films due to the enhanced wall treatment. The standard $k-\epsilon$ model is also less computationally expensive and typically more stable than other models. The first step in the $k-\epsilon$ model is calculating the turbulent viscosity [50], obtained from

$$\frac{\partial}{\partial t}(\rho k)+\frac{\partial}{\partial x_j}(\rho k u_j)=\frac{\partial}{\partial x_j}\left[\left(\mu+\frac{\mu_t}{\sigma_k}\right)\frac{\partial k}{\partial x_j}\right]+G_k+G_b-\rho\epsilon-Y_M+S_k \quad (27)$$

G_k is the generation of turbulent kinetic energy due to velocity gradients, G_b is the turbulence from buoyancy, Y_M is the dilation in compressible turbulence, and S_k is a source term, where the coefficients for the source and sink terms can be found in [50]. Figure 38 shows the CFD y-plus values, where all of the values are below 5, and most are close to 1, as required for accurate predictions using using the k-ϵ model with enhanced wall treatment.

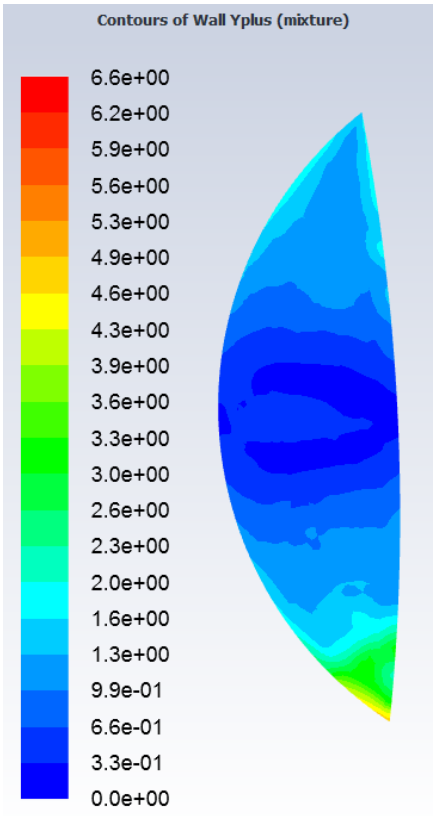

Figure 38. Y-plus values for CFD model showing most values close to 1 and all values below 5.

This CFD model uses three different sets of boundary conditions. Figure 39 shows the first and second set of boundary conditions along the edge of the TC. The first is a set in the lower portion of the TC imposing a velocity condition. This bottom section, extending up to 25 % of the LA perimeter, results from the projection of the inlet flow yet over the TC area. Numerical simulations varying the length of this region show little variation (<3%) in results from 10-35% variation along the TC perimeter. The inlet velocity on these faces is set to the prescribed test condition in the vertical direction given by the oil nozzle size and flow rate. The pressure along the upper portion of the TC perimeter is set to ambient condition. The third boundary condition is on the BW and TC face boundaries and these are set to rigid walls, or zero flow boundaries.

A three phase model tests for the possibility of air ingestion at either the inlet or the outlet of the TC. The three phases are oil (liquid), oil (vapor), and air. The boundary condition set a specific ratio of air to oil, so that at the inlet or outlet there was a percentage of the boundary that contained air. The inlet boundary condition was set with air to oil ratios of 5, 10, and 20%, while the outlet was included ratios of 30, 50, and 70%. The LA rejected all of the air at the inlet, so that the results were unchanged. For tests modeling air at the outlet, a small air bubble forms on the edge of the TC disk in the upper part of the LA. The air bubble grows for increasing air oil ratios. These results do not match what was found in experiments (no air ingestion present at these locations), so that the following analysis and results shows only the two-phase model (oil liquid and oil vapor).

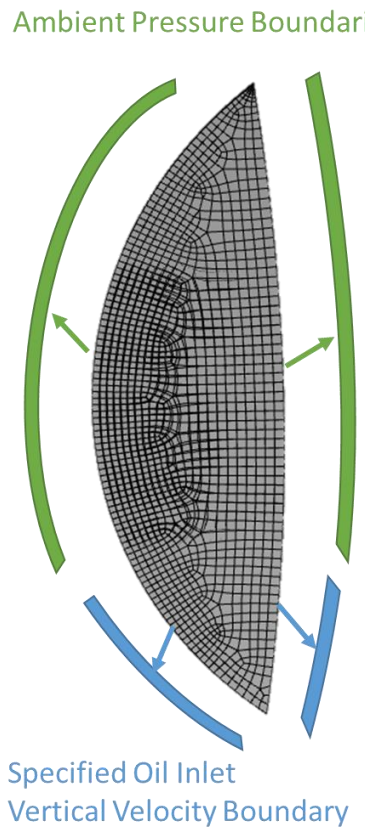

Figure 39. CFD boundary condition descriptions showing ambient oil outlet pressure boundary and specific vertical inlet velocity boundary.

Convergence is met when the residuals of velocity and continuity stabilize at values below 10e-4. The CFD model for most test cases converges after 20-30 iterations, but is run at 100 iterations to ensure convergence. The run-time for a single film thickness test point is typically ten to fifteen minutes. The computer has 96 Gb of RAM, a 64 bit / 3 GHz processor with 12 cores, and uses parallel processing. A mesh independence study, and results that are consistent with experiments and the FE model (in terms of pressure field, film thickness, and lubricant cavitation and flow turbulence location) validate the model assumptions.

5. RESULTS

The results section is broken into three parts: the experimental results, which provide a qualitative description of the lubricant cavitation and the flow turbulence; the numerical results section, which discusses the finite element (FE) and computational fluid dynamics (CFD) model predictions for pressure, cavitation, deflection, and turbulence; and finally a quantitative comparison of the predictions and experimental results.

Experimental Results

Figure 40 shows an averaged binary image at $\omega_{TC} = 7.5$ krpm and $F_{TC} = 1$ kN (11.6 bar). The binary image shows two disruptions in the flow field, one in the upper half of the thrust collar (TC) in the diverging section, and the other in the entrance of the lubricated area (LA). This section includes a qualitative description of the two flow disturbances, the first being cavitation and the second flow turbulence. Cavitation creates an area of mixed oil liquid and vapor. Since oil vapor is more transparent than the surrounding liquid, the light will shine through this area and reflect off the bull wheel (BW) more clearly. The high speed camera (HSC) receives more light from the cavitation area and it appears brighter. Turbulence in the entrance region causes small eddies to form in the flow. These eddies reflect more light directly back to the camera than the surrounding laminar region. Turbulent flow is difficult to distinguish from laminar flow without tracing particles, but the HSC can still observe differences in recorded light from the eddies. Small differences in recorded brightness are exaggerated through the gamma filtering, as described in the experimental procedure section. Otsu's method takes the local differences in brightness to create a binary image. In Figure 40, the white areas that extend up the TC are eddies that have not dissipated.

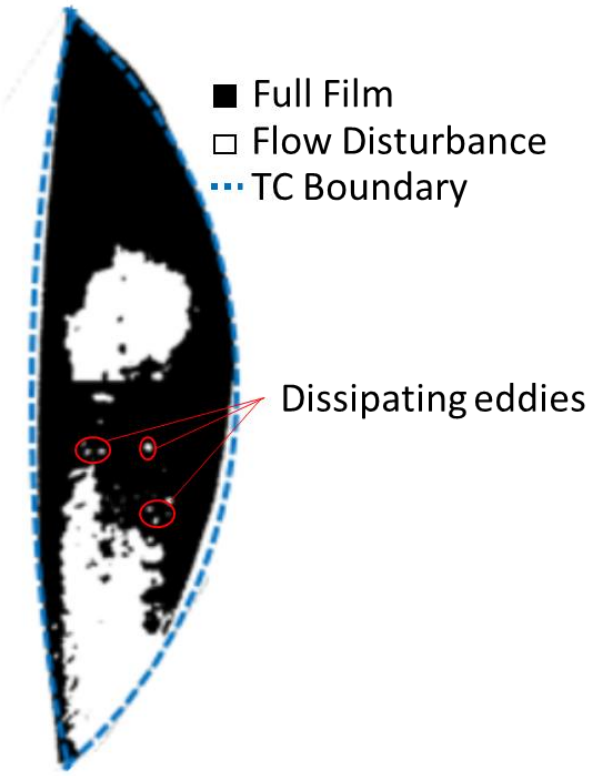

Figure 40. Averaged binary image for $\omega_{TC} = 7.5$ krpm, ω_{BW} = 624 rpm, and $F_{TC} = 1$ kN, highlighting the two regions of interest, lubricant cavitation in the diverging section and flow turbulence in the inlet region.

Lubricant Cavitation Measurements

This section contains a description of the lubricant cavitation location, shape, transience, and the effect of spin speed on cavitation.

Figure 33 shows the filtered LA images for $\omega_{TC} = 2.5$, 5, and 7.5 krpm, all at an F_z =1 kN. The cavitation streamers, highlighted by red circles, appear as an area that is brighter than the surrounding liquid. Similar to the optical cavitation study conducted by Song et al. [17], the cavitation area becomes more clear as the spin speed increases, and it is only easily identifiable at

speeds over 5 krpm. Otsu's method and other thresholding techniques cannot distinguish between the lubricant cavitation area and the rest of the film for a majority of the images.

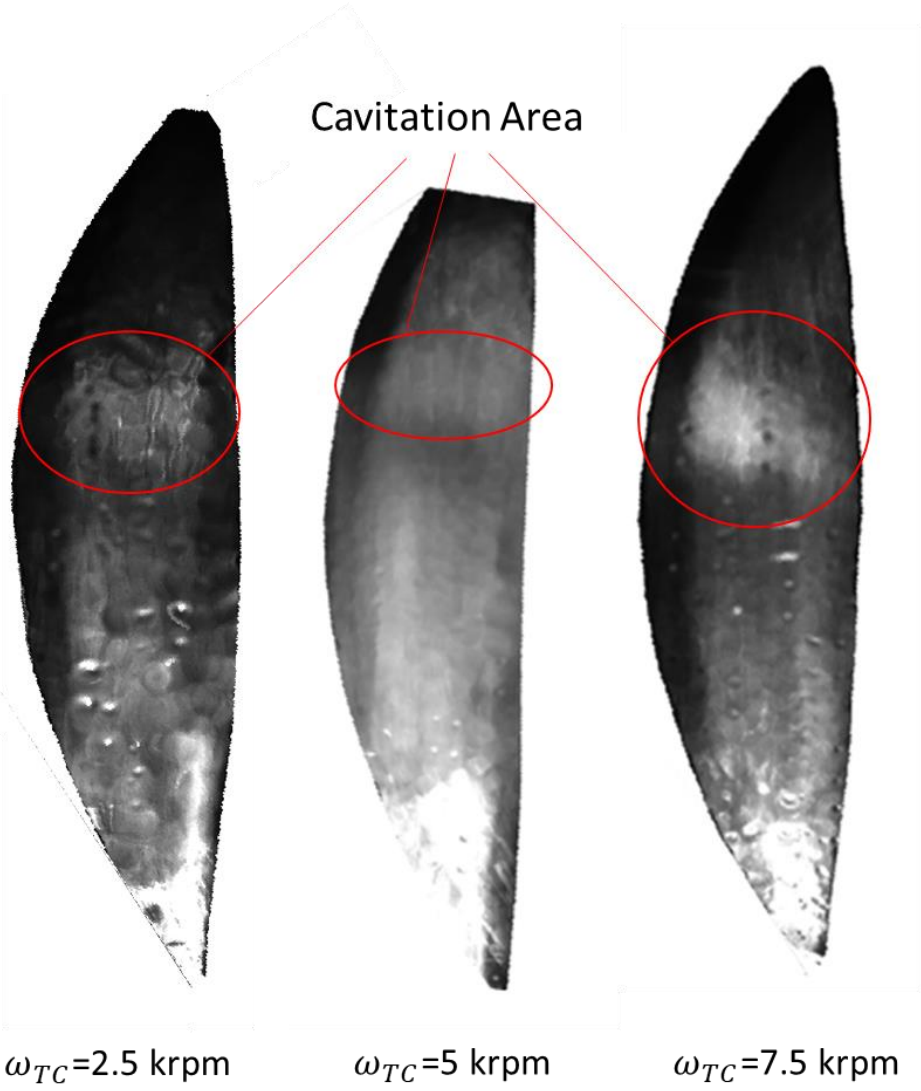

Figure 41. LA for three spin speeds highlighting the cavitation area.

Figure 42 shows the cavitation from the same video for four time steps for the $\omega_{TC} = 7.5$ krpm test case. The top pictures have a gamma filter applied to them, and the bottom images show the

binary results. The streamers occasionally reach up and extend past the previous reformation boundary, but in general the shape of the cavitation area remains consistent. The figure also includes the averaged result for the four time steps. The cavitation formation boundary is a nearly horizontal line that begins slightly above the half-way point of the LA. There is very little cavitation at the edges of the LA, where the pressure is close to ambient. The reformation boundary features a semi-circular shape above the formation line, and extends approximately 15 mm from beginning to end. The cavitation area makes up 14.5% (290 mm^2) of the total lubricated area. The results also show a turbulent area at the entrance region of the LA.

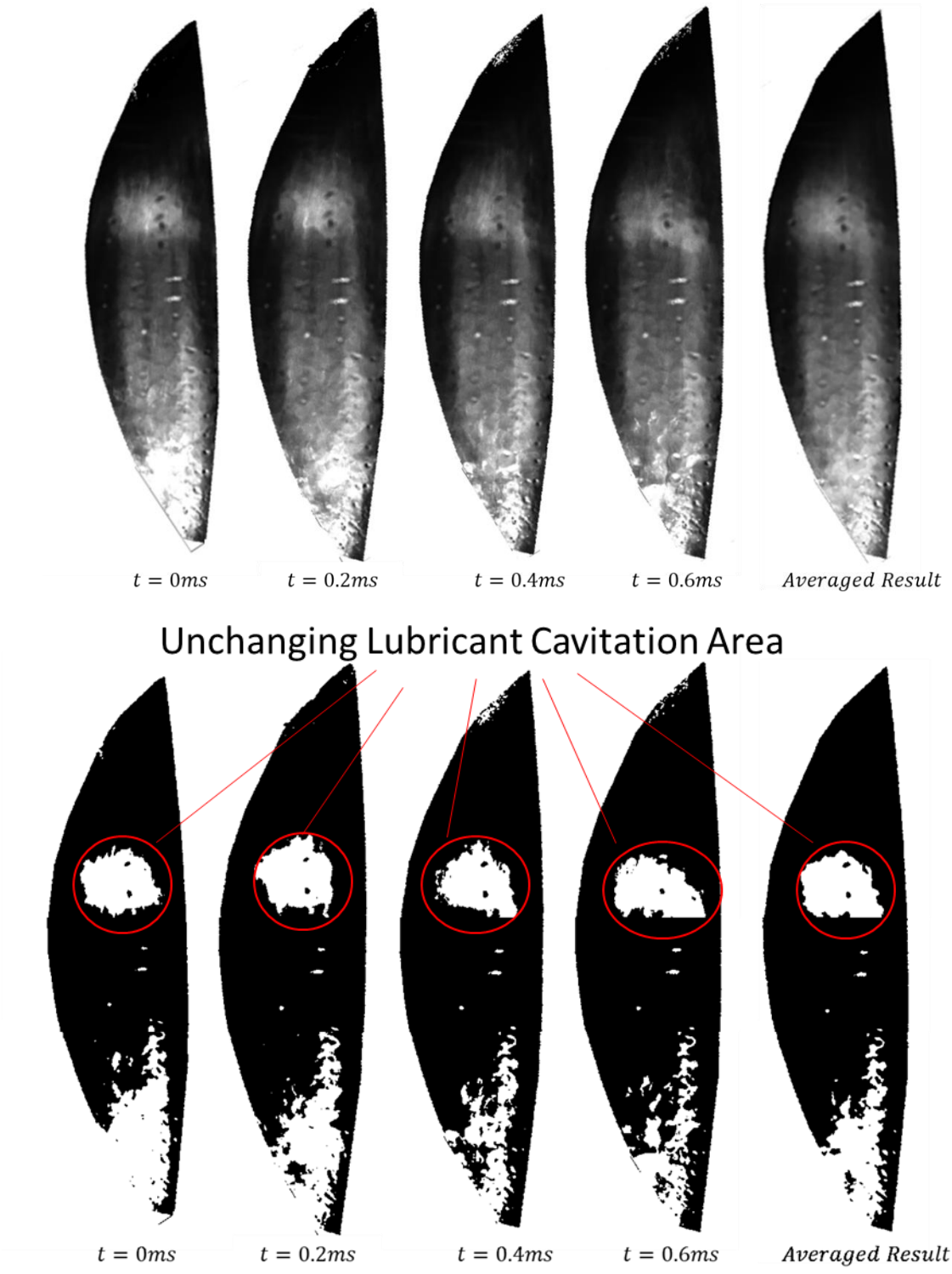

Figure 42. LA for four steps in time highlighting the unchanging nature of the lubricant cavitation area for $\omega_{TC} = 7.5$ krpm, ω_{BW} = 624 rpm, and $F_{TC} = 1$ kN (11.6 bar unit load).

Flow turbulence Measurements

This section investigates the observed flow disturbance at the inlet (shown for example in Figure 29). The section walks through possible causes behind this disturbance, and concludes that, as also described in Section 4, this region is associated to flow turbulence rather than flow starvation or lubricant cavitation. The section also describes the location, shape, and transience of the flow turbulence; and the effect of increasing oil inlet velocity on the flow turbulence area.

There are three possibilities for describing what is occurring in the entrance region of the TC LA: air ingestion, flow turbulence, or cavitation. This section shows confirmed examples of air ingestion, cavitation, and flow turbulence, and compare them to the results in Figure 29 to identify it as primarily flow turbulence.

Figure 43 shows an example of air ingestion occurring in the LA, when $\omega_{TC} = 0$ rpm, $\omega_{BW} =$ = 60 rpm, and F_{TC} = 0 N. The image was captured with a standard camera, at a framerate of 24 fps. The image was taken in RGB color. The LA shows two clear air-oil boundaries. The air is not mixing with the oil at all, and the boundary moves throughout the LA in a laminar, steady manner. The air-oil boundary in the figure appears similar to air ingestion seen in squeeze film dampers [16]. The steady, un-mixing air-oil boundary is different to the transient area in Figure 29.

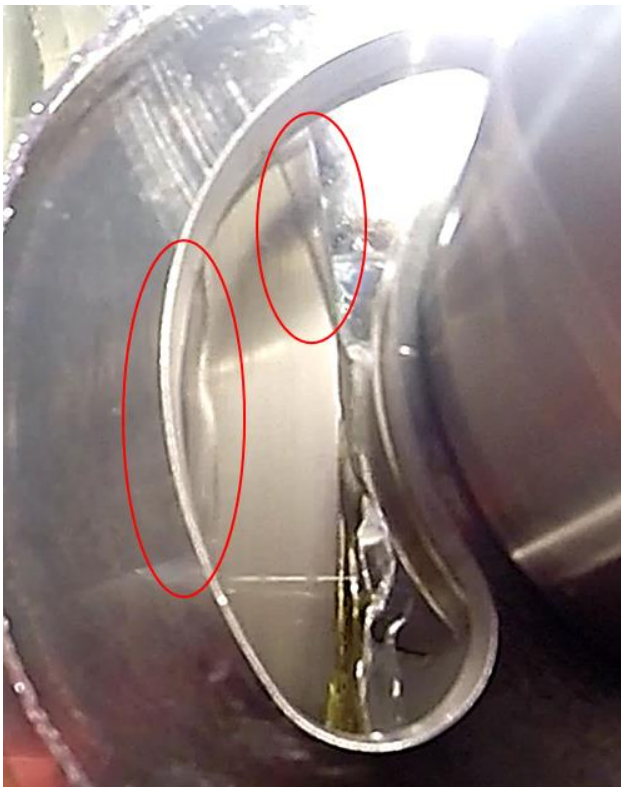

Figure 43. TC LA for $\omega_{TC} = 0$ rpm, ω_{BW} = 60 rpm, and F_{TC} = 0 N, showing air ingestion.

Figure 44 shows an example of air ingestion that does occur in the inlet region during testing, but that is distinct from the turbulent region. There are eight images of the LA for ω_{TC}=2,500 rpm, ω_{BW} = 214 rpm and F_{TC} = 1,000 N during a time span of 1.6 milliseconds. The eight images all display the bright colored disturbance in the entrance region that is characterized by flow turbulence, but also shown in the video is an air bubble that forms at the BW boundary (lower left side) and travels across the lower area until it exits at the TC boundary (right side). The air bubble is highlighted in the figure by the red circle. Some part of this lower inlet region does include air ingestion, although it is minimal, and easily identifiable, because the bubbles do not conform to a central area and quickly exit the LA.

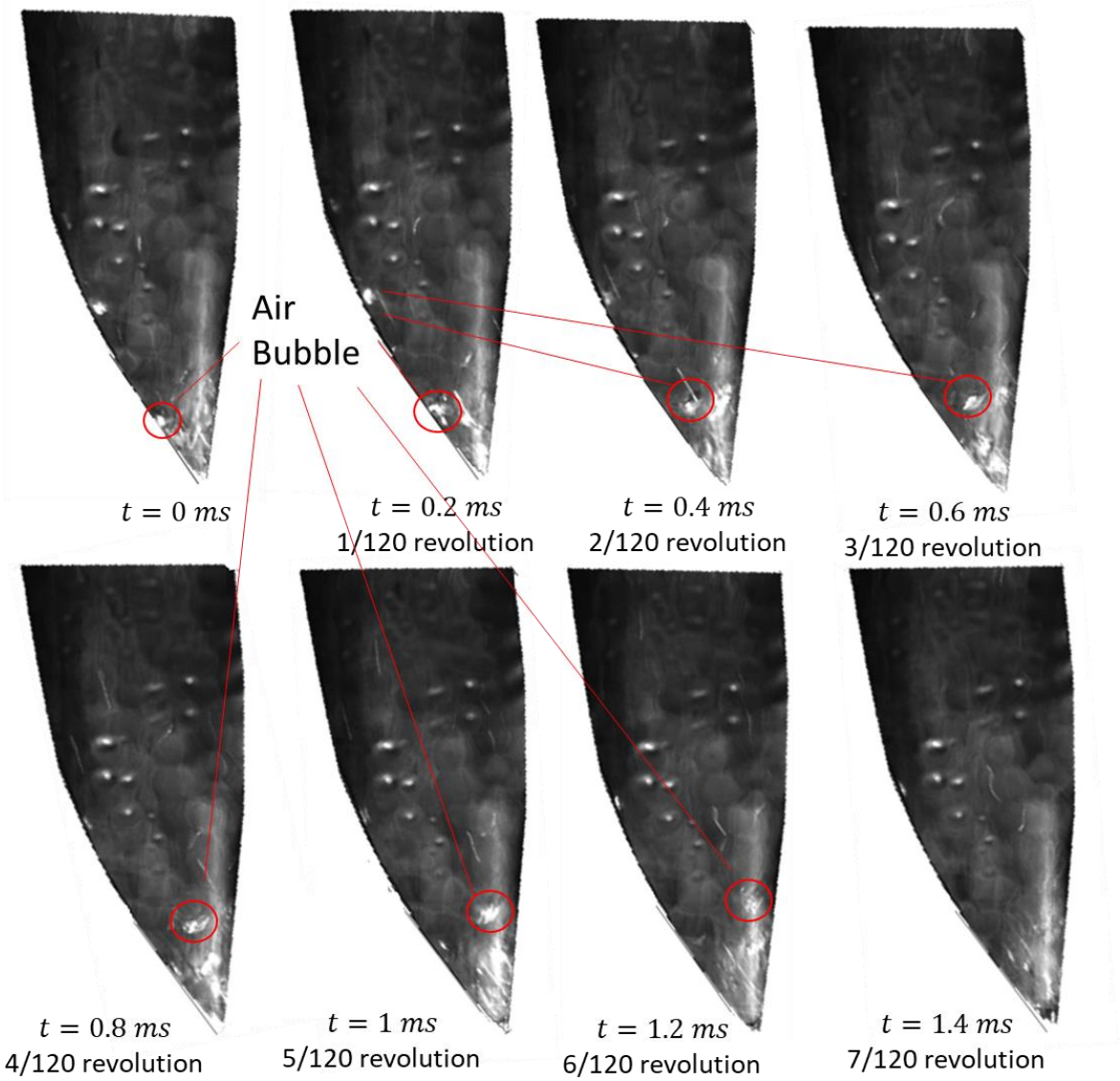

Figure 44. Air bubble entering LA on the TC boundary and exiting at the BW showing the difference between an air bubble and the flow turbulence area for ω_{TC}=2,500 rpm, ω_{BW} = 624 rpm, and F_{TC} = 1,000 N.

Figure 45 shows a LA with cavitation occurring in the diverging section of the TC in the form of vapor streaks. The images are from the $\omega_{TC} = 0$ rpm, ω_{BW} = 60 rpm, and F_{BW} = 1,000 N test case. The camera could not capture the entire LA in one shot, so two images are shown at different times for the upper and lower region. The upper region shows cavitation streaks that grow and

shrink, in a non-uniform way, but remain in the same area. The entrance region shows no cavitation, or disturbances in the flow at all. The non-transient area and noted streaks do not conform to what is seen in Figure 29. Additionally, if lubricant cavitation forms in entrance region (instead of turbulence) for test conditions with a spinning TC, it would also appear in Figure 45 for the stationary TC.

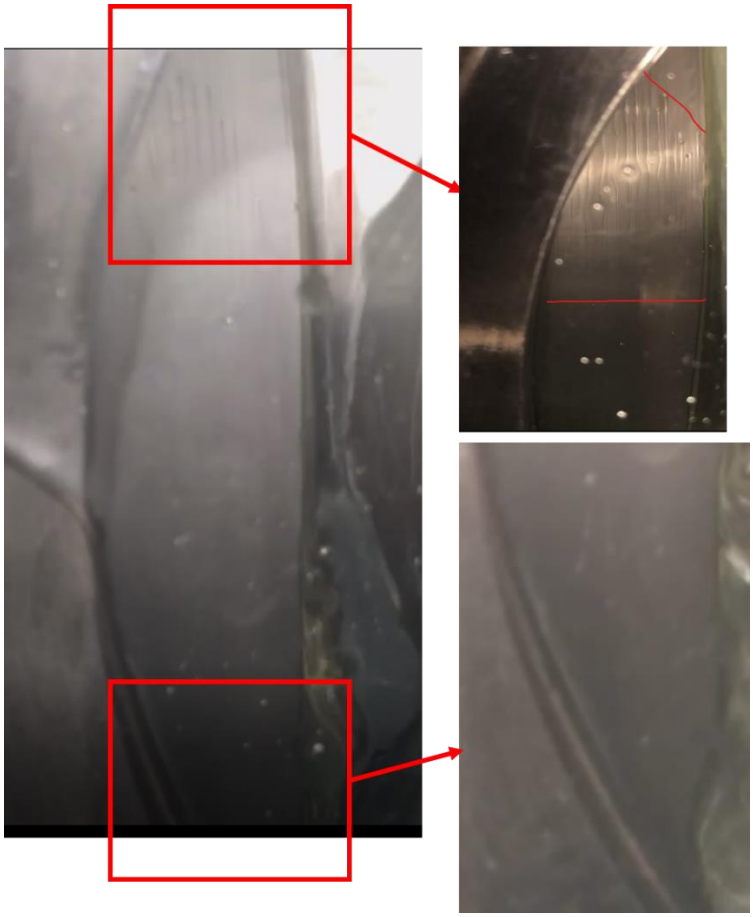

Figure 45. TC LA for $\omega_{TC} = 0$ rpm, ω_{BW} = 60 rpm, and F_{TC} = 1,000 N showing oil cavitation in diverging section which does not match flow turbulence seen in other figures.

Turbulence is characterized by areas of randomly-fluctuating velocity. Figure 46 shows the LA for $\omega_{TC} = 2{,}500$ rpm, ω_{BW} = 214 rpm, and F_{TC} = 0 N. The images are all taken from the same video at 5 different instances in time. The framerate of the video is 5,000 fps, so that $\Delta t = 0.2$ milliseconds. The top of the images were not illuminated as strongly as the bottom part of the LA, and therefore appear darker. The pictures clearly show flow turbulence occurring throughout the LA, and the images are very similar to those of the entrance region from Figure 29 with respect to reflectivity and the movement of the fluid (best seen in the videos shown in Appendix B). When F_{TC} = 0 N, the HSS is free to move axially, and the film thickness will be large because there is no axial force to react the pressure field. The effects of the converging-diverging wedge are minimal, because of the large film thickness, so that there is not a large pressure drop in the LA. When the TC is loaded, the film thickness begins to decrease, and the turbulence only remains in the area with a large gap. The results section shows that increasing axial load decreases the flow turbulence area.

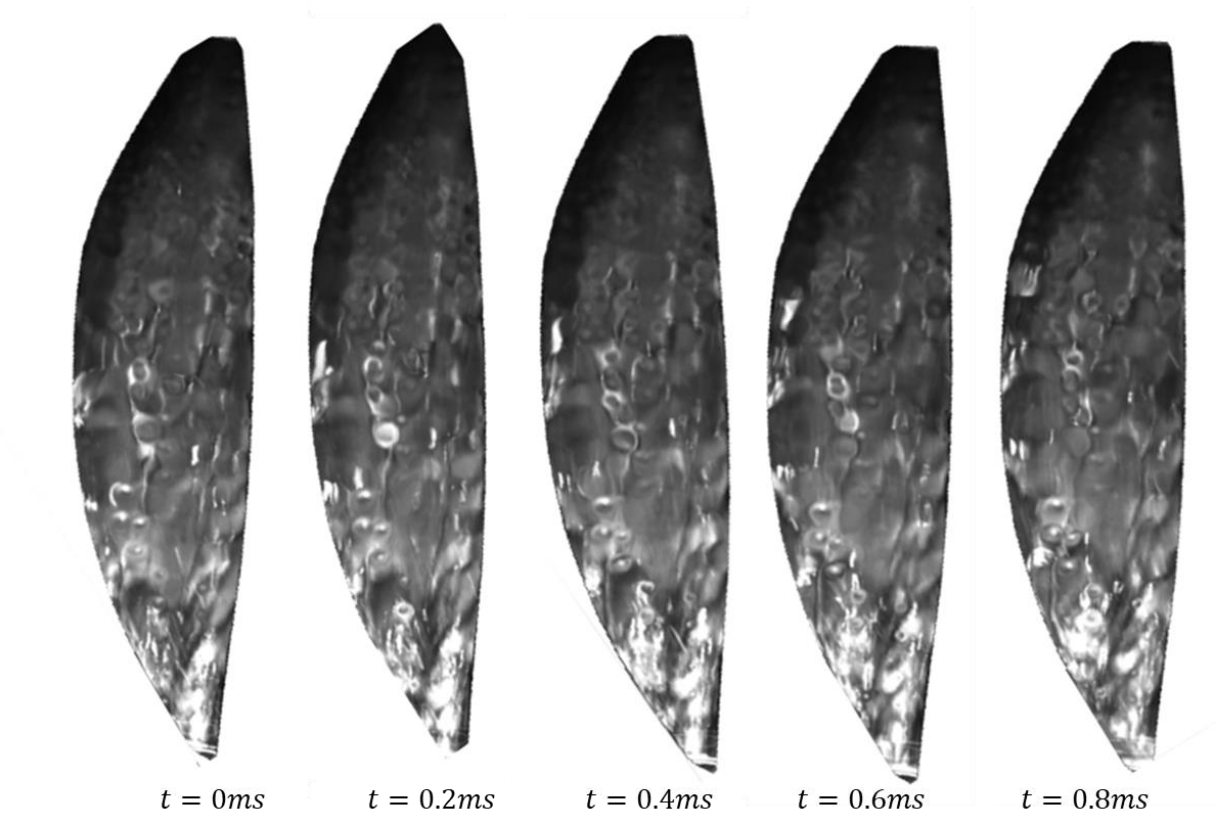

Figure 46. Five shots of the TC LA for five instances in time with $\omega_{TC} = 2.5$ krpm, ω_{BW} = 214 rpm and F_{TC} = 0 N, showing clear flow turbulence matching results seen in entrance region of other test conditions.

Figure 43, Figure 45, and Figure 46show air ingestion, lubricant cavitation, and flow turbulence, respectively. Comparing the inlet region of Figure 29 with these figures suggests that the disturbance in this region is turbulence. As indicated previously, while there may be some air ingestion, as bubbles do form and exit at low speeds, the air ingestion is minimal, and there is no cavitation in this section, so that the disturbance in the inlet region seen in Figure 29 is attributed to flow turbulence. Turbulence occurs at the inlet because of a large film thickness, high surface speed, and velocity direction differences across the film thickness causing high flow vorticity. The

maximum local Reynolds number for the ω_{TC}=7,500 rpm is only 930. These results were obtained from videos that can be viewed in Appendix B.

Figure 47 shows an unfiltered TC LA for three different pinion speeds, all at $F_{TC} = 1$ kN. At each ω_{TC} there is an area of flow turbulence in the inlet region, indicated by the red lines. This turbulence area (A_{Turb}) grows with increasing ω_{TC} until close to $\omega_{TC} = 7$ krpm, where the area remains constant. The results for $\omega_{TC} = 5$ krpm appears brighter because the lights were positioned more directly on this part of the mirror. When calculating A_{Turb} ,the differences in brightness are accounted for by filtering and using Otsu's method. This is seen in the image of an area that has changing light intensity, so there is a mixture of lighter streaks in a field surrounded by darker fluid. Each video can appear different because of lighting differences, but the flow turbulence is always shown as a brighter area. The flow turbulence quickly transitions into a laminar regime as the film clearance decreases and the pressure increases. The upper boundary of the flow turbulent area grows and shrinks up the LA flow domain as a function of time, but always remains at the inlet region of the LA.

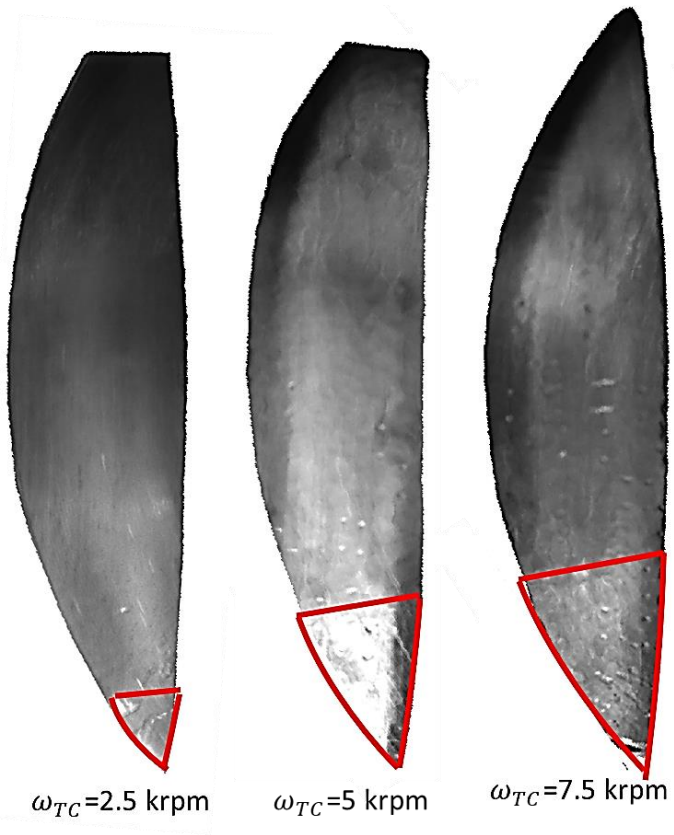

Figure 47. TC LA for three pinion shaft speeds, all at an axial load of 1 kN, showing the flow turbulence area within the red triangle that grows for increasing spin speed.

Figure 48 shows the TC LA for different oil inlet speeds, where all the images were obtained at $\omega_{TC} = 2.5$ krpm and $F_{TC} = 1$ kN. The top images are unfiltered, and the bottom images show the binary results. At a TC spin speed of 2,500 rpm, the surface speed at the perimeter of the TC is 15.7 m/s. A_{Turb} tends to grow for increasing inlet velocity, until the oil velocity becomes larger than the surface speed of the TC. At that threshold (15.7 m/s), the flow turbulence area shrinks and then disappears, as shown in the picture for $V_{oil} = 23\,\frac{m}{s}$, where the highest local Reynold's number is below 330.

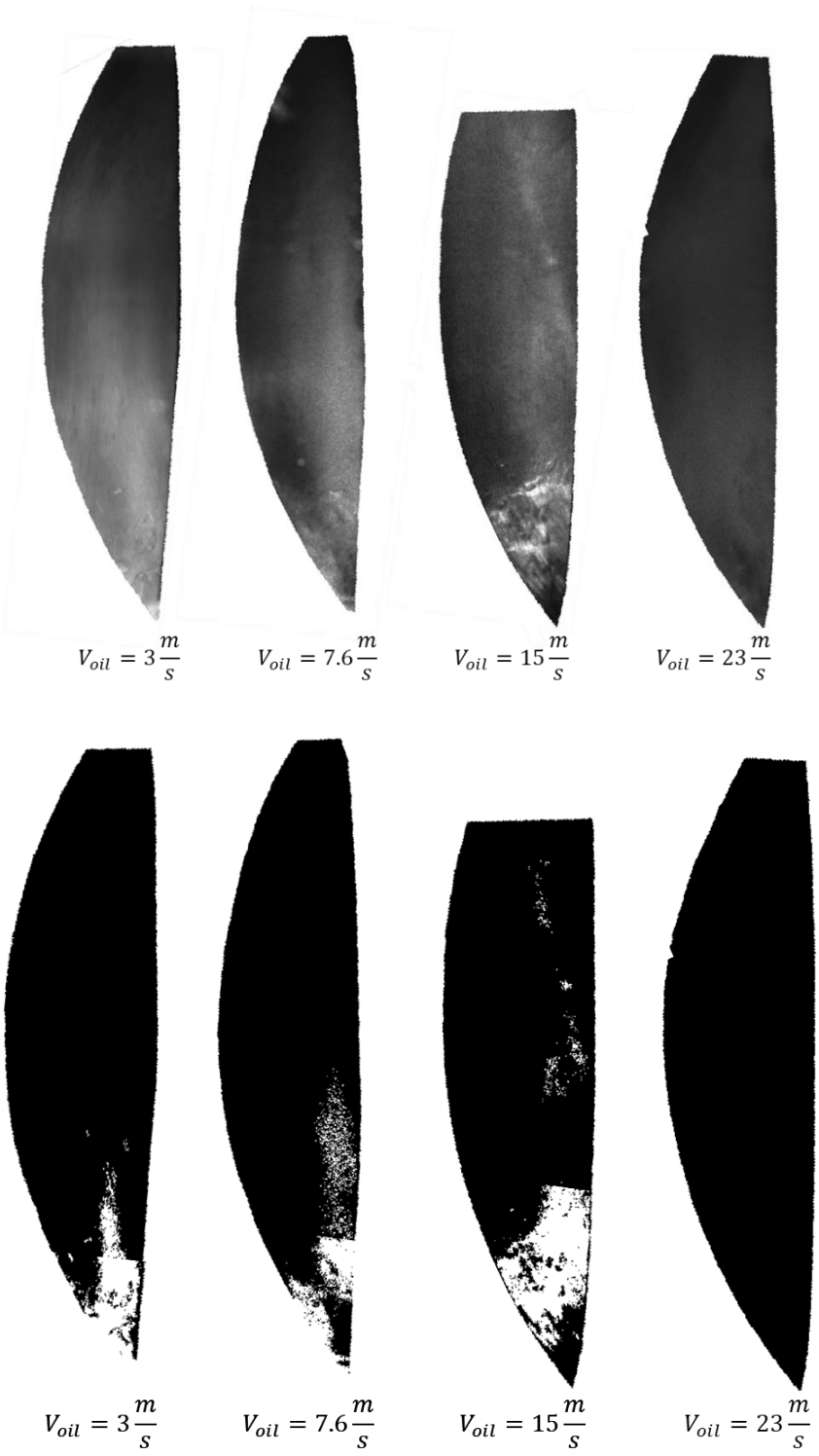

Figure 48. TC LA at $\omega_{TC} = 2.5$ krpm, ω_{BW} = 214 rpm, and $F_{TC} = 1$ kN for a range of oil inlet speeds, where the white area is the flow turbulence, showing the increase of turbulence area with increasing oil inlet velocity, until the surface speed of the disk is met.

Numerical Results

FE Model Results

Figure 49 shows the two-dimensional pressure profile from the FE model for $\omega_{TC} = 7{,}500$ rpm, and $F = 1{,}500$ N. The maximum pressure occurs in the lower half of the LA, near the centerline. This test case only requires two iterations for the switch matrix, and four iterations for the film thickness. The resulting pressure field is very similar to the previous FE model [12] that uses the Reynolds assumption to model the cavitation. The Elrod's method predicts a slightly lower load capacity, typically one to two percent, when compared to the model that uses the Reynolds assumption to model the lubricant cavitation. The reason is that the high pressure area remains largely unchanged for different lubricant cavitation models, and this region is responsible for transmitting the axial load.

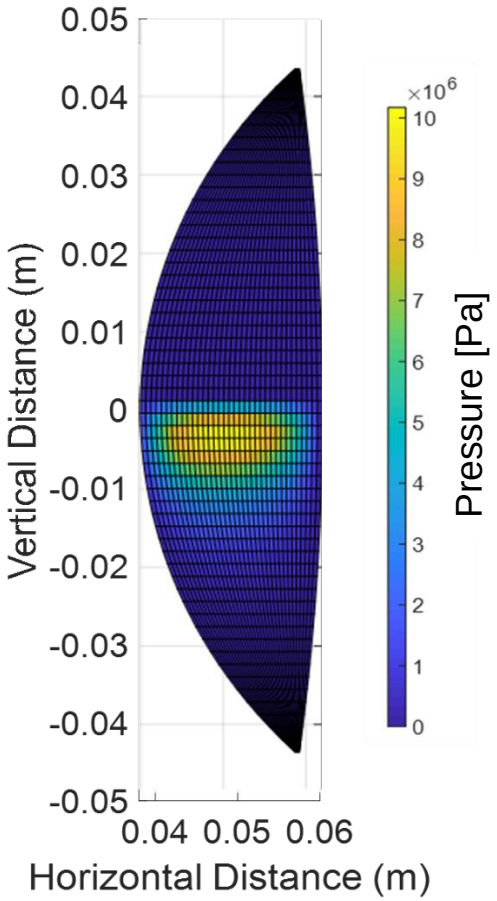

Figure 49. Numerical prediction of thrust collar 2-D pressure profile using FE model for $\omega_{TC} = 7,500$ rpm, ω_{BW} = 624 rpm, and $F = 1,500$ N (11.6 bar).

Figure 50 shows the final switch matrix over the LA. Areas where the switch function are equal to 1 signify full film lubrication, while 0 relates to cavitation. The upper half of the LA is cavitated for this test case. There is a reformation boundary at very top of the LA. Using Elrod's method, the switch function is either 0 or 1. In actuality, there will be some mixture of vapor and liquid around the boundary.

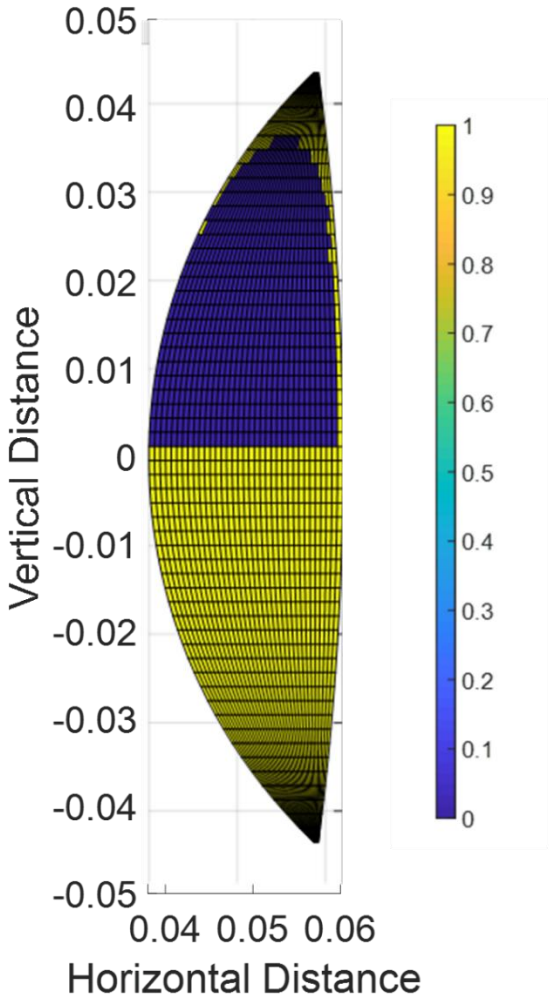

Figure 50. Switch matrix over the LA where 1 corresponds to full film lubrication and 0 is cavitation for $\omega_{TC} = 7,500$ rpm, ω_{BW} = 624 rpm, and $F_{TC} = 1,500$ N.

Solving the elastic deformation equations requires an additional loop after the original film thickness is calculated. Figure 51 shows the initial $h(x, y)$, $\delta(x, y)$, and percent difference between the two for the $\omega_{TC} = 7{,}500$ rpm, and $F_{TC} = 1{,}500$ N test case. The film thickness, left, is smallest at the centerline and is largest near the top and bottom. The largest deflection, shown in the middle, occurs in areas with the largest local pressure. The minimum film thickness for this test case is

equal to 0.0317 mm and occurs near the centerline of the LA. The maximum deflection is 0.0309 mm, and occurs at the same location as the minimum film thickness. Thus, the deflection nearly doubles the film thickness at this location, but has little effect elsewhere in the LA. Including deflection add significant computational costs to the model. To decrease the amount of time to run the code, the number of elements is decreased in both the horizontal and vertical direction. The smaller amount of elements also makes the results easier to see. The fidelity of the model is also not affected by using this coarser mesh.

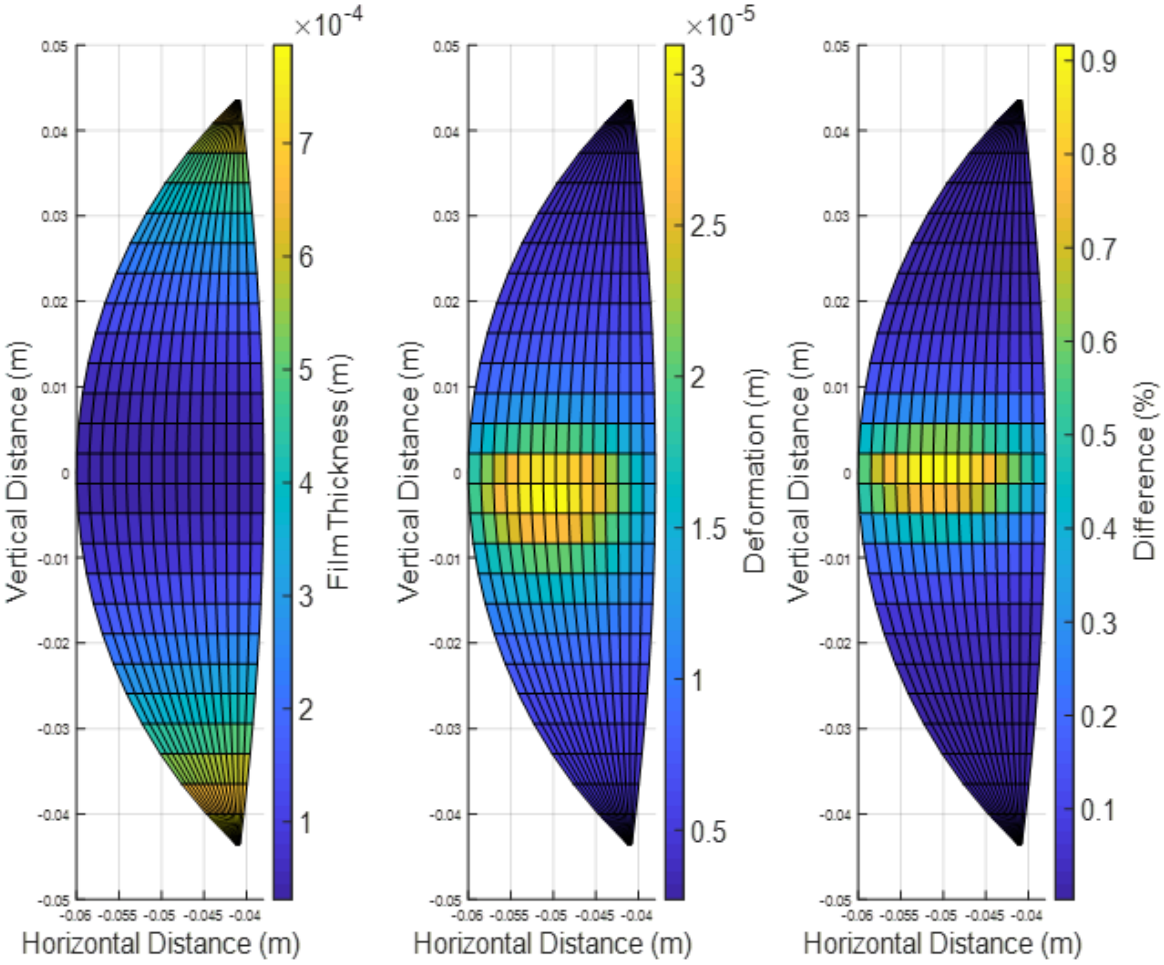

Figure 51. Initial film thickness (left) and deflection (middle) of the LA from the FE model, and percent difference (right) between the initial film thickness and the deflection (note different scales) for the $\omega_{TC} = 7,500$ rpm, ω_{BW} = 624 rpm, and $F_{TC} = 1,500$ N test case.

Once the deformation results are added into the film thickness, the loop repeats solving for the new pressure profile. Figure 52 displays the pressure field of the LA for the first and second iteration of the elastic deformation loop. After the second iteration, the pressure profile is distributed over a larger area. The pressure profile now extends further up the LA. The peak pressure is also reduced from 9 MPa to 3.5 MPa. The cycle is repeated until the film thickness and deformation converge. This test case converges quickly, after only three iterations. Finer meshes with 1,000 elements produce similar results at a higher computational cost. At lower loads (<600 N), the deformation barely changes the film thickness, and the model converges after only one loop. Summation of the pressure across the LA yields the axial force through the TC. The code uses a built in MATLAB iterative function to solve between the prescribed axial force and the initial film thickness.

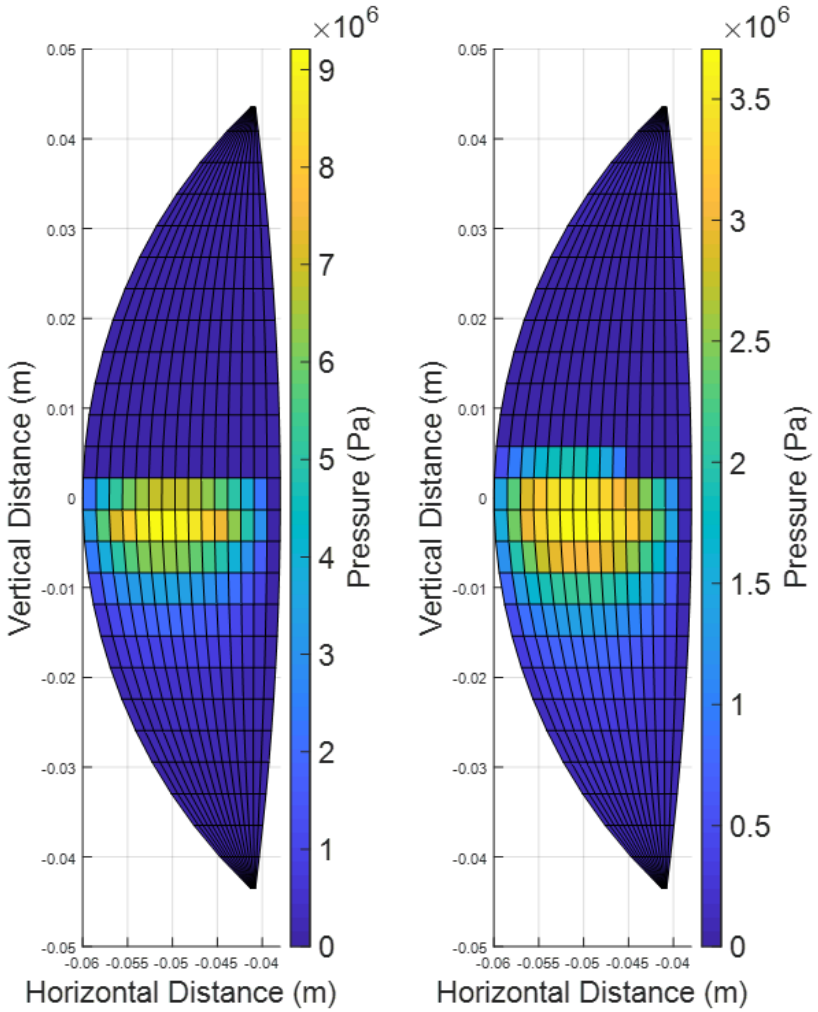

Figure 52. Predicted pressure field of the LA after first (left) and second (right) iteration for elastic deformation (note different scales) for the $\omega_{TC} = 7,500$ rpm test case.

Figure 53 presents the cavitation field for a rigid surfaces case and the case that includes elastic deformation of the surfaces. Since the deflection pushes the diverging section of the film thickness up, the pressure field is more distributed across the film, and reaches higher along the LA. The lubricant cavitation area is therefore smaller, because the film rupture boundary occurs later in the development of the flow, while the reformation boundary is in the same location.

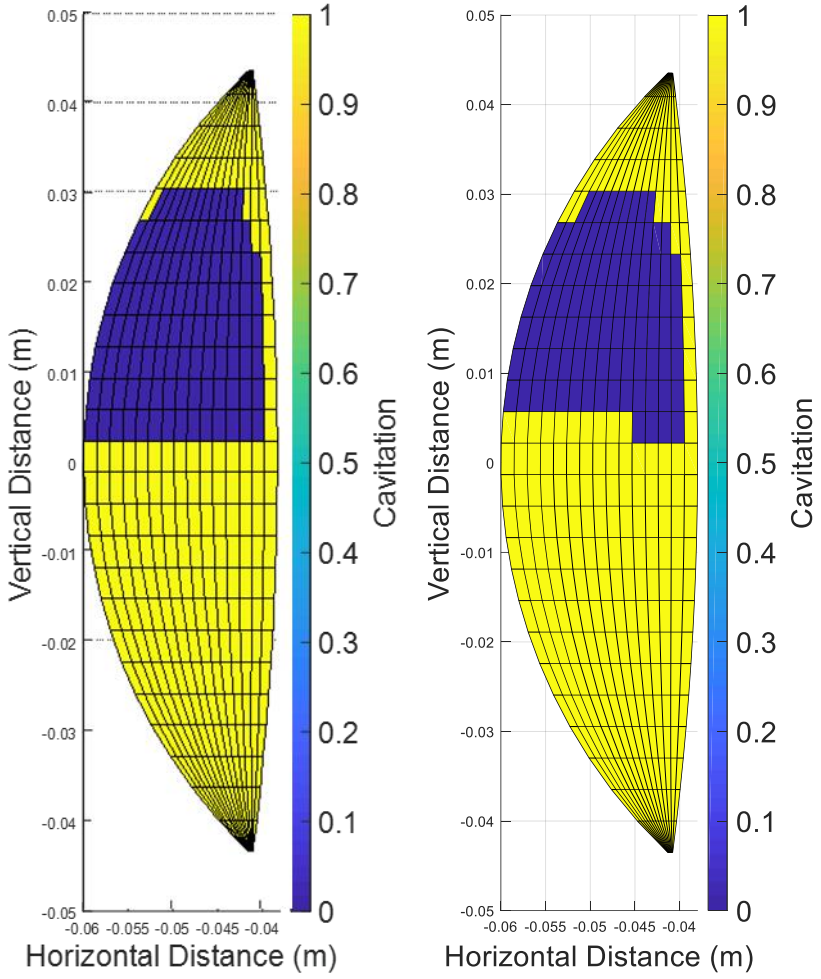

Figure 53. Cavitation area in the LA assuming rigid surfaces (left) and elastic surfaces (right) for the $\omega_{TC} = 7,500$ rpm, ω_{BW} = 624 rpm, and $F_{TC} = 1,500$ N test case.

Including cavitation and elastic deformation both tend to decrease the predicted load capacity of the TC for a given minimum film thickness. Figure 54 shows the minimum film thickness against predicted axial load for the $\omega_{TC} = 7.5$ krpm test case for three different models. The first model is the original Reynolds solution [12], the second model uses Elrod's method to describe the lubricant cavitation, and the third includes Elrod's method and the effects from deformation.

The deformation assumes one disk (TC) is made of acrlyic, and the other disk (BW) is made of steel. Using a mass conserving model for lubricant cavitation has little effect on load capacity and only tends to decrease the predicted axial force by a couple Newtons. Including deformation decreases the predicted load capacity especially at higher loads. This is due to edge thinning, where at the center line (the horizontal line of minimum film thickness) the clearance is larger in the middle of the LA than at the edges. For the minimum film thickness shown (24.8 micrometers) , the predicted load capacity is 25% lower than that predicted by the models excluding deformation.

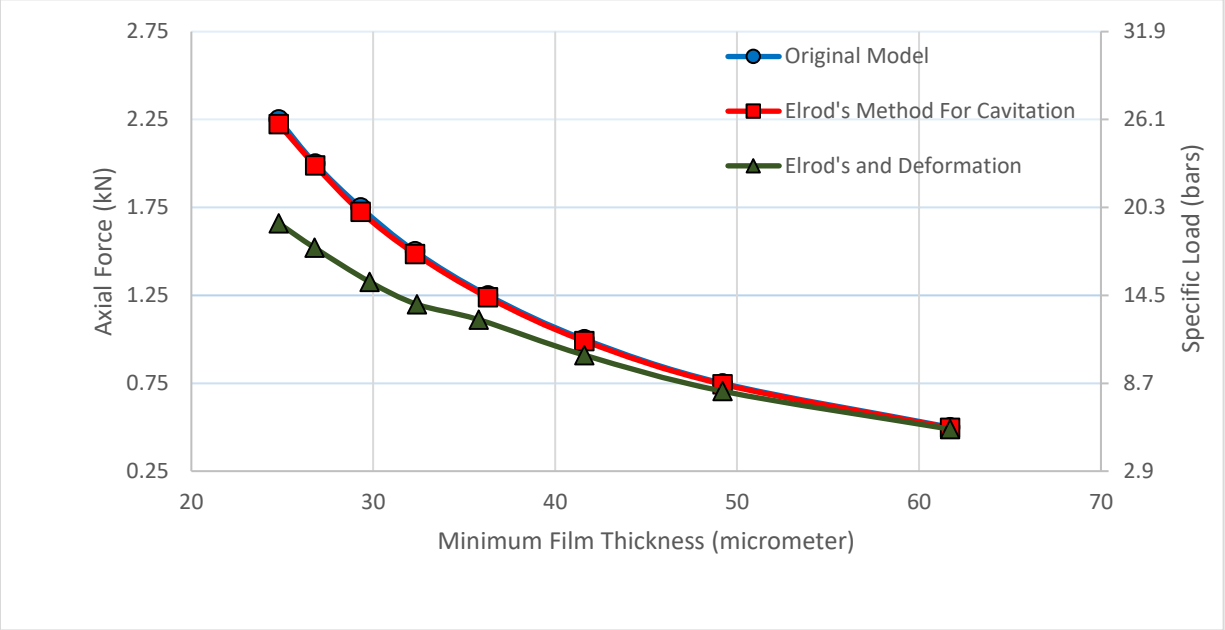

Figure 54. Minimum film thickness versus axial force for three models (original Reynolds, including cavitation, and deformation) using acrylic as TC surface for the $\omega_{TC} = 7.5$ krpm and ω_{BW} = 624 rpm test case.

Using acrylic results in a much lower effective bulk modulus, 7 GPa compared to 200 GPa when both disks are made of steel. At these low test loads, if both disks were made of steel the deflection would be very minimal and have no effect on the results. Even using acrylic, at these lower loads, the effect of elastic deformation on load capacity is minimal. But at higher loads (>1.5 kN for acrlic and >5 kN or 58 bar specific load for steel) the effect from elastic deformation could be substantial even for disks made of steel. There is a wide range of possible axial loads in industrial IGCs. TCs in IGCs can see very low axial loads when there is a compressor stage on each end of the pinion shaft and they are well balanced, the TCs can even be completely unloaded. TCs can also see loads up to at least 15 kN (170 bar) when the pinion shaft is not balanced [51].

Figure 55 shows the film thickness with (right) and without (left) deformation for an axial load of 10 kN. The effective bulk modulus is 202 GPa (two steel disks) to demonstrate the need for including elastic deformation when high loads are present. The minimum film thickness (7.9 micrometers) for the model without elastic deformation occurs at the midline of the LA. The minimum film thickness for the model that includes deformation is 7.03 micrometers and it occurs at the edge of the LA midplane, called edge thinning. Including elastic deformation becomes important at high loads when edge thinning starts to occur, because rubbing can happen at the edge of each disk when a rigid model would predict full film. For steel disks with the current speeds and TC geometries, modeling that includes elastic deformation becomes necessary above loads of 5 kN (55 bar unit load), when the predicted load capacity can be over 15% lower when compared to that predicted without considering deformation. Kerr [13] measured an averaged relative axial displacement of the TC LA for varying axial loads. His results are for a steel TC and only tested to a maximum axial load of 3 kN, but his results matched what was found in the rigid model.

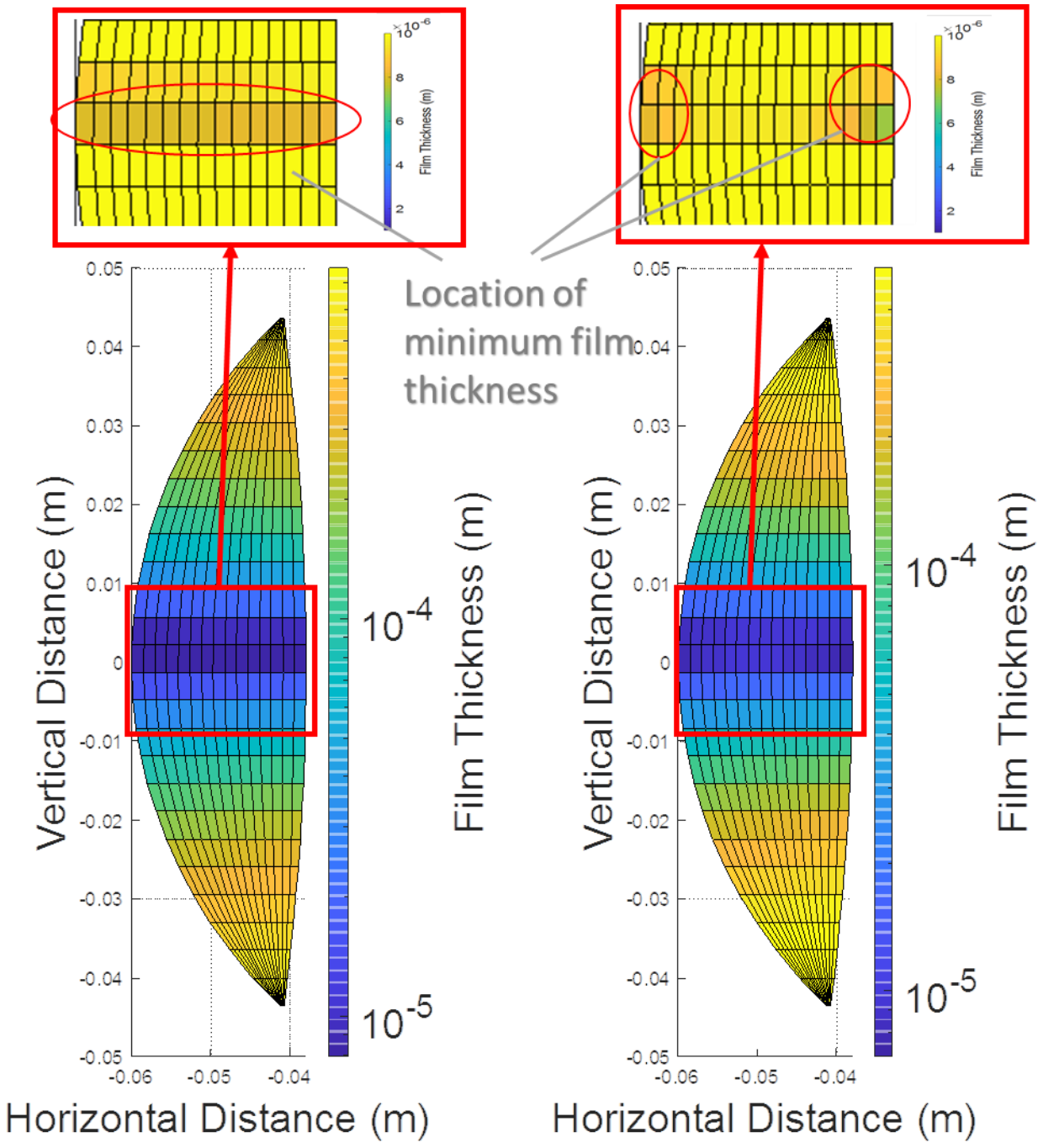

Figure 55. Predicted film thickness from rigid (left) and elastic (right) model for two steel disks highlighting location of minimum film thickness for a test condition of $\omega_{TC} = 7,500$ rpm, ω_{BW} = 624 rpm, and $F_{TC} = 10$ kN (155 bar unit load) test case.

Because the elastic deformation at the given test load range (500-1500 N) has a small impact on the pressure field (even with an acrlyic disk), the CFD model does not include elasticicty of the disks. A more detailed analysis on the effect of elastic deformation on load capacity can be found in [6].

CFD Model Results

Figure 56 shows the absolute pressure in Pa on the face of the TC from the CFD model. Integrating the pressure field over one surface yields the resultant force. For this film thickness, the resultant force is equal to 1,500 N.

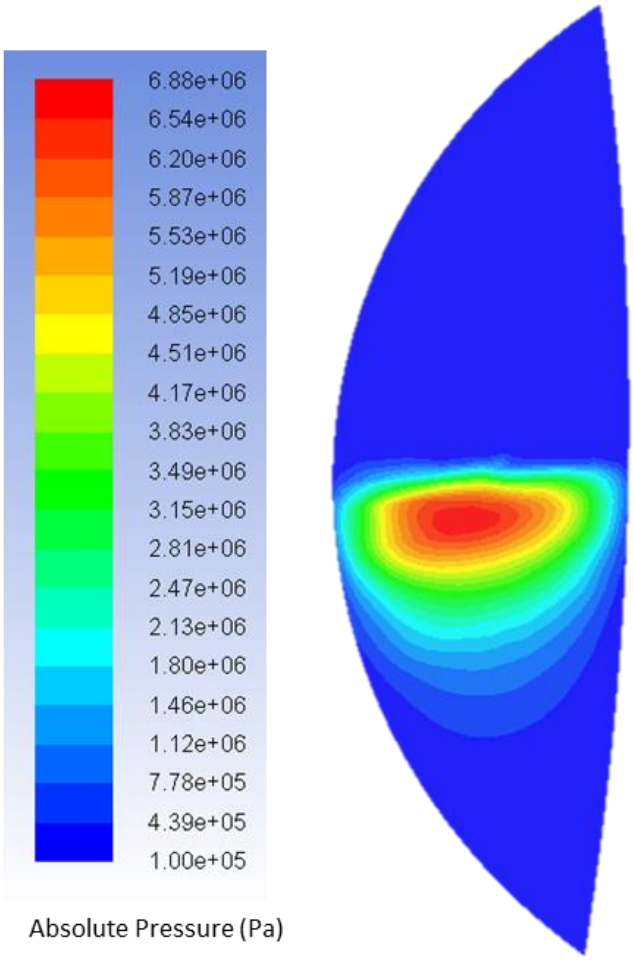

Figure 56. Absolute pressure profile of TC LA on the TC face in Pa for the $\omega_{TC} = 7,500$ rpm, ω_{BW} = 624 rpm, and $F_{TC} = 1,000$ N test case.

Figure 57 shows the oil volume fraction, where 1 corresponds to all oil, and 0 to all vapor in the interior of the LA. The cavitation occurs in the upper part of the LA, in the diverging section. There is no cavitation at the very top of the LA, where the vapor has reformed into liquid. CFD does predict an area with both oil vapor and oil liquid in the cavitation region. The volume fraction

in the cavitated area is 94% liquid by volume, but this has been weighted by mass. The cavitation pressure for the CFD and FE model is set to 1,000 Pa [52].

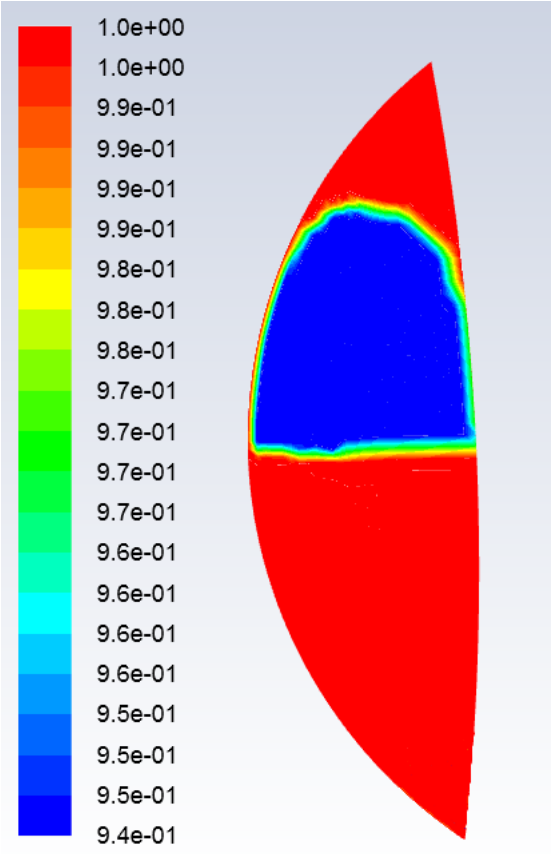

Figure 57. Oil volume fraction in the interior of the LA at the mid-plane for the $\omega_{TC} = 7,500$ rpm, ω_{BW} = 624 rpm, and $F_{TC} = 1,500$ N test case.

Figure 58 shows the dimensionless turbulence intensity values for $\omega_{TC} = 2.5$ krpm and $F_{TC} = 1{,}000$ N. The turbulence intensity is defined as the ratio of the root-mean-square (RMS) of the velocity fluctuations to the mean flow velocity. The mean flow velocity is set to 1 m/s, to show just the RMS of the fluctuations. Turbulence intensity shows where turbulence is occurring in a flow field, and also provides a good estimate of the magnitude of the velocity fluctuations in that

area. There is a mixture of turbulence that occurs in the entrance region of the TC. The area of highest turbulence intensity is closest to the bottom region, while there is no turbulence in the rest of the TC LA. Including turbulence in the model does not have a significant impact on load capacity, since the turbulence occurs far from the high pressure area that determines the resultant force. The lubricant cavitation and flow turbulence results from the CFD model will be discussed in the next section.

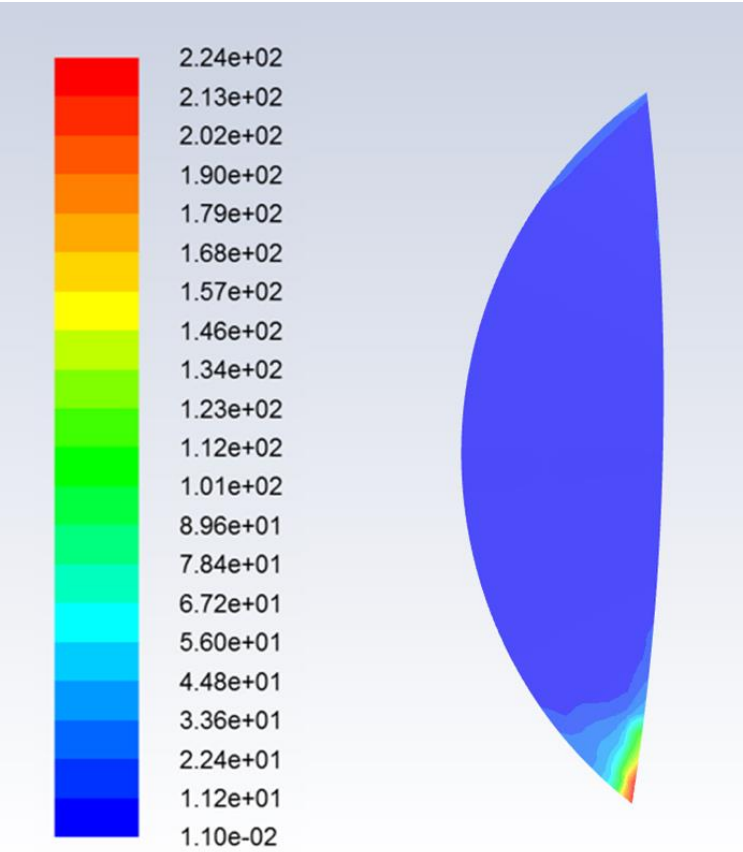

Figure 58. Turbulence intensity (dimensionless) from FLUENT CFD model for the $\omega_{TC} = 2,500$ rpm, ω_{BW} = 214 rpm, and $F_{TC} = 1,000$ N test case where the local Reynolds number in this area is below 330.

Figure 59 shows the CFD predicted pressure field on the face of the TC for the $\omega_{TC} = 7.5$ krpm and $F_{TC} = 1{,}000$ N test case. The left image includes flow turbulence and the right image is from a laminar model. There is no noticeable difference in the pressure profiles. The resultant axial force on the disk is 13.2 N higher for the turbulent model. The turbulent model has a higher profile because the eddies slightly increase the pressure in the area resulting in an extra axial force on the disks. The reason flow turbulence has a very small effect on the load capacity is because the turbulent area is in a low pressure area. The area in the middle of the LA that contains the high pressure area largely determines the load capacity. The flow disturbances outside of this area then have a small effect on load capacity. Predicted power loss is higher when including flow turbulence, but the difference is only 13.1 Watts (under ~2% of the total 0.82 Watts) for the $\omega_{TC} = 7.5$ krpm and $F_{TC} = 1{,}500$ N test case.

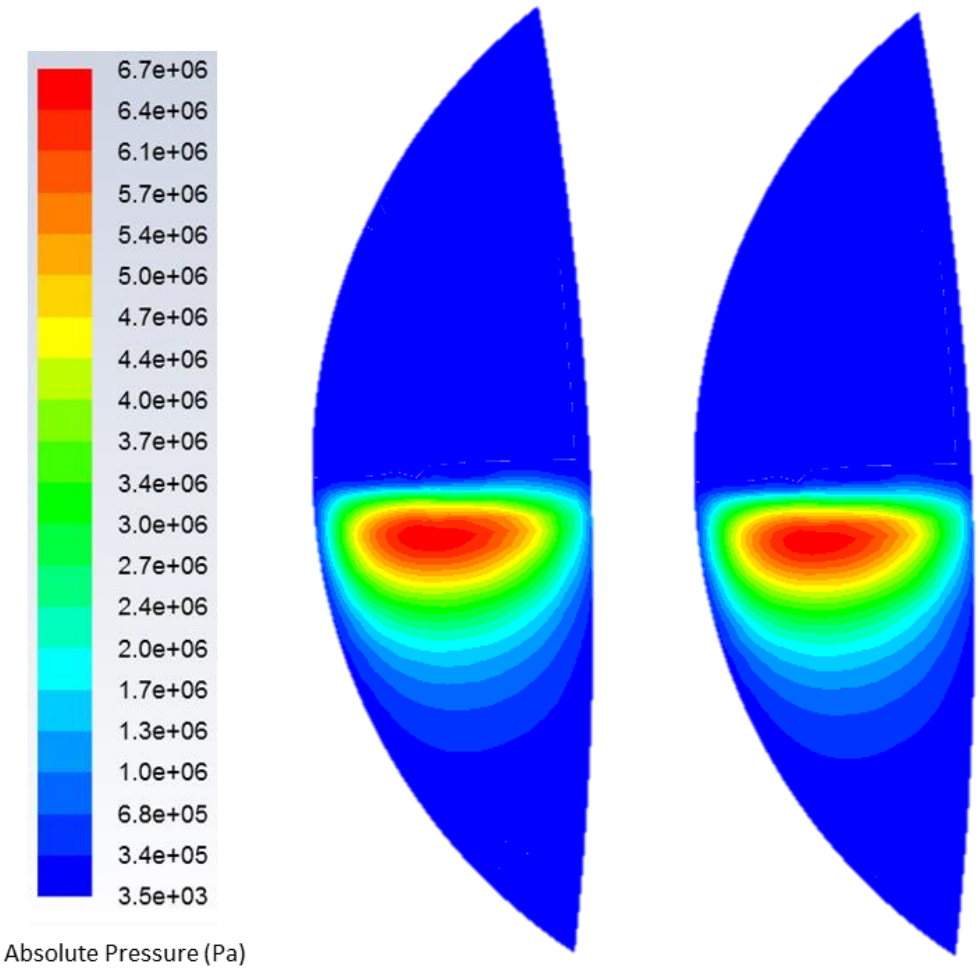

Figure 59. Predicted pressure profile for model with (left) and without (right) including flow turbulence for the $\omega_{TC} = 7,500$ rpm, ω_{BW} = 624 rpm, and $F_{TC} = 1,000$ N test case showing little difference to pressure field when including turbulence modeling (local Reynolds number is below 330).

Comparison of Results

Table 6 provides a description of the test matrix. The top table shows the results that were captured for the cavitation, and the bottom table shows the results including turbulence. The test cases where the CFD model outputs cavitation are marked in the corresponding cell with a red *C*, blue *F* corresponds to lubricant cavitation results from the FE model, and the experimental results

displaying cavitation are represented with a green *E*. The FE model does not predict turbulence area, since it cannot capture recirculation in a three-dimensional flow field. An axial natural frequency prevented testing at medium and high loads for the 7.5 krpm test case. Axial vibrations at these loads forced a shut-down, so that there are no flow turbulence or lubricant cavitation results at these test points. Cavitation was not observed at the lower spin speeds and is not presented for the experiments either. Due to the pump/ nozzle combination the maximum oil inlet velocity that could be achieved was 30.4 m/s. Because the maximum oil speed is below the surface speed of the disks at the 5 krpm test case, only the 2.5 krpm spin speeds were tested with different inlet velocities. The cavitation results are shown first, followed by the turbulence results.

Table 6. Test matrix showing available results from experiments, CFD model, and FE model.

Cavitation		Spin Speed		
		2.5 krpm	5 krpm	7.5 krpm
Axial Load (specific load)	500 N (7.8 bar)	C,F	C,F	C,F,E
	750 N (11.6 bar)	C,F	C,F	C,F
	1,000 N (15.5 bar)	C,F	C,F	C,F

Turbulence		Spin Speed		
		2.5 krpm	5 krpm	7.5 krpm
Axial Load (specific load)	500 N (7.8 bar)	C,E	C,E	C,E
	750 N (11.6 bar)	C,E	C,E,N	C
	1,000 N (15.5 bar)	C,E	C,E	C

C - CFD
F - FE
E – Experiment
N - Nozzle

Figure 60 compares the FE, CFD, and experimental cavitation area as a percent of the total LA for all speeds and loads in the test matrix. The experimental lubricant cavitation and flow turbulence area is calculated by dividing the total number of pixels in each area respectively, by the total number of pixels in the LA. The predicted area from both the CFD and FE models are calculated by taking the area of each element with turbulence or cavitation and dividing by the total area of all the elements. Cavitation is not clear enough at low speeds to record the results, so there is only one data point for the experimental results ($\omega_{TC} = 7.5$ krpm). The CFD model predicts a larger lubricant cavitation area than the FE model (approximately 10% more) because of disk flexibility. The CFD model does not include elastic deflection of the TC and BW surfaces. The experimental cavitation area is half of the FE predictions. The lubricant cavitation area for the CFD predictions is higher because the pressure profile area is larger than the pressure area of the FE model. These discrepancies may also be associated to the visualization method. Since the oil film is nearly transparent, it is expected that this method would also capture cavitation streaks in the interior of the film thickness (instead of on the TC acrylic surface). However, if there were a small amount of cavitation vapor compared to the surrounding liquid oil, the extent of the cavitation area would be difficult to visualize and quantify. Similar to the lower speed tests, the visualization method may not capture the entire cavitation region.

The lubricant cavitation area increases versus spin speed for both the CFD and FE models, so that the $\omega_{TC} = 7.5$ krpm test case is approximately 7% larger than the $\omega_{TC} = 2.5$ krpm test case. There is very little variance in cavitation area for different axial loads for the FE model, while the CFD model has changes in area of up to 5 % for different axial loads.

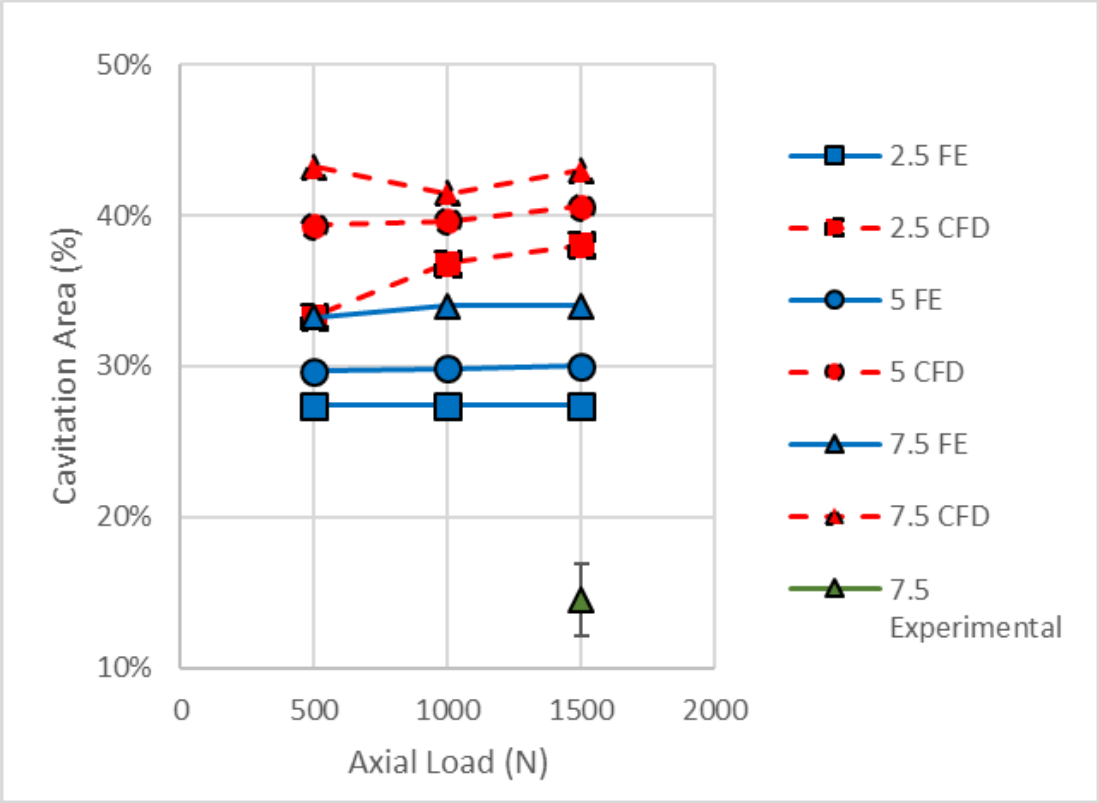

Figure 60. Predicted and experimental lubricant cavitation percent area versus axial load for three pinion speeds: CFD model shown by red dashed lines, FE model shown by solid blue lines, and experimental results shown by green line and the legend shows the TC spin speed in krpm.

Figure 61 shows a comparison of the CFD and experimental results for flow turbulence area at all the points in the test matrix. The CFD model predicts a larger turbulence area than the experimental results. One explanation is that the turbulent to laminar regime in the experiments is indistinguishable from the laminar section. Another explanation could be that the experimental area with very low turbulence intensity indicated by the CFD results do not provide a significant change in reflected light compared to the laminar region. The flow turbulence area decreases as axial load increases for the experimental results, but increases for the CFD model.

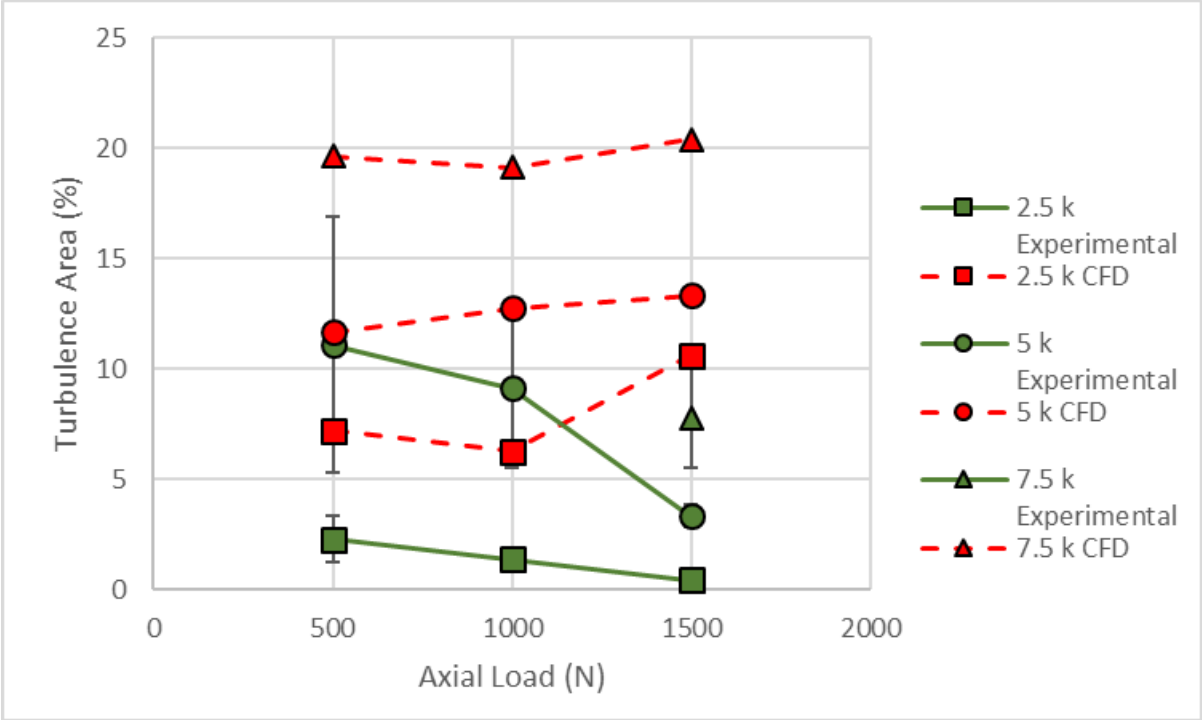

Figure 61. Turbulent area versus axial load for three pinion speeds: CFD model shown by red dashed lines, and experimental results shown by green line and the legend shows the TC spin speed.

Figure 62 show the turbulent area versus oil inlet spin speed to disk surface speed ratio. The results are from the $\boldsymbol{\omega_{TC} = 2.5}$ krpm and $\boldsymbol{F_{TC} = 1}$ kN test case. The experimental results show a low flow turbulence area for $\boldsymbol{V_{oil}}$ = 3 m/s, this could be because this test case uses the open tubing instead of a nozzle. There is a large drop in turbulence area after $\boldsymbol{V_{oil}}$ becomes larger than 15 m/s, where the surface speed of the TC is close to 16 m/s. To decrease flow turbulence at the inlet, the required inlet velocity must be above the surface speed of the disks. After the speed increases above 23 m/s, the turbulence area begins to increase again. The increasing oil inlet velocity has no effect on the cavitation area.

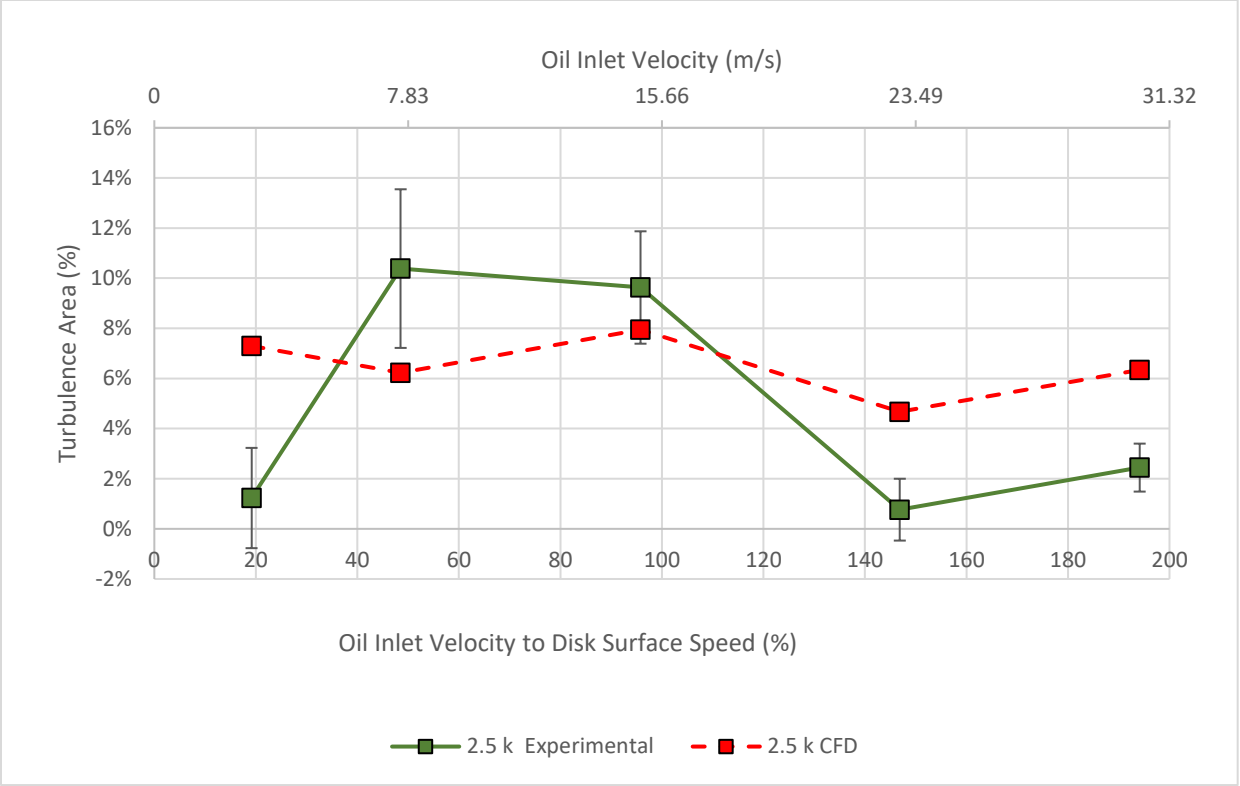

Figure 62. Turbulence area versus oil inlet speed: CFD model shown by the dashed red lines and experimental results shown for the solid green line at a test condition of ω_{TC} = 2.5 krpm, ω_{BW} = 214 rpm, and F_{TC} = 1 kN.

Figure 63 shows the pressure profile in the TC for ω_{TC} = 7,500 rpm, and F_{TC} = 1,500 N. The left image is the pressure profile from the CFD model, while the right image is from the FE model, both are in units of Pa. The FE image does not include disk deflection for this figure for the purpose of comparison. The maximum pressure occurs in the lower half of the LA, near the centerline. For this film thickness and pressure field, the resultant force is equal to 1,500 N. The pressure profiles are very similar to each other (within 10%), but the FE model predicts a larger maximum pressure at the center location.

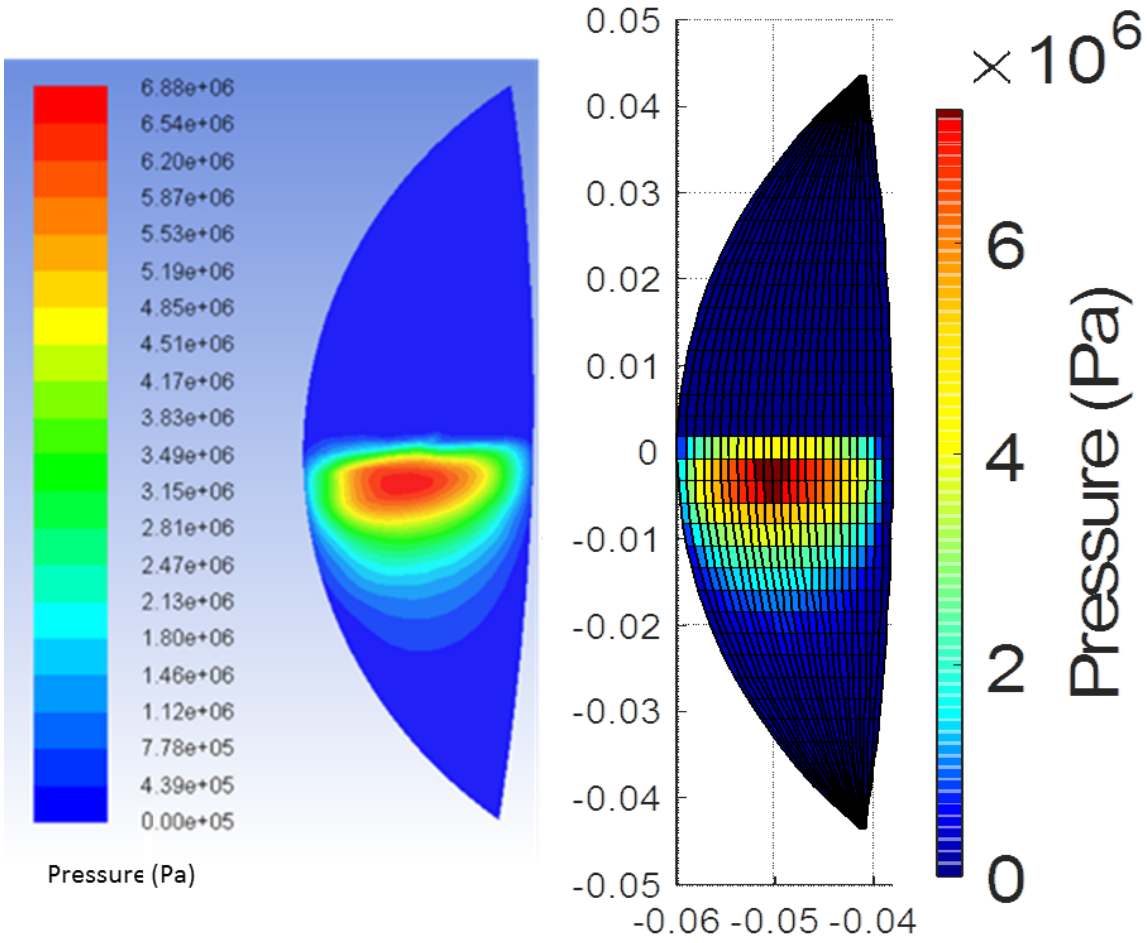

Figure 63. Pressure profile of TC lubricated area CFD (left) and FE model (right) in Pa for ω_{TC} = 7,500 rpm, ω_{BW} = 624 rpm, and F_{TC} = 1,000 N.

Figure 64 compares the CFD model (left and right) and the averaged binary experimental results (center). $\omega_{TC} = 7.5$ krpm, $\omega_{BW} = 0.64$ krpm and F_{TC} = 1 kN for this test point. These speeds are also typical of what could be seen in an industrial IGC. The FE and CFD model predict a similar lubricant cavitation area (35-45%), shown on the left. The cavitation occurs in the upper part of the LA, in the diverging section. There is no cavitation at the very top of the LA. The

location of cavitation is consistent with the experimental result, but the CFD model overpredicts the total lubricant cavitation area by 35%.

The predicted flow turbulence area from CFD matches the measured turbulent area from the measurements, but the CFD model tends to overpredict the total turbulent area. This could be due to small amounts of air ingestion at the inlet region leading to a lower viscosity and larger Reynolds number than predicted. Flow turbulence is highly related to the relative velocity between the oil inlet and the surface speed of the two disks. Turbulence has little effect on the predicted load capacity however. The testing does not include film thickness measurements, although these measurements could be incredibly useful for identifying the load capacity of the TC. Film thickness testing could be conducted by using an interferometer as detailed in recommendations for future work.

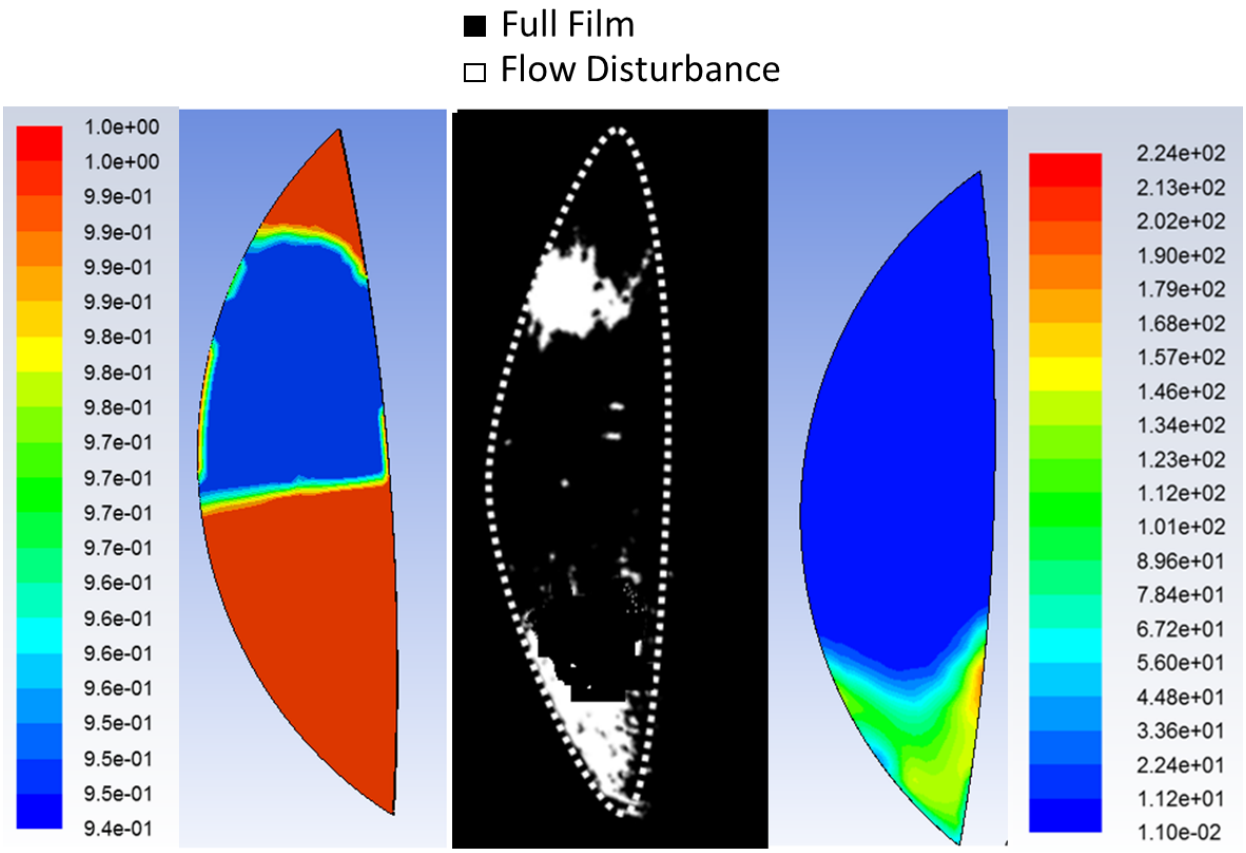

Figure 64. CFD lubricant cavitation liquid volume ratio (left) and dimensionless turbulent kinetic energy (right) with experimental results (middle) where the white pixels are locations of flow turbulence and lubricant cavitation, showing matching areas for the ω_{TC} = 7.5 krpm, ω_{BW} = 0.64 krpm and F_{TC} = 1 kN test case.

6. SUMMARY AND CONCLUSIONS

There is little available literature investigating the oil film within a thrust collar (TC) for use in integrally geared compressors (IGCs). Oil film hydrodynamics plays an important role in determining the static characteristics of bearing elements such as TCs. There are no published measurements for lubricant cavitation or flow turbulence in a TC. There are also no models in the literature that investigate lubricant cavitation or flow turbulence in a TC, and there is no methodology for performing a computational fluid dynamics (CFD) study. This work aimed at evaluating experimentally the lubricated area of a TC through a new optical test rig, improving existing models to allow for a mass conserving cavitation model and elastic deformation, and running a CFD model to compare with the experimental results.

The new test set-up shows repeatable experiments, which provides the first optical measurements of the TC lubricated area. The TC and bull gear (BG) have a 2 degree taper angle, and the rest of the TC dimensions are all comparable to TCs used in IGCs. The TC is made of transparent acrylic and has two windows in the steel backing which allow for visualization. A high speed camera, mirror, and oil spray mitigation mechanisms made it possible to capture images of the oil between the overlap region of the TC and BW at ω_{TC} = 2.5, 5, and 7.5 krpm and axial loads of 0.5, 1, and 1.5 kN. The lubricant sprayed into the TC is ISO VG 32 oil, and is sprayed at a range of oil inlet speeds between 3 and 30 m/s. The test rig achieved good success in identifying areas of cavitation and turbulence in the film, and provided the first experimental results for cavitation and turbulence in a TC.

The results were filtered and turned into binary images, which highlighted regions of interest. The binary images were converted into area weighted percent for lubricant cavitation and flow turbulence for each case in the test matrix. Results showed that lubricant cavitation in the diverging

section of the TC becomes clear at spin speeds greater than 5krpm, and is unaffected by unit load. The lubrication area (LA) also contains a turbulence area which grows as spin speed increases, and shrinks as the axial load increases.

The work also presents a finite element (FE) model based on the Reynolds equation. The model included a mass conserving model for cavitation and elastic deformation of the disks. The results were compared to an existing model without these considerations. And finally, the work also presented a CFD model including flow turbulence.

The experimental lubricant cavitation area is lower than both predictions from the FE and CFD models. The CFD and FE model have very similar pressure profiles, and minimum film thickness predictions. The CFD model tends to overpredict the flow turbulence area when compared to experiments. The model also shows a turbulence area that grows with increasing spin speed and decreases with increasing axial load. Increasing the oil inlet speed past the surface speed of the TC reduces the turbulence area, as shown by experiments and predictions. Flow turbulence tends to slightly increase predicted load capacity, and cavitation tends to slightly decrease it.

The major conclusions from the study are:

- Experimental results showed lubricant cavitation and flow turbulence do occur for a range of test conditions, which have been up to this point not included in literature.
- Neither flow turbulence nor lubricant cavitation have a significant effect on load capacity (<2%), and do not need to be considered in models only focused on load capacity. Turbulence does increase predicted power loss, but the increase is minimal (<2%) for the given test conditions.
- Elastohydrodynamic modeling demonstrated elastic deformation becomes important to load capacity for TCs made of steel (>55 bar unit load).

- Experimental oil inlet velocity results showed a method for reducing flow turbulence area with corroborating CFD predictions.

Future experimental testing should investigate the film thickness and pressure profile. The film thickness could be measured by using an interferometer or imbedded particles in the film. An interferometer could incrementally measure the entire film thickness profile of the LA. The interferometer should feature an internal mirror that would fit in the gap between the TC and bearing pedestal and that measures thickness to a 10-nanometer accuracy. Future testing could determine the load capacity of the TC for a wide range of test conditions by measuring a minimum film thickness.

The pressure profile could be measured through imbedded pressure transducers or through pressure sensitive paint. Imbedded pressure probes would require a slip ring as well as many small holes drilled into one of the disks. The speed of the disks also may require testing to only be done with one disk spinning, and the other held stationary. Pressure sensitive paint may not have the required accuracy or range for providing meaningful results. Another set of testing that could be helpful would be film starvation studies, which could be conducted through optical analysis using the current set-up.

REFERENCES

[1] K. Wygant and J. Bygrave, 2016, “Application and Design of Integrally Geared Compressors,” Proceedings of the 2nd Asia Pump and Turbomachinery Symposium, Singapore, pp. 21.-31, Feb.

[2] P. J. Beaty, K. Eisele, T. D. Maceyka, and C. Schwarz, 2000, “Integrally Geared API 617 Process Gas Compressors,” Proceedings of the Twenty-Ninth Turbomachinery Symposium, Texas A&M University, College Station, TX, pp. 239-246.

[3] M. Heß and A. Lohrengel, 2017, “Thrust cone bearings provide increased efficiency for helical gear units at moderate speed levels: Indications for possible energy saving potential in an expanded field of application,” Forsch Ingenieurwes, vol. 81, no. 2–3, 135–143, Sep.

[4] J. Niederhauser, 1925, “Apparatus for balancing the axial thrust in single helical toothed wheel gearing,” Patent # 1,548,545.

[5] V. A. Sadykov and L. M. Schneerson, 1968, “Helical gear transmissions with thrust collars,” Russian Engineering Journal, vol. 48, no. 1, pp. 31–34.

[6] H. Langer, 1982, “Hydrodynamische Axialkraftübertragung bei Wellen Schnellaufender Getriebe,” Konstruktion, vol. 34, no. 12, 473–478.

[7] V. Simon, 1984, “Thermal Elastohydrodynamic Lubrication of Rider Rings,” J of Tribology, vol. 106, no. 4, pp. 492–498, Oct.

[8] F. dM B. de Ling, H. P. Evans, and R. W. Snidle, 1996, “Thrust Cone Lubrication: Part 1: Elastohydrodynamic Analysis of Conical Rims,” Proceedings of the Institution of Mechanical Engineers, Part J: J. Tribol., vol. 210, no. 2, 85–96, Jun.

[9] D. W. Parkins and L. Rudd, 1996, “Thrust Cone Lubrication: Part 3: A Test Facility and Preliminary Measured Data,” Proceedings of the Institution of Mechanical Engineers, Part J: J. Tribol., vol. 210, no. 2, pp. 107–112, Jun.

[10] D. Thoden, 2006, “Elastohydrodynamische Schmierung von Druckkämmen,” Technische Universität Clausthal: Institut für Maschinenwesen.

[11] L. S. Andres, T. A. Cable, K. Wygant, and A. Morton, 2014, “On the Predicted Performance of Oil Lubricated Thrust Collars in Integrally Geared Compressors,” ASME J. Eng. Gas Turbines Power. 139(4), pp. 10-16.

[12] Cable TA, San Andrés L, Wygant K, 2016, “On the Predicted Effect of Angular Misalignment on the Performance of Oil Lubricated Thrust Collars in Integrally Geared Compressors.” ASME j Eng. Gas Turbines Power. 139(4), pp. 042503-1-11.

[13] T. Kerr, 2017, “Static and dynamic Coefficient Measurements of a Thrust Collar for use in an Integrally Geared Compressor,” Master’s Thesis, Texas A&M University, College Station.

[14] L. D. Wedeven, D. Evans, and A. Cameron, “Optical Analysis of Ball Bearing Starvation,” J. Lubrication Technology, vol. 93, pp. 349–361.

[15] A. T. Cross, F. Sadeghi, L. Cao, R. G. Rateick, and S. Rowan, 2012, “Flow Visualization in a Pocketed Thrust Washer,” Tribology Transactions, vol. 55, no. 5, pp. 571–581, Sep.

[16] L. San Andre´s and S. E. Diaz, 2001 “Pressure Measurements and Flow Visualization in a Squeeze Film Damper Operating With a Bubbly Mixture,” J. Tribol., vol. 124, no. 2, pp. 346–350, Feb.

[17] Y. Song, X. Ren, C. Gu, and X. Li., 2015, “Experimental and Numerical Studies of Cavitation Effects in a Tapered Land Thrust Bearing,” J. Tribol., vol. 137, no. 1, pp. 011701, Jan.

[18] M. J. Braun and W. M. Hannon, 2010, “Cavitation formation and modelling for fluid film bearings: A review,” Proceedings of the Institution of Mechanical Engineers, Part J: Journal of Engineering Tribology 224, no. 9 .

[19] P. D. Swales, D. Dowson, M. Godet, C. M. Taylor, 1974, ‘A review of cavitation phenomena in engineering situations’ In Cavitation and related phenomena in lubrication Mechanical Engineering Publications Ltd, London, UK pp. 3-9.

[20] L. Gumbel, 1914, "Das Problem der Lagerreibung" Mon. Berl. Bezirksverein., 1914V.D.I. 5: 87-104, pp. 109–120.

[21] B. Jakobson, L. Floberg, 1957, "The finite journal bearing considering vaporization," Goteborg, Sweden: Transactions of Chalmers University Technology 1957: pp. 1–119.

[22] H. G. Elrod, 1981 “A Cavitation Algorithm,” J. of Lubrication Tech, vol. 103, no. 3, pp. 350–354, Jul.

[23] D. Vijayaraghavan, and T. G. Keith Jr, 1990, ‘An efficient, robust, and time accurate numerical scheme applied to a cavitation algorithm.’ J. Tribol., 112(1), pp. 44–51.

[24] R. S. Paranjpe and T. Han, 1995, ‘A transient thermohydrodynamic analysis including mass conserving cavitation for dynamically loaded journal bearings.’ J. Tribol., 117(2), pp. 369–378.”

[25] R. F. Ausas, M. Jai, and G. C. Buscaglia, 2009, ‘A mass conserving algorithm for dynamical lubrication problems with cavitation.’ J. Tribol., 131.

[26] Li, X. S., Song, Y., Hao, Z. R., and Gu, C. W., 2012, ‘Cavitation Mechanism of Oil-Film Bearing and Development of a New Gaseous Cavitation Model Based on Air Solubility,’ ASME J. Tribol., 134(3), pp. 031701.

[27] Y. Song, C. Gu, and X. Ren, “Development and validation of a gaseous cavitation model for hydrodynamic lubrication,” J Engineering Tribology, vol. 229, no. 10, pp. 1227–1238, 2015.

[28] T. Woloszynski, P. Podsiadlo, and G. W. Stachowiak, 2015, “Efficient Solution to the Cavitation Problem in Hydrodynamic Lubrication,” Tribol Lett, vol. 58, no. 1, pp. 18, Apr.

[29] N. Brunetière, 2018, “A General Model for Liquid and Gas Lubrication, Including Cavitation,” J. Tribol., vol. 140, no. 2, pp. 021702, Mar.

[30] G. Bayada and L. Chupin, 2013, “Compressible Fluid Model for Hydrodynamic Lubrication Cavitation,” J. Tribol., vol. 135, no. 4, pp. 041702, Oct.

[31] Y. Dai, W. Wu, H. B. Zhou, J. Zhang, and F. Y. Ma. 2018, “Numerical Simulation and Optimization of Oil Jet Lubrication for Rotorcraft Meshing Gears,” Int. j. simul. model., vol. 17, no. 2, pp. 318–326, Jun.

[32] Q. Zeng, J. Zhang, J. Hong, and C. Liu, 2016, ‘A comparative study on simulation and experiment of oil-air lubrication unit for high speed bearing’, Industrial Lubrication and Tribology, Vol. 68 No. 3, pp. 325-335.

[33] C. Hirt, 1981, “Volume of Fluid (VOF) Method for the Dynamics of Free,” J. Comp. Phy. 39, no. 1, pp. 201-225.

[34] M. Yazdani, M.C. Soteriou, F. Sun, and Z. Chaudhry, 2014, "Prediction of the thermo-fluids of gearbox systems." International J. Heat Mass Transfer. 81, pp. 337-346.

[35] B. Manshoor, M. Jaat, Z. Izzuddin, and K. Amir, 2013, “CFD Analysis of Thin Film Lubricated Journal Bearing,” Procedia Engineering, vol. 68, pp. 56–62.

[36] J. Zhu, H. Chen, and X. Chen, 2013 “Large eddy simulation of vortex shedding and pressure fluctuation in aerostatic bearings,” J. Fluids and Structures, vol. 40, pp. 42–51, Jul.

[37] X. Jing, P. Xudong, B. Shaoxian, and M. Xiangkai, 2012, “CFD simulation of microscale flow field in spiral groove dry gas seal,” in Proceedings of 2012 IEEE/ASME 8th IEEE/ASME International Conference on Mechatronic and Embedded Systems and Applications, Suzhou, China, pp. 211–217, Jul..

[38] X. Yan, J. Li, and Z. Feng, 2011, “Investigations on the Rotordynamic Characteristics of a Hole-Pattern Seal Using Transient CFD and Periodic Circular Orbit Model,” J. Vibe. and Aco., vol. 133, no. 041007, Apr.

[39] B. O. Jacobson and B. J. Hamrock, 1983, “High-Speed Motion Picture Camera Experiments of Cavitation in Dynamically Loaded Journal Bearings,” J. of Lubrication Tech, vol. 105, no. 3, pp. 446–452, Jul.

[40] “P. Mueller, 1969, ‘Color Image Retrieval from Monochrome Transparencies,’ Appl. Opt. 8, pp. 2051-2057.”

[41] T. Kurita, N. Otsu, and N. Abdelmalek, 1992, “Maximum likelihood thresholding based on population mixture models,” Pattern Recognition, vol. 25, no. 10, pp. 1231–1240, Oct..

[42] R. M. Olson, “Cavitation Testing in Water Tunnels,” St. Anthony Falls Hydraulic Laboratory, Report, Dec. 1954. Accessed: Nov. 04, 2019.

[43] A. Kumar and J. F. Booker, 1991, “A Finite Element Cavitation Algorithm,” J. Tribol, vol. 113, no. 2, pp. 276–284, Apr.

[44] M. Hajjam, D. Bonneau, 2004, "Elastohydrodynamic analysis of lip seals with microundulations," Proceedings of the Institution of Mechanical Engineers, Part J: J. Tribol., 218(1) pp. 13-21.”

[45] X. Meng, S. Bai, and X. Peng, 2014. “An efficient adaptive finite element method algorithm with mass conservation for analysis of liquid face seals,” J. Zheijang Univ.-Sci., vol. 15, no. 3, pp. 172–184, Mar.

[46] J. N. Reddy, 1993. "An introduction to the finite element method," New York, 27.

[47] A. Z. Szeri, 1980, “Fluid Film Lubrication,” Cambridge Core, Dec.

[48] K. L. Johnson, Contact Mechanics. Cambridge University Press, 1987.

[49] “ANSYS FLUENT 12.0 Theory Guide - 16.7.4 Cavitation Models.” https://www.afs.enea.it/project/neptunius/docs/fluent/html/th/node343.htm (accessed Dec. 10, 2019).

[50] “ANSYS FLUENT 12.0 User’s Guide - 12.1 Introduction.” https://www.afs.enea.it/project/neptunius/docs/fluent/html/ug/node406.htm (accessed Dec. 10, 2019).

[51] L. Baldassarre, B. Andrea, R. Emanuele, F. Michele, and M. Francesco, 2015, "Axial Thrust in High Pressure Centrifugal Compressors: Description of a Calculation Model Validated by Experimental Data From Full Load Test." In 44th Turbomachinery & 31st Pump User Symposia (Pump & Turbo), Houston, TX, Sept, pp. 14-17.

[52] C. Shen, M. Khonsari, 2013, “On the Magnitude of Cavitation Pressure of Steady-State Lubrication,” Tribol Lett 51, pp. 153–160.

APPENDIX A

POWER LOSS MEASUREMENTS

Both the pinion and bull wheel shaft motors are powered by separate variable frequency drives (VFD). The VFDs display the power delivered to the motors. Both shafts are spun to the predetermined speed, there is no axial force applied to the pinion shaft, and there is no lubricant applied to the overlap area. The power displayed by the VFD is recorded as a baseline. The lubricant is then applied, and the pneumatic loader places the 2,600 N load on the pinion shaft. The VFD load outputs are recorded again. The difference between the loaded and unloaded VFD power outputs yields the power loss due to the TC lubricated area. The baseline test accounts for any motor inefficiencies, shaft windage and test rig bearing losses.

Figure 65 displays power loss measurements and predictions versus the pinion shaft spin speed for an axial load of 2,600 N. The predictions are taken from the code from Cable et al. [12]. Both measured and predicted power loss increases as a function of rotor spin speed. The measured power loss is higher than the predicted power loss by a factor of two. The author acknowledges VFD power loss measurements are not typically precise.

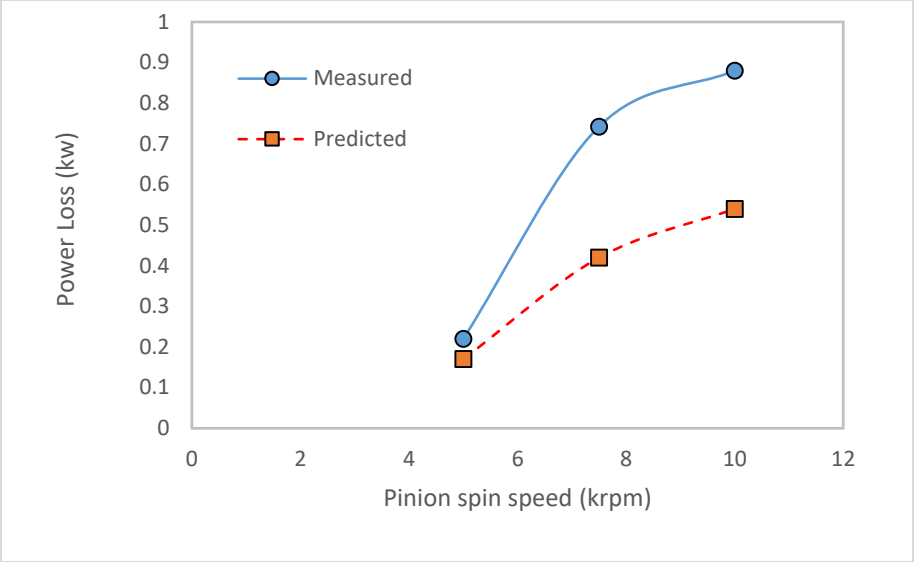

Figure 65. Power loss measurements and predictions as a function of pinion spin speed.

APPENDIX B

TC LA VIDEOS

The word version of this document contains embedded videos of the TC LA. The videos are embedded through youtube.com. The videos are not stored in this document, but on the website. So to watch the videos, the computer must have access to the internet, and to youtube. To watch the video, simply click the triangle in the center of the image. The videos are not embedded in the PDF version, instead follow the link.

Video B.1 shows start-up of the TC system. The BW begins spinning, and a small load is applied. There are two air pockets that become apparent in the video. Figure 43 is taken from a similar test condition. The nozzle is the open pipe, and at the beginning of the video, there is no oil being admitted to the LA, but as soon as the BW begins to spin, the oil is pulled in through shear force.

Video B.1: TC LA for a low load condition, $\omega_{TC} = 0$, $\omega_{BW} = 0 - 60$ rpm showing air entrapment in the upper part of the LA. https://www.youtube.com/watch?v=noZUXni4QnY

Video B.2 shows the LA once the BW has reached a steady speed, and there is a 1 kN load applied to the HSS. There is still no HSS motion. Both videos B.1 and B.2 are taken with a standard color camera, and the videos are played back at real time. Once the TC has reached steady state- there is no flow turbulence in the inlet region. There are clear cavitation streamers in the diverging section however.

Video B.2: TC LA for $\omega_{TC} = 0$, $\omega_{BW} = 60$ rpm, and $F_{TC} = 1$kN, showing cavitation upper part of the LA. https://www.youtube.com/watch?v=dpaNevDJaaQ

Video B.3 is a series of images captured from the HSC, for a test condition of $\omega_{TC} = 2.5$ krpm, $\omega_{BW} = 312$ rpm, and $F_{TC} = 0$. There is turbulence throughout the LA for this test condition, as there is no axial load to force the two disks together. Figure 46 is taken from this video.

Video B.3: TC LA for $\omega_{TC} = 2.5$ krpm, $\omega_{BW} = 312$ rpm, and $F_{TC} = 0$ showing turbulence throughout LA. https://www.youtube.com/watch?v=y_WUeLfzhG8&t=9s

Videos B.4-B.6 show the TC LA for three speed conditions, $\omega_{Tc} = 2.5$, 5, and 7.5 krpm, respectively. The HSC recorded the videos at a framerate of 5000 frames per second, and the videos are playing at 2 frames per second, so the videos are 2,500 times slower. The LA is reflected from a mirror, so that the inlet region is at the bottom, and the lubricant travels down the video to the exit (at the top of the LA). All three videos show flow turbulence occurring in the inlet region of the TC, and the flow turbulence area grows in each video according to the increasing TC speed. The flow turbulence area also changes for each shot, but maintains its position. Videos B.4 and B.5 show a small amount of cavitation streaking occurring in the diverging section, however it becomes clear in video B.6.

Video B.4: TC LA for $\omega_{TC} = 2.5$ krpm, $\omega_{BW} = 312$ rpm, and $F_{TC} = 500$ showing turbulence throughout LA. https://www.youtube.com/watch?v=_7Wz5TzQuss&t=3s

Video B.5: TC LA for $\omega_{TC} = 5$ krpm, $\omega_{BW} = 624$ rpm, and $F_{TC} = 1{,}000$ showing turbulence throughout LA. https://www.youtube.com/watch?v=vf0tCZ2kY-g

Video B.6: TC LA for $\omega_{TC} = 7.5$ krpm, $\omega_{BW} = 642$ rpm, and $F_{TC} = 1,000$ showing turbulence throughout LA. https://www.youtube.com/watch?v=-crrL5jS0eA

APPENDIX C

UNCERTAINTY ANALYSIS

A student t-distribution calculation determines the total uncertainties for the percent lubricant cavitation and flow turbulence area. The error associated to the high speed camera and determining the total area of the LA is small compared to the uncertainty from randomness. The mean and standard deviation is calculated from the 15 final binary images, so that a 95% confidence interval is obtained by

$$x - t_{\alpha,DOF} * \frac{\sigma}{sqrt(DOF)} < \mu < x + t_{\alpha,DOF} * \frac{\sigma}{sqrt(DOF)} \quad \textbf{(C.1)}$$

Where the true mean μ will lie between these values. The range is displayed in the report in the figures for cavitation and turbulence areas.